

Dissertation zur Erlangung des Doktorgrades
der Fakultät für Chemie und Pharmazie
der Ludwig-Maximilians-Universität München

**Implementation and Characterization
of a New Low Temperature
Tip-enhanced Near-field Optical Microscope**

von
Julia Janik
aus
Dresden

2017

Erklärung

Diese Dissertation wurde im Sinne von § 7 der Promotionsordnung vom 28. November 2011 von Herrn Prof. Dr. Achim Hartschuh betreut.

Eidesstattliche Versicherung

Diese Dissertation wurde eigenständig und ohne unerlaubte Hilfe erarbeitet.

München, 30.03.2017

.....

(Julia Janik)

Dissertation eingereicht am 31.03.2017

1. Gutachter: Prof. Dr. A. Hartschuh

2. Gutachter: Prof. Dr. J. Wintterlin

Mündliche Prüfung am 22.05.2017

Abstract

The rise of nanotechnology led to the development of different techniques to analyze nanostructures precisely. Tip-enhanced near-field optical microscopy (TENOM) is able to characterize these structures at sub diffraction length scales with high detection sensitivity. Of particular interest would be the implementation of TENOM at low temperatures, because of the reduction of thermal broadening, the slow down of relaxation processes and the potentially stronger localization of excited states. This work presents the implementation of a new design for TENOM measurements at low temperatures. The microscope shows some unique features, compared to previous systems. Its key element is a solid immersion lens (SIL), which is introduced as dielectric substrate to achieve detection angles beyond a numerical aperture (NA) of one. The usage of the SIL results in the problem of the path difference, which leads to a reduced movement of the focus, while scanning the SIL. This effect prevents the tip from staying in the laser focus during a scan, which is crucial for a successful TENOM measurement. To overcome this problem, two independent moving scanner stacks were implemented, controlled by the so called synchronous scan. The first part of this thesis focuses on the characterization of the SIL and the optimization of the synchronous scan parameters. In the second part of the thesis, the tuning fork based atomic force microscope (AFM) was tested at low temperatures. A particular challenge was the strong increase of the quality factor of the tuning fork at low temperatures. This was addressed by using the Q control feature of the measuring software. After optimizing the Q factor and the feedback parameters, topography scans of single walled carbon nanotubes (SWCNT) were successfully performed. These measurements show a stable topography with a height resolution down to 0.6 nm and a lateral resolution only defined by the size of the tip. The third part of this thesis describes the final improvements towards low temperature TENOM measurements. A second illumination channel was added, to ensure a faster and easier tip centering, while the likelihood of damaging the tip is reduced. In addition, a mode converter was introduced, to create a radially polarized laser mode, for the efficient generation of the tip-enhanced near-field. These improvements and the optimization of the scan and feedback parameters, lead to the first TENOM measurements at 77 K. These measurements were performed on SWCNTs and showed a spatial resolution of the photoluminescence signal down to 35 nm.

Contents

1	Introduction	1
2	High-resolution Optical Microscopy	5
2.1	The Resolution Limit	6
2.2	Tip-enhanced Near-field Optical Microscopy	9
2.2.1	The Optical Antenna	10
2.2.2	Tip-enhanced Fluorescence	13
2.2.3	Tip-enhanced Raman Scattering	14
2.3	Low Temperature Near-field Measurements	15
3	Single Walled Carbon Nanotubes as Model System	21
3.1	Structure	21
3.2	Optical Properties	23
3.2.1	Photoluminescence	23
3.2.2	Temperature Dependence of Photoluminescence	25
3.2.3	Raman Scattering	27
4	Experimental Details	29
4.1	New Low Temperature Microscope Setup	29
4.1.1	Low Temperature Microscope Optics	30
4.1.2	Low Temperature Atomic Force Microscope	38
4.1.3	Electronics	43
4.2	Sample Fabrication	46
5	Results and Discussion	47
5.1	Characterization of the Solid Immersion Lens	47
5.1.1	Surface Characterization	48
5.1.2	Synchronous Scan	50
5.1.3	Low Temperature Confocal Imaging	52
5.2	Characterization of the Low Temperature Atomic Force Microscope	55
5.2.1	Resonance Stability	55

CONTENTS

5.2.2	Feedback Stability	58
5.2.3	Low Temperature Atomic Force Measurements	61
5.3	Low Temperature Tip-enhanced Near-field Measurements	63
5.3.1	Tip Centering	63
5.3.2	Tip-enhanced Near-field Measurements at Low Temperature	65
6	Summary and Outlook	73
7	Appendix A: Manual for Handling the Low Temperature Setup	77
A.1	Structure and Parts of the Setup	77
A.2	General Points	81
A.3	Software	81
A.3.1	Software User Interface	83
A.3.2	Data Saving	89
A.4	Preparations for Low Temperature Measurements	91
A.4.1	Tuning Fork Soldering	91
A.4.2	Tip Gluing	92
A.4.3	Centering SIL and Tip	93
A.4.4	Transfer Microscope Stick to Vacuum Chamber and Pumping Down	95
A.4.5	Transfer to Cryostat and Cooling	96
A.5	Tip-enhanced Measurements	97
A.5.1	Center SIL and Confocal Imaging	97
A.5.2	Approach and Find Tip	97
A.5.3	Center Tip for Sync Scan	98
A.5.4	Scan Parameters for Low Temperature Scanning	99
A.6	Troubleshooting	99
	Bibliography	101
	List of Abbreviations	113
	List of Publications	119
	List of Conferences	121
	Acknowledgments	123

1 Introduction

Compared to the big innovations in history, today the revolution of technology lies in the smallest things. Nanoscience is one of the key disciplines of the 21st century. In 1959 Richard Feynman first brought up the topic of nanotechnology without using this term. In his famous talk “There’s Plenty of Room at the Bottom” he predicted the rise of nanotechnology. Parts of his ideas already became reality. And the field is still expanding: In 2013 the basic research budget of the “Bundesministerium für Bildung und Forschung” for nanosciences amounts to 220 million€ and in the same year a growth of 27% in nanotechnological companies was reported [1].

But what is nanotechnology? It is a growing part of industry that focuses on nano-sized materials. Its field of application ranges from material science and medical treatments to energy technique and catalytic applications. And therefore it is not limited to physics but found its way into a plenty of research fields and applications. They all take advantage of the unique characteristics of nanoparticles. The size of these nanomaterials reaches dimensions below 100 nm which causes a change in the electronic, optical and magnetic properties. In this range classical mechanical descriptions become too inaccurate and quantum mechanical effects occur. Depending on their application nanomaterials come in different shapes, compositions and structures.

The arise of nanostructures triggered the development of microscopes and techniques to analyze and characterize them precisely. There are several techniques that are capable of providing the desired atomic resolution. Transmission electron microscopy (TEM) has a resolution down to 0.5 Å [2] and delivers information about the crystallinity and morphology. To gain topographic information atomic force microscopy (AFM), scanning electron microscopy (SEM) or scanning tunneling microscopy (STM) are the tools of choice. The latter also provides insight into the electronic density of states near the Fermi energy and the spatial probability distribution of the sample wavefunction. All these techniques can determine different properties of the sample material but none of them can image its optical properties.

As a result, overcoming the resolution limit, given by the wavelength of light, has been a key issue in the further development of optical microscopes. Their importance reflects in the noble price which was awarded to Eric Betzig, Stefan W. Hell and William E. Moerner for “the development of super-resolved fluorescence microscopy” in 2014 [3]. This price awarded two super-resolution methods based on far-field techniques such as stimulated emission depletion (STED), photo activated localization microscopy (PALM) and stochastic optical reconstruction microscopy (STORM) [4, 5]. Besides these far-field methods a second series of techniques, that makes use of optical near-field interactions exist. It can be summarized with the term scanning near-field optical microscopy (SNOM). Tip-enhanced near-field optical microscopy (TENOM) belongs to this group and it combines high sensitivity with few nanometer spatial resolution. This technique is based on the field enhancement locally induced by a metallic tip, due to localized surface plasmons and the lightning rod effect. Upon laser illumination a strong electromagnetic field can be achieved in the vicinity of the tip which leads to confinements in the range of the tip radius. The probe is raster-scanned in small distance to the sample to enable imaging and mapping of the spectral information. Until to date, TENOM measurements have been performed by several groups all around the world on a wide variety of sample material, such as single walled carbon nanotubes [6, 7], 2D materials [8, 9] and biological structures [10, 11]. In recent years resolutions down to 0.7 nm have been demonstrated [7], which stands in conflict with the established ideas of the extended plasmonic fields. Therefore, several novel models using different phenomena have to explain these results. Still, the enhancement mechanism is not yet fully understood and more experiments are needed.

Semiconductor nanomaterials are of high interest, particular with regard to the miniaturization of electronic components and optical applications. To fully understand their potential, nanospectroscopic measurements have to be performed in different environments like low temperatures and under external fields. Magnetic-field SNOM measurements already have been reported by several groups with different systems and materials [12–15]. Low temperature measurements have the advantage of smaller line widths, due to the reduced temperature induced broadening and slowed down relaxation processes upon cooling. Additionally, low temperatures require vacuum or inert gas atmosphere, this improves the photochemical stability of the sample material. Several attempts to develop cryogenic-SNOMs have been reported. Different types of SNOMs have been tested, all having advantages and disadvantages depending on if they are based on an aperture [16] or scattering tip [17] or if a flow cryostat [18] or cold finger [19] is used. Either way the conditions are challenging

and the systems have to be optimized and tested carefully, taking into account all optical and mechanical influences.

The aim of this work is the implementation, testing and characterization of a new low temperature SNOM setup. Compared to previous works, this setup exhibits some new features to improve the performance of tip-enhanced measurements at low temperatures. It also is the first setup to use an optical antenna to enhance the signal. One main addition in the design of the microscope is the use of a solid immersion lens (SIL) to improve the detection angle. For the characterization of the microscope one can divide the system into two main parts. The optical detection containing the SIL and the low temperature tuning fork AFM. Both can work independently from each other, but must be combined and work together to gain near-field images. The performance of all microscope sections was characterized under low temperature conditions and improved if necessary. At the end the interaction of all components was tested by performing tip-enhanced near-field measurements at low temperatures.

The thesis is structured as follows: Chapter 2 focuses on the principles of tip-enhanced near-field measurements and additionally gives an overview over the state of art of low temperature SNOM measurements. In chapter 3 the basic properties of single walled carbon nanotubes are discussed containing a section on their behavior at low temperatures. The single walled carbon nanotubes were used as a model system because of their well known structure and behavior. Chapter 4 gives a detailed description of the experimental setup including its electronics and describes the sample fabrication. The results are presented in chapter 5. It is divided in the characterization of SIL and AFM and concludes with the presentation of the first tip-enhanced near-field measurements performed with the setup at low temperatures. At the end the work is summarized and some ideas for further improvements are discussed.

2 High-resolution Optical Microscopy

The light microscope is the simplest form of an optical microscope and known for about 400 years. It is a fundamental tool in science, since it allows the observation of small structures and can be combined with spectroscopy to gain additional information, e.g. about electronic and vibronic excitation. In the last decades, the structures of interest, e.g. in biomedicine and semiconductor industry, are continuously getting smaller, such as nanostructures with dimensions below 100 nm. The confocal microscope shows the best resolution among all conventional optical microscopes and allows imaging in three dimensions. This makes it an essential tool in biology, as well as in material science [20]. Despite improvements in lens design and detection systems the resolution limit for optical microscopy is defined by about half the wavelength of the light. The reason is the diffraction of propagating waves that constitute light, which cannot be compensated for.

In recent years, several techniques to overcome the diffraction boundary have been developed. They are divided in far-field and near-field techniques. Far-field concepts showed a rapid development over the last decade, which was highlighted by awarding the noble prize "for the development of super-resolved fluorescence microscopy" to Eric Betzig, Stefan W. Hell and William E. Moerner in 2014 [3]. As the name implies, far-field techniques only detect propagating waves. Important far-field methods are for example: stimulated emission depletion (STED), photo activated localization microscopy (PALM) and stochastic optical reconstruction microscopy (STORM) [4, 5]. These techniques are used primarily in biological applications, since they enable the three dimensional observation of a system. Unfortunately, with decreasing sample volume the signal intensity gets weaker, far-field methods do not offer the opportunity to enhance such signals. Near-field techniques, on the other hand, exploit the evanescent fields by using short sample-probe distances. The first near-field setup to image single fluorescent molecules was a so-called aperture scanning near-field optical microscope (a-SNOM) [21]. This technique uses a nanometer sized aperture for illumination, which is kept at small distance above the sample. In this configuration,

the emitted light is collected in the far field [22]. The same aperture probes can also be used to locally collect the light emitted by the sample. A different approach is tip-enhanced near-field optical microscopy (TENOM) where a sharp metallic tip is used to interact with the near-field of the sample. Due to the exponential decay of the near-field, the distance between sample and tip needs to be small, in the range of a few nanometers. To collect a substantial fraction of the near-field SNOM and TENOM are limited to sub-surface studies.

The fundamentals of optical microscopy and the problem of the diffraction limit will be discussed in the first part of this chapter using the angular spectrum representation. The following sections will focus on tip-enhanced near-field optical microscopy and introduce the optical antenna and its role in the signal enhancement.

2.1 The Resolution Limit

To visualize the problem of the resolution limit, the angular spectrum representation of optical fields is the mathematical technique of choice. It describes a series of free-space propagating field components in terms of plane and evanescent waves with arbitrary amplitudes and directions.

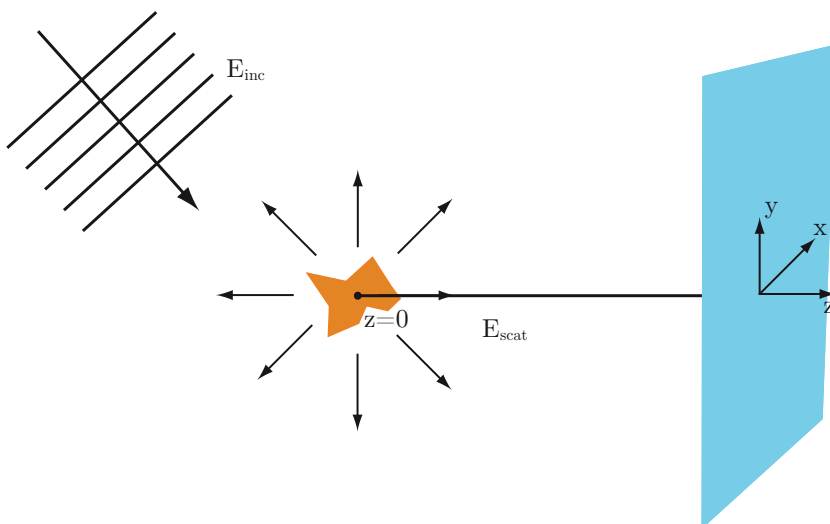


Figure 2.1: Schematic of the optical scattering problem.

Figure 2.1 illustrates the geometry of the problem: In the beginning we observe an electric field $\mathbf{E}(x, y, z) = \mathbf{E}_{inc} + \mathbf{E}_{scat}$ propagate from an arbitrary scattering object at position $z = 0$. The z -direction is the direction of propagation and the fields may

be collected on a detector in a xy plane at constant z . The field \mathbf{E} can be calculated by the angular spectrum representation at any position along the z -axis [23].

The 2D Fourier transformation of the field \mathbf{E} at any position z is presented in equation 2.1.

$$\hat{\mathbf{E}}(k_x, k_y; z) = \frac{1}{4\pi^2} \int_{-\infty}^{\infty} \int_{-\infty}^{\infty} \mathbf{E}(x, y, z) e^{-i(k_x x + k_y y)} dx dy \quad (2.1)$$

The equivalent inverse Fourier transformation looks as follows:

$$\mathbf{E}(x, y, z) = \int_{-\infty}^{\infty} \int_{-\infty}^{\infty} \hat{\mathbf{E}}(k_x, k_y; z) e^{-i(k_x x + k_y y)} dk_x dk_y. \quad (2.2)$$

In both equations presented above x and y are the Cartesian coordinates and k_x, k_y the corresponding reciprocal coordinates of the wave vector \mathbf{k} . We assume a homogeneous, isotropic and linear medium along the transversal plane and define

$$|k_z| \equiv \sqrt{k^2 - k_x^2 - k_y^2} \quad \text{with} \quad \text{Im}\{k_z\} \geq 0. \quad (2.3)$$

Here, k depends on the wavelength λ and the refractive index n of the surrounding medium by $k = \frac{2\pi n}{\lambda}$. With the assumptions made above the electric field has to satisfy the Helmholtz equation. If we insert the inverse Fourier transformation (Eqn. 2.2) in the Helmholtz equation, we gain the development of the Fourier spectrum along the z -axis as show in equation 2.4.

$$\hat{\mathbf{E}}(k_x, k_y; z) = \hat{\mathbf{E}}(k_x, k_y; 0) e^{\pm i k_z z} \quad (2.4)$$

$\hat{\mathbf{E}}$ is called the angular spectrum with $e^{\pm i k_z z}$ as propagator and the definition of the propagation direction by \pm . The angular spectrum determines the amplitudes of the waves, which are characterized by the wave numbers and the corresponding direction of propagation. This helps to represent the fields by their angular spectrum for any z values.

$$\mathbf{E}(x, y, z) = \int_{-\infty}^{\infty} \int_{-\infty}^{\infty} \hat{\mathbf{E}}(k_x, k_y; 0) e^{-i(k_x x + k_y y)} e^{\pm i k_z z} dk_x dk_y \quad (2.5)$$

Equation 2.5 is the angular spectrum representation and describes the behavior of the electric field \mathbf{E} . It enables the calculation of the electric field anywhere in the material as long as it is homogeneous, isotropic and linear. The angular spectrum presentation contains contributions from all possible wave vectors and includes propagating waves as well as evanescent waves. The character of the wave can be described by the z -component k_z which can be real or imaginary, depending on k_x and k_y . For small, spatial frequencies $k_x^2 + k_y^2 \leq k^2$ is valid and k_z is real. In this case the wave propagates in z -direction with an amplitude of $\hat{\mathbf{E}}(k_x, k_y; z = 0)$ and an oscillation of $e^{\pm i k_z z}$. The k_z component becomes complex in case of $k_x^2 + k_y^2 > k^2$ and describes an exponential decay of the wave.

$$\text{plan wave : } e^{-i(k_x x + k_y y)} e^{\pm i |k_z| z}, \quad k_x^2 + k_y^2 \leq k^2 \quad (2.6)$$

$$\text{evanescent wave : } e^{-i(k_x x + k_y y)} e^{-|k_z| |z|}, \quad k_x^2 + k_y^2 > k^2 \quad (2.7)$$

The description indicates that plane waves can propagate, whereas evanescent waves decay fast, exponentially with the distance to the source. Since k depends on the wavelength of the light and the refractive index of the surrounding medium, a decrease of frequency in the range of $k_x^2 + k_y^2 > (\frac{2\pi n}{\lambda})^2$ with growing distance can be observed. Far away from the source only the spatial frequencies of plane waves can be detected. The propagation corresponds to a low-pass filtering of spatial frequencies with an upper limit of $k_x^2 + k_y^2 = k^2$. The increasing loss of information due to the propagation of the wave leads to a broadening of the field distribution and, therefore, to a loss in resolution.

The spatial resolution of an imaging system is determined by Δr , which is the distance needed to distinguish two separate point sources in the object plane. This distance is related to the width of the point spread function (PSF) of the imaging system, which describes the pattern rendered by a point source. As mentioned above the resolution of an optical system depends on the bandwidth of the detected spatial frequencies ($\Delta k = \sqrt{\Delta k_x^2 + \Delta k_y^2}$). To distinguish two point sources $\Delta r \cdot \Delta k \geq 1$ has to be fulfilled [23]. This behavior is similar to the Heisenberg's uncertainty principle. To improve the resolution it is crucial to maximize the width of the collected in-plane wave vector components. In the far-field the upper boundary is set by $k = \frac{2\pi n}{\lambda}$, because of the loss of the evanescent waves (eqn. 2.6, 2.7). In this case the best resolution possible is given by equation 2.8.

$$\Delta r_{min} = \frac{\lambda}{2\pi n} \quad (2.8)$$

Additionally, the influence of the optical components in the system has to be taken into account. In practice, the complete range of plane waves can not be collected, due to the limited collection angle of the system. The resolution limit of a system is thus determined by its numerical aperture $\text{NA} = n \sin(\theta)$. The numerical aperture is described by the half-angle of the maximum cone of light θ and the refractive index n between sample and lens.

In the best case, the lateral resolution for conventional optical imaging systems is given by equation 2.9.

$$\Delta r_{min} = \frac{\lambda}{2\pi\text{NA}} \quad (2.9)$$

In axial (z -direction) the focus is not a circular spot but forms an ellipse. The best conventional microscope regarding axial and lateral resolution is the confocal microscope. It cancels the contributions of out-of-plane emitters by incorporating a pinhole in the detection beam path. As a result only the signals from a sample volume located within the distance Δr_{axmin} are detected [24]. This distance defines the axial resolution of a confocal microscope.

$$\Delta r_{axmin} = 2 \frac{n\lambda}{\text{NA}^2} \quad (2.10)$$

Due to its improved detection behavior and the relatively easy handling the confocal microscope has become the system of choice for many scientific applications. Nevertheless it can not overcome the diffraction limit or enable the detailed analysis of materials on a length scale below $\lambda/2$.

2.2 Tip-enhanced Near-field Optical Microscopy

Tip-enhanced near-field optical microscopy has been used for more than 10 years [25] in different configurations and by groups all over the world [26–29]. The technique provides a spatial resolution down to few nanometers and even below. It has been demonstrated on an increasing variety of sample materials such as carbon based nanomaterials [9, 30], inorganic nanowires [31, 32], as well as biological materials [33, 34]. Besides the improved spatial resolution, the advantage of TENOM over the far-field techniques is, that the signal in the vicinity of the tip gets enhanced. Therefore, this method can be used to image weak emitters and very small sample volumes. During a measurement a metal tip is centered in the laser focus near the sample

surface while the sample is raster-scanned in x-y-direction. The imaging exploits the extremely short-ranged interaction of the probe with the near-field of the sample and additionally gains topographic information. To maintain a constant distance of a few nanometers to the sample surface, an atomic force or scanning tunneling microscope is used. The resolution of the method is mainly determined by the radius of the tip and its distance to the sample surface. Due to the lightning rod effect and the excitation of surface plasmons, a field enhancement in the vicinity of the tip can occur, which leads to an increased resulting signal and an overall higher detection sensitivity.

2.2.1 The Optical Antenna

The metallic tip concentrates the laser radiation to a spot below the diffraction limit and in doing so replaces an objective or focusing lens. It converts free-propagating optical radiation to localized energy and *vice versa* [35–38], which is the definition of an optical antenna. The antenna is introduced between an emitter or receiver and the free radiation. It can act as emitter, enhancing the excitation of the receiver, or as receiver enhancing the emitted light of the transmitter [39]. A scheme of the described interaction is shown in figure 2.2. In contrast to their microwave counterparts, the properties of an optical antenna strongly depends on the material properties and shape, due to surface plasmon resonances [40].

For a comprehensive characterization of an optical antenna, terms of the classical antenna theory are used and redefined. To simplify the description a dipole-like behavior of receiver and transmitter is assumed.

The two enhanced processes, namely emission and absorption, have to be considered in order to get a complete picture of the optical antenna enhancement. A practical way to characterize the enhanced emission is the antenna efficiency, which is defined in equation 2.11. It describes the ratio between the total power dissipated by the antenna P and the radiative power P_{rad} . The total power P is composed of P_{rad} and the power dissipated through other channels for example heat P_{loss} [37].

$$\epsilon_{rad} = \frac{P_{rad}}{P} = \frac{P_{rad}}{P_{rad} + P_{loss}} \quad (2.11)$$

The antenna's ability to focus the radiated power into a certain direction can be measured by the directivity D . It considers the angular power density $p(\theta, \phi)$ with θ and ϕ as the angles of the direction of observation.

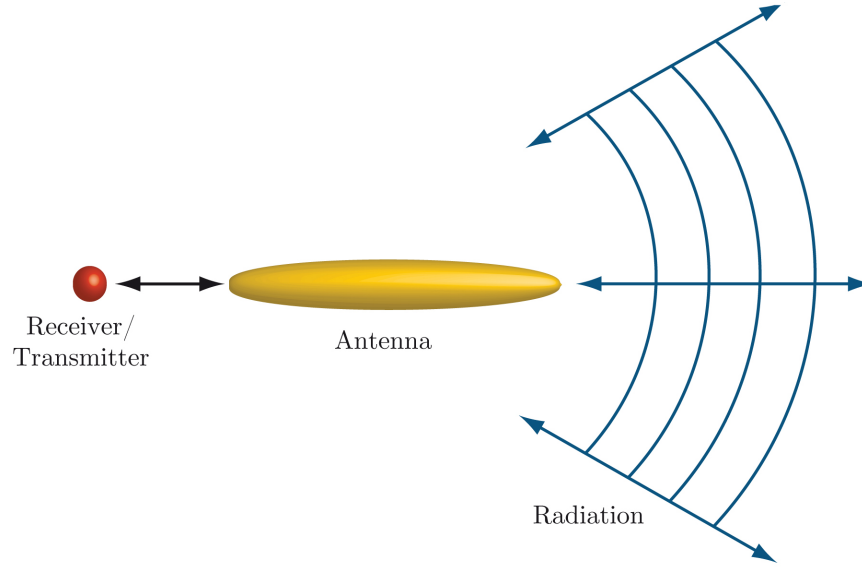


Figure 2.2: Principle of an optical antenna coupled to a point-like receiver or transmitter. The antenna can interact with the emitter as receiver or transmitter and enhance either excitation or emission or both.

$$D(\theta, \phi) = \frac{4\pi}{P_{rad}} p(\theta, \phi) \quad (2.12)$$

By taking the polarization into account, one can define the partial directives as

$$D_\theta(\theta, \phi) = \frac{4\pi}{P_{rad}} p_\theta(\theta, \phi), \quad D_\phi(\theta, \phi) = \frac{4\pi}{P_{rad}} p_\phi(\theta, \phi) \quad (2.13)$$

with p_θ and p_ϕ as normalized angular powers.

The antenna gain G combines the efficiency and directivity of an antenna to yield the radiation relative to the total power.

$$G(\theta, \phi) = \epsilon_{rad} D(\theta, \phi) \quad (2.14)$$

For a full description of the antenna properties the enhanced absorption has to be discussed. The most important parameter in this process is the antenna aperture A , which corresponds to the absorption cross section σ in the presence of the tip. It describes the efficiency with which the incident radiation is captured to excite the receiver with the power P_{exc} . I is the intensity of the radiation with the polarization \mathbf{n}_{pol} coming from (θ, ϕ) direction.

$$A(\theta, \phi, \mathbf{n}_{pol}) = \frac{P_{exc}}{I} = \sigma_A(\theta, \phi, \mathbf{n}_{pol}). \quad (2.15)$$

The tip enhances the field at the absorber and by defining the field in absence of the tip as \mathbf{E}_0 and in presence of the tip with \mathbf{E} the absorption cross section (σ) becomes

$$\sigma = \sigma_0 |\mathbf{n}_p \cdot \mathbf{E}|^2 / |\mathbf{n}_p \cdot \mathbf{E}_0|^2. \quad (2.16)$$

Here, \mathbf{n}_p is the orientation of the absorption dipole and the superscript "0" indicates the absence of the antenna. Equation 2.16 shows that the absorption process depends on the incident direction and polarization of light.

If we consider the same optical frequency, a transmitting antenna is also a good receiving antenna. More specifically, absorption and emission should follow the reciprocity theorem. This leads to a connection between the excitation rate Γ_{exc} and its spontaneous emission rate Γ_{rad} .

$$\frac{\Gamma_{exc,\theta}(\theta, \phi)}{\Gamma_{exc,\theta}^0(\theta, \phi)} = \frac{\Gamma_{rad} D_\theta(\theta, \phi)}{\Gamma_{rad}^0 D_\theta^0(\theta, \phi)} \quad (2.17)$$

The index θ refers to one polarization state but can also be denoted ϕ , which corresponds to a rotation of the polarization by 90° . Neglecting the vectorial character the spontaneous emission rate enhancement can be expressed by the local field enhancement factor f as $f^2 = \Gamma_{rad}/\Gamma_{rad}^0$. This relation is also true for the excitation enhancement in equation 2.16 with $f^2 = \Gamma_{exc}/\Gamma_{exc}^0$. The field enhancement factor is defined as the ratio between the electric field at the tip and without the tip.

The field enhancement of an antenna has three different contributions: the lightning rod effect, the excitation of resonant surface plasmons and antenna resonances. The lightning rod effect is non-resonant, depends on the tip geometry and leads to the confinement of surface charge densities at the apex of the tip. The antenna resonances occur, if the length of the antenna scales with the wavelength of the incident light. This behavior is only true for radiowave antennas, but does not apply at optical frequency, since at optical frequencies, metals cease being ideal conductors and radiation starts to penetrate into the metal. As a consequence, the antenna interacts with the effective wavelength λ_{eff} and not with the incident radiation λ . The effective wavelength shows a linear behavior with the plasma wavelength of the metal λ_p and the constants n_1 and n_2 that depend on geometry and dielectric properties.

$$\lambda_{eff} = n_1 + n_2 \left(\frac{\lambda}{\lambda_p} \right) \quad (2.18)$$

In general, the enhanced fields of the optical antenna are highly dependent on the shape and structure of the used antenna-substrate system and the resulting near-field is always highly complex. Several studies have been performed to characterize the field enhancement for different conditions [41–44].

Depending on the experimental geometry different substrates can be used. The dielectric properties of the sample substrate have to be considered, since they influence the enhancement [44, 45]. Electromagnetic coupling between the charges in the tip and the induced charges in the substrate takes place. For dielectric substrates, Raman enhancement factors in the range of $10^2 - 10^7$ have been found [28]. The presence of a metallic substrate leads to the coupling between tip and substrate plasmons, resulting in the formation of the so-called gap plasmon mode. A far stronger confinement of the field as well as higher field enhancement factors can be achieved by using this gap mode configuration. As a result, the light in the nanogap can be confined to dimensions smaller than the tip apex [40, 46]. Since the near-field decays exponentially, the distance between tip and substrate has to be taken into account and should be as short as possible. An increase in tip-substrate distance will lead to weaker fields and a loss in resolution [43]. When the distance between tip and substrate enters the sub-nanometer length scale, quantum mechanical effects, such as electron tunneling and nonlocal screening, become important [47].

The following section shows how the optical antenna enhances different optical processes.

2.2.2 Tip-enhanced Fluorescence

The fluorescence intensity depends on the quantum yield η of the system and the excitation rate Γ_{exc} . The quantum yield takes into account that not every excited state emits a photon due to competing non-radiative losses Γ_{nr} (eqn. 2.19).

$$\eta^0 = \frac{\Gamma_{rad}}{\Gamma_{rad} + \Gamma_{nr}} \quad (2.19)$$

The fluorescence rate, i.e. the number of photons emitted per second, in the absence of an optical antenna is given by:

$$\Gamma_{FL} = \Gamma_{exc} \cdot \eta^0 = \Gamma_{exc} \frac{\Gamma_{rad}}{\Gamma_{rad} + \Gamma_{nr}}. \quad (2.20)$$

The presence of an optical antenna enhances the excitation rate, but also modifies the non-radiative rate. The fluorescence enhancement can be written as

$$M_{fl} \approx \frac{\Gamma_{exc}}{\Gamma_{exc}^0} \frac{\eta}{\eta^0} = f^2 \frac{\eta}{\eta^0}, \quad (2.21)$$

where η is the quantum yield in the presence of the tip. Equation 2.21 shows that the fluorescence enhancement depends on the quantum yield of the material. Emitters with a high quantum yield ($\eta^0 \approx 1$) already have a strong signal that can not be further enhanced. In this case only the excitation rate influences the enhancement. For weak emitters ($\eta^0 \ll 1$), such as carbon nanotubes, the enhancement is most effective. Here, the radiative rate can be neglected in the denominator and the quantum yield can be expressed by $\eta = \Gamma_{rad}/\Gamma_{nr}$. Assuming that the antenna has a small effect on the non-radiative rate the fluorescence enhancement behaves like the Raman enhancement and scales with f^4 (see section 2.2.3).

2.2.3 Tip-enhanced Raman Scattering

The Raman scattering signal contains vibrational information about a sample and can provide a unique chemical fingerprint. The Raman scattering cross section, on the other hand, is typically low and, therefore, the signal of single molecule is often too weak to be detected. The Raman signal intensity depends on the product of both, the transition rates Γ_{exc} and Γ_{rad} , as well as the directivity $D_\theta(\theta, \phi)$ and the detection efficiency $\eta_\theta(\theta, \phi)$ of the setup. To derive the total signal it is necessary to integrate over all angles since ϕ is limited by the maximum detection angle ϕ_m of the setup (eqn. 2.22). Additionally, the wavelength dependence has to be taken into account.

$$S_{Raman,\theta} = 1/4\pi \int_0^{2\pi} \int_0^\pi \Gamma_{exc,\theta} \Gamma_{rad} D_\theta \eta_\theta \sin\theta d\theta d\phi \quad (2.22)$$

Due to the low signal intensity, it is advantageous to use an enhancement mechanism. A nearby antenna influences incoming and outgoing fields and since absorbed and emitted photons have nearly the same energy the total signal enhancement scales with approximately the fourth power of the enhancement factor. Equation 2.23

shows a simplified representation, where the angular and polarization dependence is neglected.

$$M_{Raman} \approx \frac{\Gamma_{exc} \Gamma_{rad}}{\Gamma_{exc}^0 \Gamma_{rad}^0} \approx f^4 \quad (2.23)$$

Tip-enhanced Raman scattering (TERS) has been used to study carbon nanotubes [48], biological materials [10, 11] and other materials [49–51]. Only recently sub-nanometer resolved optical images of single molecules [52] and carbon nanotubes [7] could be shown. These measurements and other experiments that show a nonlinear power dependence of the enhanced signal put the understanding of the enhancement process into question. Now, new signal-enhancement concepts are being discussed, taking into account optomechanical coupling [53, 54] or electric field gradient [55] to explain the observations.

2.3 Low Temperature Near-field Measurements

The first single molecule detection and spectroscopy, at cryogenic conditions, has been performed in 1989 [56] by Moerner et al., by suspending single dye molecules in a host crystal. They took advantage of the zero-phonon lines arising at low temperatures and their sensitivity to changes in the environment. In an ideal system all molecules in the host system would experience the same environment and a spectrum would show an homogeneous line width, which consists of the sum of all zero-phonon lines. Since the host matrix is not perfectly ordered, every embedded dye molecule will experience a slightly different local structure, which leads to a small shift of the corresponding zero-phonon line. This results in an inhomogeneous broadening of the spectrum of the dye molecules. By using frequency-modulation laser spectroscopy, with a laser bandwidth smaller than the homogeneous line width of the guest molecule, only the resonant molecules are probed. To get down to single molecule detection the laser wavelength has to be moved to the wings of the inhomogeneous line, where the number of resonant molecules will be reduced further. The idea is to reduce the density of molecules excited in the confocal volume, to reach single molecule excitation. Until now, most single molecule measurements at cryogenic conditions are performed with far-field techniques and are already a standard procedure. But not all molecules show sharp zero-phonon lines or are suited to be incorporated in a matrix and are, therefore, not suited for low temperature single molecule detection.

A different approach to perform single molecule measurements is to reduce the density of the molecules deposited on the sample surface. This can be done for room temperature as well as low temperature studies. A problem of this approach is the loss in signal intensity with decreasing sample volume.

The first single molecule experiments at room temperature were performed later, in 1993, by using an aperture-SNOM (a-SNOM) [21]. For this technique an optical fiber is etched or pulled into a sharp tip and subsequently coated with a thin metal layer. The illumination of the sample takes place via the fiber and the emitted light is collected by far field optics. Fiber illumination suffers from low signal intensity, because of the cut-off of propagating wave guide modes in the tapered fiber. Between the cut-off, which is determined by a specific fiber diameter and the aperture, the intensity decays exponentially.

The idea to implement SNOM at low temperatures is of interest, because of the reduced thermal broadening and the slow down of relaxation processes. The development of low temperature near-field microscopes has been proven to be challenging. Their design has to be optimized taking into account the operation mode and optical configuration. The first low temperature near-field microscope was introduced 1994 by Grober et al. [16]. He presented an aperture-SNOM with an optical shear-force distance detection. For the experiments the whole microscope was submerged in a bath cryostat. To investigate the optical properties of the system epitaxially grown GaAs/AlGaAs wires were observed with a probe with an aperture of 250 nm. Grober and co-workers were not able to resolve single wires, but to observe the array as a 1 μm long and 500 nm broad line. In the same year, Hess and co-workers presented a study on luminescent centers in a GaAs/AlGaAs quantum well, performed with an a-SNOM at 2 K [12]. The luminescent centers were characterized by means of magnetic field and linewidth measurements. Spectral narrow (< 0.07 meV) distinct emission lines were imaged with a spatial resolution of 100 nm. The experiments indicate, that the luminescence centers arise from excitons, localized at lateral interface roughness.

In 1997 Göhde et al. [57] used a similar system to show shear-force topography images of a 450 nm Al projection pattern at 22 K. Furthermore, single molecule measurements on SR101 dye molecules were performed at 75 K, but due to the aperture tip the resolution of the optical signal was above 200 nm, with a low detection efficiency. In the same year, a different approach using a flow cryostat and a cold finger to only cool the sample, was published by Behme et al. [19]. All other parts of the near-field setup were kept at room temperature and the whole microscope was mounted in a vacuum chamber. An additional modification, compared to the

previous designs, is the tuning fork shear-force tip-sample distance regulation. They performed topography measurements at a standard grating demonstrating a stable shear-force feedback. Further, epitaxially grown GaAs wires were observed optically with a resulting resolution of approximately 250 nm. Similar approaches were published in 1998 [58] and 2002 [59] without considerable changes in design or new results. Especially for experiments in higher wavelength regimes, the a-SNOM has the disadvantage of the limited optical transmission efficiency for aperture diameters below $\lambda/10$.

In 2000 the aperture-SNOM approach was modified by adding a terrylene doped *p*-terphenyl crystal at the end of the fiber probe to act as single-molecule active light source [60]. A tuning fork shear-force AFM was used to control the probe sample distance and a 0.8 NA objective was present to collect the emitted light. They measured the same sample, consisting of triangular aluminum islands, at different tip-sample distances. The best resolution achieved was 180 nm and it was obtained for the smallest distance.

After the development of scattering-SNOM (s-SNOM) in 2002 [61], low temperature systems based on elastic light scattering from the tip have been implemented. The s-SNOM uses the light scattered from an illuminated AFM tip, which acts as near-field probe. It is typically operated at IR frequencies and has a resolution only depending on the tip radii. In the last years this technique was used for various investigations, such as domain formations during low temperature phase transitions. For example in 2013 Yang et al. [17] observed the metal to insulator transition of V_2O_3 at 150 K in the mid-IR regime. Their microscope system is based on a dynamic force AFM with parabolic mirrors for tip illumination and light collection. All components are mounted on a flow cryostat with a titanium housing. In 2014 Döring et al. [62] combined piezoresponse force microscopy with s-SNOM to probe the two ferroelectric phase transitions of barium titanate domains at 263 K and 173 K also in the mid-IR regime. In this approach, the microscope is placed inside a vacuum tube submerged in a bath cryostat. They used an AFM with interferometric oscillation detection, which is situated outside the cryostat, and focuses the laser through a ZnSe window. The most recent experiment was performed in 2016 by Chen et al. [63], using a fiber coupled s-SNOM operating in reflection mode. The system was cooled in a He bath cryostat and the experiment was performed at 10 K. A gold and chromium coated fiber tip was fixed on a cantilever in a tapping mode conformation to investigate the carrier diffusion length in GaN nanorods. The carriers were generated by the evanescent waves, propagating from the 50 nm aperture and the resulting emission was detected via far field detection. As a result a critical diameter of 170 nm for the carrier diffusion in nanorods was determined.

In 2007 Pettinger and Steidtner presented an ultra high vacuum (UHV) TERS system, based on a scanning tunneling microscope (STM) [64]. The working principle of a STM is based on quantum tunneling. It requires a conductive probe and sample, with a bias applied between both. If the tip-sample distance is small (few Å), a tunneling current can be detected. The current depends on the z position of the tip, the applied voltage between tip and substrate and the local density of states (LDOS) of the sample [65, 66]. In the work of Steidtner et al., the STM probe is a gold tip, which also acts as optical antenna. They investigated single molecules on a monocrystalline Au substrate and observed a lateral resolution of approximately 15 nm with a Raman enhancement of $\sim 10^6$ [67]. This work was the first to acquire STM topographs together with TERS images and it fueled the development of STM-based TERS systems. The STM can not only be operated in UHV, but also at low temperatures and in 2013 the first STM-controlled low temperature TERS measurements were presented by Zhang and co-workers [52]. Their setup consists of a UHV-STM with side-illumination on a silver tip. Zhang et al. studied single porphyrin molecules on a Ag(111) substrate under liquid nitrogen cooling (80 K). They demonstrated a plasmon-enhanced Raman scattering image with a resolution of approximately 0.5 nm, the same as in the corresponding STM topograph. In a follow-up study, the group took advantage of the high resolution and distinguished two adjacent different molecules with very similar structure [68]. The same group demonstrated low temperature measurements on carbon nanotube with a resolution of 0.7 nm [7]. They correlated the change in the G band with strain variations due to bending of the nanotube.

Further, cryogenic UHV-TERS has been used to study adsorbate-substrate interactions under liquid helium cooling (19 K) [69]. TERS spectra of rhodamine 6G (R6G) on Ag(111) were taken at room and at low temperatures. A shift of the Raman peaks was observed at low temperatures and used to determine the orientation of the R6G molecule on the substrate. Altogether, STM-based low temperature TERS measurements have been shown to reach a spatial resolution down to 0.5 nm and a Raman enhancement factor up to 10^8 . This strong enhancement and confinement probably originates from the highly confined plasmonic fields in the nanogap. These gap-mode plasmons arise from the coupling between tip and substrate plasmons and only occur for metallic substrates.

In summary, three different microscope approaches for low temperature near-field measurements were developed during the last 25 years. Aperture-SNOM was the first technique to be applied for low temperatures and several designs have been published since then. None of these systems reached a spatial resolution below 100 nm and most of them suffered from a low signal intensity. Later, scattering-SNOM

microscopes for low temperature applications were developed. They allow for the investigation in the IR wavelength regime and reach higher resolutions, than the a-SNOM. These setups were mainly used to investigate temperature dependent phase transitions. The newest development in low temperature near-field microscopy is the STM-based TERS microscope. This system enables single molecule investigations at low temperature with sub-nanometer resolution and strong signal enhancement. This behavior is based on the interaction between the metallic tip and substrate, and it is limited to samples with a thickness below several nanometers, to allow for efficient coupling. Additionally, the investigation of photoluminescence is not possible, since the metal substrate would quench the PL signal.

The low temperature microscope presented in this thesis is based on a shear-force controlled tip-enhanced microscope. The sample is deposited on a transparent and dielectric substrate, for photoluminescence detection. To our knowledge no antenna-enhanced near-field experiments have been performed in this configuration at low temperatures. Since the resolution is determined by the radius of the tip, at room temperature resolutions down to 15 nm could be achieved [31]. Additionally, a higher detection sensitivity due to locally enhanced fields can be observed.

3 Single Walled Carbon Nanotubes as Model System

Single-walled carbon nanotubes (SWCNTs) can be described as hollow cylinders, formed by a rolled-up graphene sheet and consist only of sp^2 hybridized carbon atoms. Since their discovery they have been intensively studied as nearly ideal quasi one-dimensional model system. With diameters down to 0.5 nm and lengths up to several centimeters, their aspect ratio results in unique optical and electrical properties [70, 71]. These properties and the extraordinary structure of SWCNT are discussed briefly in the following sections. The last section gives an overview of the optical experiments performed on the behavior of SWCNTs at low temperatures.

3.1 Structure

The structure of a carbon nanotube is based on a rolled-up graphene sheet, resulting in a seamless hollow tube. Since there are infinite ways to wrap up graphene, a variety of SWCNT exist. The chiral index, consisting of the two numbers m and n ($n, m \in \mathbb{N}_0$), enables the description of all possible SWCNT chiralities. They can be sorted in three different groups. For zig-zag nanotubes, one of both indices equals zero and for armchair nanotubes $n = m$, both of these types are achiral. Chiral SWCNT are defined by $n \neq m$ and $n, m \neq 0$ and exist in two mirror handed configurations. Next to armchair and zig-zag, they form the largest group of SWCNT configurations.

A SWCNT can be described by its circumferential vector, which represents the direction the nanotube is rolled-up and determines the nanotube circumference. It is formed by vector addition of the two graphene lattices vectors \vec{a}_1 and \vec{a}_2 and the chiral indices, as shown in equation 3.1.

$$\vec{C}_h = n \cdot \vec{a}_1 + m \cdot \vec{a}_2 \quad n, m \in \mathbb{N}_0 \quad (3.1)$$

The roll-up along the circumferential vector and the formation of the three different types of SWCNT is presented in figure 3.1.

The chiral index can also be used to distinguish between metallic and semiconducting SWCNTs. A broad rule can classify nanotubes according to their conductivity. For all tubes with $(n - m) \bmod 3 = 0$, no band gap is present and the carbon nanotube is metallic. In contrast if $(n - m) \bmod 3 \neq 0$ is fulfilled, the CNTs are semiconducting.

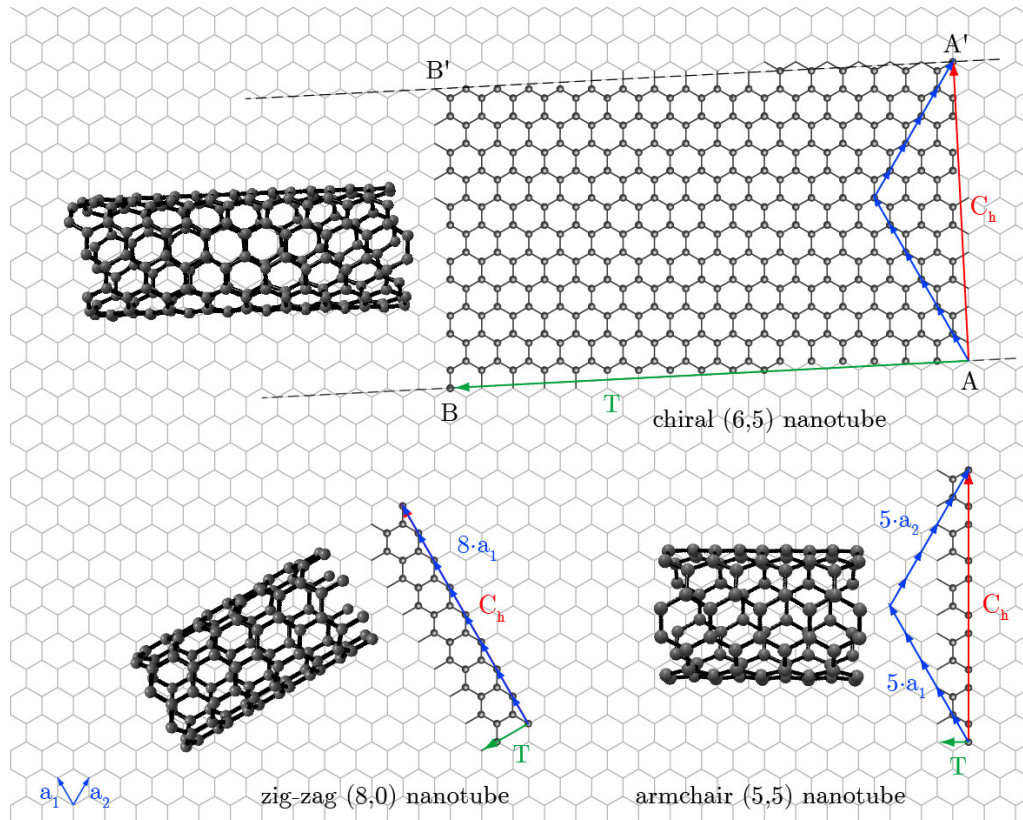


Figure 3.1: Schematic of the formation of SWCNTs by rolling-up the graphene lattice. Examples for all three types of nanotubes and the underlying graphene sheet are shown. On top, the unit cell of a chiral (6,5) nanotube is visible and by rolling it up along the circumferential vector A and A' , and B and B' connect to build a hollow cylinder. For the zig-zag nanotube on the lower left, the circumferential vector corresponds to the eight-fold of the graphene lattice vector \vec{a}_1 . The armchair nanotube on the lower right is formed like the others with the resulting chirality of (5,5). The figure shows the lattice vectors \vec{a}_1 and \vec{a}_2 in blue, the circumferential vector \vec{C}_h in red and the translation vector \vec{T} in green. Adapted from [72].

The electronic structure of a nanotube can be approximated, based on graphene by the so-called zone folding. This description takes the quantum confinement due to the quasi 1D structure of the nanotube into account, but neglects their curvature. Graphene is a zero-gap semi-metal, because in its Brillouin zone valence and con-

duction band touch at the Dirac points. When a nanotube is formed from the two dimensional graphene, the one dimension perpendicular to the tube axis is subject to quantization. The associated wave vector k_{\perp} gets quantized during the process, with n as non-zero integer (eqn. 3.2). Due to its high aspect ratio, the parallel component k_{\parallel} can be assumed to be continuous.

$$k_{\perp} = \frac{2\pi n}{|C_h|} \quad (3.2)$$

Line cuts of the 2D band structure of graphene can be taken to obtain the band structure of a SWCNT. The position of these cross sections is determined by allowed wave vectors and results in a series of subbands which form the band structure of a carbon nanotube. When a cross section contains a Dirac point, the resulting band-structure has no band gap and the nanotube is metallic. All other band structures show an energy gap at the Fermi level and, therefore, belong to semiconducting nanotubes. The resulting density of states (DOS) can be calculated from the band structure and shows sharp peaks for every maximum and minimum. These distinctive features are called van Hove singularities (vHS) and due to their large DOS, optical transitions preferably occur between this peaks.

3.2 Optical Properties

3.2.1 Photoluminescence

Semiconducting SWCNT can exhibit photoluminescence (PL) due to their direct band gap. In addition efficient Raman and Rayleigh scattering can occur for all kind of nanotubes, regardless of their band structure.

The scheme in figure 3.2 shows a simplified energy diagram for the optical transitions in SWCNTs based on the free carrier model. It presents the first and second electronic sub bands and the corresponding DOS for a single nanotube. The density of states reflects the 1D structure by showing van Hove singularities. The absorption of light is represented by the E_{22} transition where an electron and hole are created. After a fast relaxation process a radiative E_{11} transition takes place. The emission wavelength depends on the chirality of the nanotube and is usual visible in the near-infrared (NIR) to infrared regime (IR). The electronic transitions are denoted corresponding to the subbands i and j as E_{ij} . One has to distinguish between longitudinal (E_{ii}) and transversal transition (E_{ij} with $j = i + 1$), depending

on the polarization of the incident light. Longitudinal transitions are allowed for light polarized parallel to the nanotube axis, whereas transverse transitions involve perpendicular excitation and are strongly suppressed.

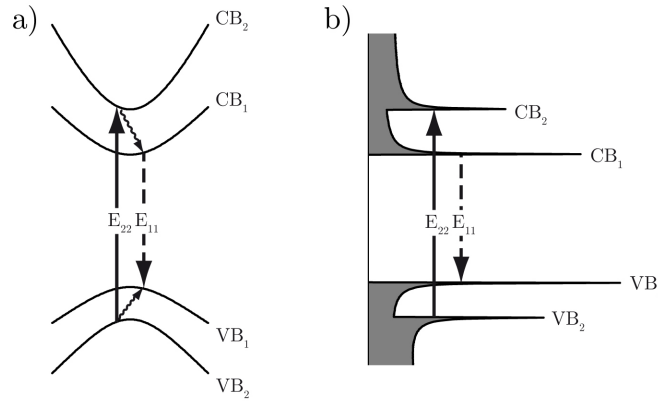


Figure 3.2: Schematic of the SWCNT band structure, in a single-particle free carrier description, with the first and second subbands (a) and the corresponding electronic density of states (b).

Photoluminescence is dominated by excitons, electron-hole bound states, that arise upon illumination. Due to the one dimensional structure of the nanotube, much stronger Coulomb interactions occur, compared to bulk semiconductors. This leads to an increased interaction between the charge carriers inside the material, resulting in a substantial deviation from the free carrier model. As consequence a shift in the optical transition energy of the photoluminescence compared to the DOS, as expected from the free carrier model, is visible. The electron-hole-attraction lowers the energy of the exciton, depending on the magnitude of the exciton binding energy. The counteracting band-gap renormalization occurs due to electron-electron-repulsion. Both interactions are in the range of several hundreds of millielectron volts and depend on the dielectric environment. The electric properties of carbon nanotubes are highly sensitive to dielectric screening since nanotubes consist only of surface atoms. Therefore, a change in the dielectric environment leads to a change in the optical response.

The two carbon atoms in the unit cell of a SWCNT result in two equivalent valleys in momentum space. Four electron-hole combinations are possible within these valleys. Two of them are responsible for direct excitons and two of them for indirect excitons. Within these four possible transitions only one is optically allowed, it is labeled “bright” exciton. The other three excitons are optically forbidden and labeled

“dark” excitons. Two of these three dark excitons can be attributed to the indirect excitons. The energy of the two remaining direct excitons is lower compared to the indirect excitons. Due to the Coulomb interactions in the SWCNT, the energy of the direct excitons is slightly different, resulting in one dark and one bright exciton. The proximity of the dark and bright state affects the optical properties of the SWCNT.

3.2.2 Temperature Dependence of Photoluminescence

The environment of a carbon nanotube can strongly influence its photoluminescence behavior. A change in temperature results in variation of photoluminescence linewidth, intensity and emission energy. In this section an overview of the experiments investigating the temperature dependence of the photoluminescence is provided [73].

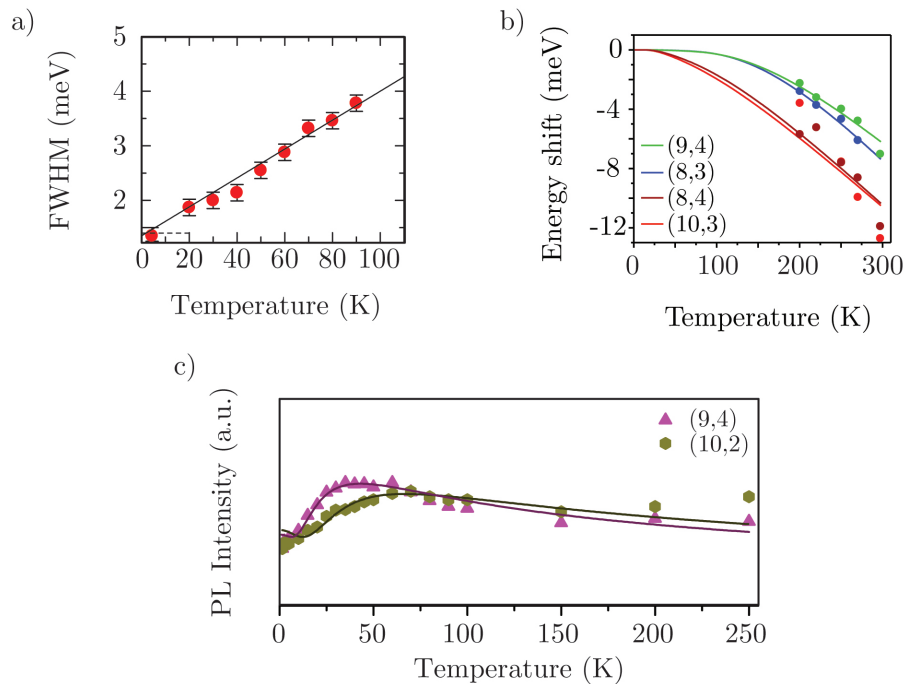


Figure 3.3: The temperature dependence of different photoluminescence characteristics are shown, based on experiments from literature. a) The graph shows the linear temperature dependence of the PL linewidth as measured by Matsuda et al. [74]. b) The representation of the energy shift of the band gap for different nanotube chiralities [75]. c) Development of the PL intensity for a (9,4) and (10,2) nanotube upon cooling [76].

PL linewidth The linewidth of a PL peak reflects the intrinsic exciton dephasing time and is extremely sensitive to its surrounding [74, 77]. The investigated nanotubes have to be single, clean and in vacuum to prevent inhomogeneous broadening. To avoid dephasing due to collision of excitons, their number needs to be kept small,

by working in a weak excitation regime [78]. Matsuda et al. [74] were able to show a nearly linear temperature dependence of the PL linewidth as visible in figure 3.3 a). The plot shows the full width at half maximum as a function of the temperature for a (10,3) nanotube. This linear behavior indicates that the exciton dephasing is dominated by the very low energy phonon modes $\ll k_B T$ and can be assigned to the twisting mode in SWCNTs.

PL emission energy The emission energy of the PL is influenced by several factors. The most important influence on the temperature dependence of the emission energy is the change in the band gap. This behavior arises due to electron-phonon interactions and has been firstly investigated for bulk semiconductors [79–81]. Recently, nanotubes were investigated experimentally and theoretically [75, 82, 83]. Measurements from Karaiskaj and co-workers [75] are shown in fig. 3.3 b). The graph presents the energy shift of the band gap for different nanotube chiralities and contains the fit of the experimental values according to reference [83]. The calculations are based on a two-phonon model and show a strong diameter and chirality dependence. Altogether, all semiconducting nanotubes exhibit a blue shift of the PL, due to an increase in band gap energy during cooling.

Also the shape of photoluminescence spectra can range from broad to narrow and from symmetric to asymmetric upon cooling. The latest study by Vialla et al. [84] attributes the drastic changes in the shape of the PL to the coupling of a localized electron to a 1D phonon bath. Small changes of the low-energy phonons result in the diversity of the PL profiles [85].

PL intensity The existence of the dark exciton state strongly affects the temperature dependence of the PL intensity [76, 86, 87]. Several temperature dependent measurements have been performed on carbon nanotubes of different chiralities, investigating the PL intensity [88, 89]. Figure 3.3 c) presents a measurement from Mortimer et al. [76] and shows the development of the PL intensity for a (9,4) and a (10,2) nanotube. The PL intensity increases with decreasing temperature, until it reaches its maximum in a region of 10-40 K. If the temperature is lowered further, a fast drop in PL intensity is observed. This behavior is representative for a variety of examined nanotubes [76]. For temperatures above 50 K the increase in intensity is dominated by the radiative decay rate of 1D excitons due to thermalization, which is approximately proportional to $T^{-1/2}$ [90, 91]. The fast intensity drop below 50 K can be attributed to the existence of the dark exciton state, slightly below the energy of the bright state. An additional observation is the dependence of the energy separation between dark and bright state on the tube diameter, which is evident in the different positions of the maxima for different nanotubes.

3.2.3 Raman Scattering

The process of Raman scattering describes the inelastic scattering of light by a phonon. It can be described by a three step process. Upon illumination a photon with ω_1 is absorbed. It scatters inelastically while emitting a phonon with the frequency ω_{ph} . Finally, the scattered photon is emitted with a resulting frequency of ω_2 . This process, when a phonon is emitted is called Stokes scattering. Anti-Stokes scattering takes place, when a phonon is absorbed and the emitted photon has a higher energy than the absorbed photon. During a Raman process energy and momentum are conserved (eqn. 3.3, 3.4). In the equation the \pm refers to Stokes and anti-Stokes scattering.

$$\hbar\omega_1 = \hbar\omega_2 \pm \hbar\omega_{ph} \quad (3.3)$$

$$\vec{k}_1 = \vec{k}_2 \pm \vec{q} \quad (3.4)$$

Single walled carbon nanotubes have a small scattering cross section, therefore, in case of single nanotube experiments only resonant Raman spectra can be observed. The spectra contain information about the phonon frequencies of the SWCNT and further allows the characterization of the nanotube in terms of doping and chirality. The most prominent Raman bands are the G band, appearing at about 1580 cm^{-1} , the radial breathing mode (RBM) at about $70\text{-}350 \text{ cm}^{-1}$, the D band at about 1350 cm^{-1} and the G' band at about 2700 cm^{-1} . The G band is associated with the C=C stretching mode for all sp^2 carbon atoms and also appears for graphene. However the line shape of the G-band splits into two features for SWCNT, due to the tube curvature. The two peaks can be used to identify metallic carbon nanotubes. The radial breathing mode is characteristic for SWCNT and has a small energy. It can be described by a breathing like motion of the carbon atoms in radial direction and leads to an oscillation of the diameter. The frequency is directly related to the diameter of the nanotube and can be used to calculate it. The D band and its overtone the G' band are present in all graphite like structures. The D mode is induced by structural defects [92].

4 Experimental Details

4.1 New Low Temperature Microscope Setup

In order to gain tip-enhanced near-field optical microscopy images at low temperatures the microscope setup needs to meet some special requirements. First, a confocal optical scanning microscope with a high numerical aperture objective, suitable for working at low temperature is required. Second, to assure small probe sample distances a low temperature tuning fork AFM for non-contact measurements is needed. It has a high sensitivity to weak forces and avoids tip damage. Third, a fast tip exchange has to be realized by short cool down and warm up times. All these points must be considered when designing a functionable and working microscope.

The resulting system is a custom build setup which was designed in cooperation with the company attocube. The microscope can be divided in two main segments according to working temperature and function. The first segment is the optical microscope head, which is situated above the cryostat on top of the microscope stick. It contains some elements for confocal imaging and different channels for the signal transmission in and out of the system. The second part is the low temperature segment, with the measurement chamber at the end of the microscope stick, which is situated in a vacuum tube. The vacuum tube has to be evacuated and is filled with low pressured Helium exchange gas, to provide thermal coupling to the surrounding liquid coolant. Afterwards it is submerged in the bath cryostat, which is filled with the liquid coolant. The low temperature segment contains a tuning fork based AFM and a low temperature suitable objective. To enable movement in all directions the sample holder and the tuning fork each sit on x, y, z positioner stacks, which enable coarse positioning and fine scanning. Both stacks can be moved independently but also synchronously. This is necessary when confocal imaging and AFM measurement are combined to obtain high resolution TENOM images. In the following sections the structure of the microscope and the operation of its main parts is explained in detail.

4.1.1 Low Temperature Microscope Optics

In general a confocal laser scanning microscope is based on an objective, that focuses the excitation beam on a small spot on the sample. An optical response is excited in the focal area and a sample image can be obtained by raster scanning the sample through the fixed probing volume. The emitted light can be collected by the same objective (epi detection) and is send to the detector after passing a confocal pinhole, to improve the spatial resolution and to suppress non-focal contributions. Alternatively, a detector with a small sensitive area can be used. To perform confocal measurements at low temperatures one has to take into account, that most optical elements do not withstand these temperature conditions. In this setup a low temperature compatible objective is used and cooled down together with the sample inside the cryostat under inert gas atmosphere. The sample is deposited on the flat surface of the solid immersion lens.

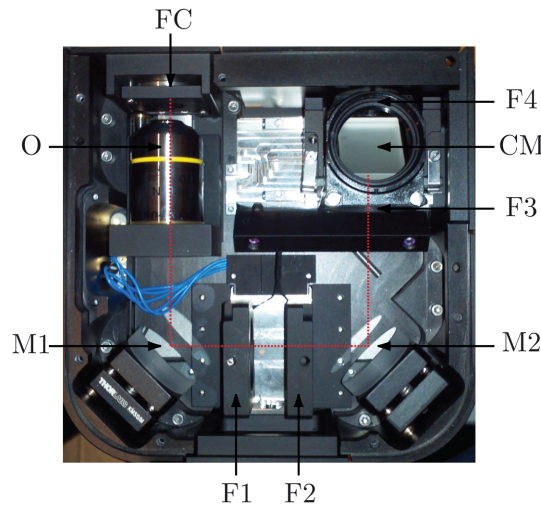


Figure 4.1: Signal channel inside the optical head.

All remaining optical elements are organized inside the optical head, that is placed on top of the cryostat and is operated at room temperature. The head consists of three measurement channels and one inspection unit. Two of the measurement channels are used for detecting the photoluminescence, either with an avalanche photo diode (APD) or to acquire spectra via a spectrometer. The third one is the excitation channel, which is used to couple a laser into the system through an optical fiber. All three channel have the same basic structure as shown in image 4.1. The fiber port (FC) connects the system with the external optics by using a FC/PC or FC/APC connector. In front of the fiber port an objective (O) is fixed on a z-adjustable mount for optimizing collimation or focusing. The mirror (M1) reflects the beam at an angle of 90 degree, through two fixed filter mounts (F1, F2) and

on a second 90 degree mirror (M2). At the end a cube mount (CM) is situated, which can be equipped with a beam splitter or a mirror according to the required properties. The cube also has two additional filter mounts (F3,F4), one on the side and one on the top. The bottom of the optical head contains the inspection channel, which can be used to image the sample surface. For this purpose it holds a webcam and a LED which can be connected to the beam line by a flippable pellicle beam splitter. In front of the exit of the head, two mirrors are installed, of which one is adjustable to assure a straight vertical exit of the laser beam.

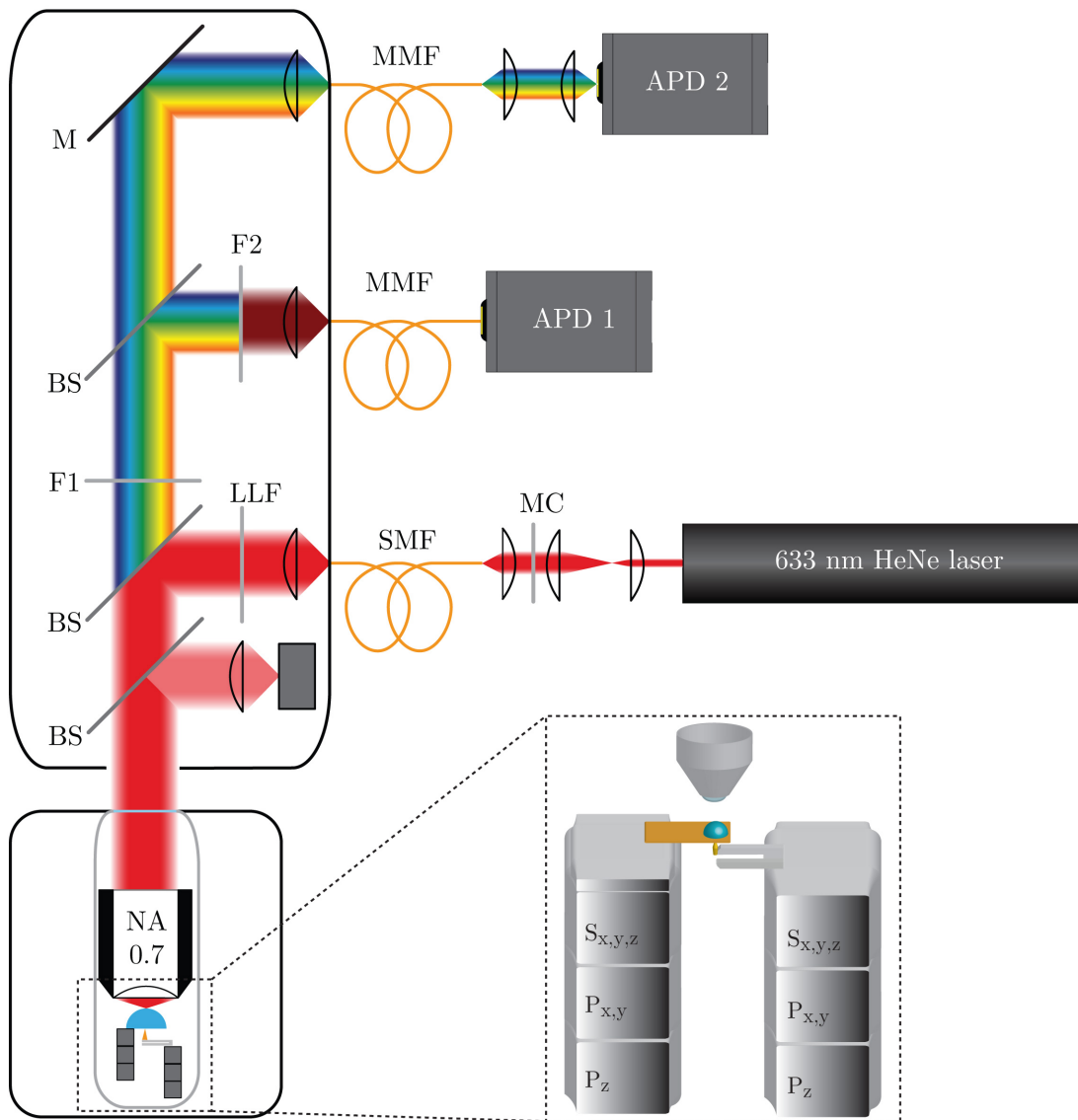


Figure 4.2: Scheme of the low-temperature near-field optical microscope setup.

The scheme in figure 4.2 shows the beam path of the whole microscope. The excitation beam of the HeNe laser (632.8 nm) is expanded by a set of lenses ($f_1=30$ mm; $f_2=100$ mm) and passes a liquid crystal mode converter (ARCOptix) to convert the laser mode into a radially polarized doughnut mode. To maintain the polarization a polarization maintaining panda fiber (Thorlabs, PM780-HP) is used to couple the laser into the optical head. Inside the head the objective (Olympus Plan N 4x / 0,1NA ∞ / - / FN 22) collimates the beam, before it is passing a laser line filter (Semrock, 632.8 nm MaxLine[®] laser clean-up filter). The laser beam is reflected by a beam splitter and vertically send down into the low temperature segment, through a vacuum optical window. Here, a low temperature objective (LT-IWDO, NA=0.68, WD=1.61 mm) focuses the beam on a solid immersion lens on which the sample is deposited. The optical signal is collected by the same objective and travels back up to the optical head. After passing the excitation beam splitter, the residual laser light is blocked by a 633 nm long pass filter (Semrock, 632.8 nm EdgeBasic[™] long-pass edge filter). To divide the final signal equally between the two detection channels a broadband 50:50 beamsplitter is situated in the lower of both cube mounts. The beamsplitter reflects one half of the signal into the first detection channel and transmits the other half, which reaches the the upper detection channel. Both channels have an identical architecture, they use an Olympus Plan 10x objective (Olympus Plan N 10x / 0,25NA ∞ / - / FN 22) to couple the signal via a multi mode fiber (MMF, wavelength range 400-2400 nm, core 105 μ m) into the respective detector. The first or lower detection channel is connected to an APD (Laser Components, COUNT-250N). For photoluminescence imaging of CoMoCAT nanotubes (see section 3) a 863 nm or a 950 nm long pass filter (Chroma, 863LP; Thorlabs, FEL0950) was inserted into this APD detection channel. The upper detection channel can be connected to a second APD or a spectrometer to analyze the spectral composition of the signal. By using a second APD without additional filters the second channel can be used to monitor the gold photoluminescence during tip centering. The signal of both APDs is fed into the microscope controller by using two different input connectors. The first APD, responsible for imaging the nanotube photoluminescence, is connected to the counter input of the ASC 500 and records the signal intensity in counts. Since there is only one of this counter connectors, the second APD is connected by using a ADC input of the ASC 500. This input records a voltage value, that is proportional to the detected signal intensity.

An additional beam path introduced within this thesis work, is not shown in image 4.2 for clarity reasons. This path was introduced to illuminate tip and SIL from below. After the laser a flipable mirror is mounted to guide the light into a second fiber. By using a bare fiber connector (BFT1, Thorlabs) the light is coupled

into a bare 633 nm fiber. This fiber is thin enough to pass the feedthrough and enter the microscope. The entrance is sealed with an epoxy polymer, that keeps the fiber fixed in place. Inside the microscope the fiber is guided down along the microscope stick. At the bottom the fiber is fixed at the lower part of the sample holder. With this the whole area below the SIL is illuminated. The tip casts a shadow on the SIL surface, which can be imaged by the webcam in the inspection channel. This construction enables the centering of the tip in the focus.

SIL

The solid immersion lens is a crucial part of the setup and, therefore, this section will give an overview on its properties. The discussion of the antenna properties in chapter 2.2.1 showed, that the directivity of an antenna is important for efficient signal enhancement. In fact, as a consequence the antenna not only enhances the spontaneous emission rate, but also influences the direction of the radiation and changes the angular radiation pattern. Every dipole that emits into the surrounding medium shows a characteristic angular emission pattern, which contains information about its orientation. In reference [93] the authors could show the radiation pattern of a single photoluminescent carbon nanotube and the influence of the antenna on this pattern.

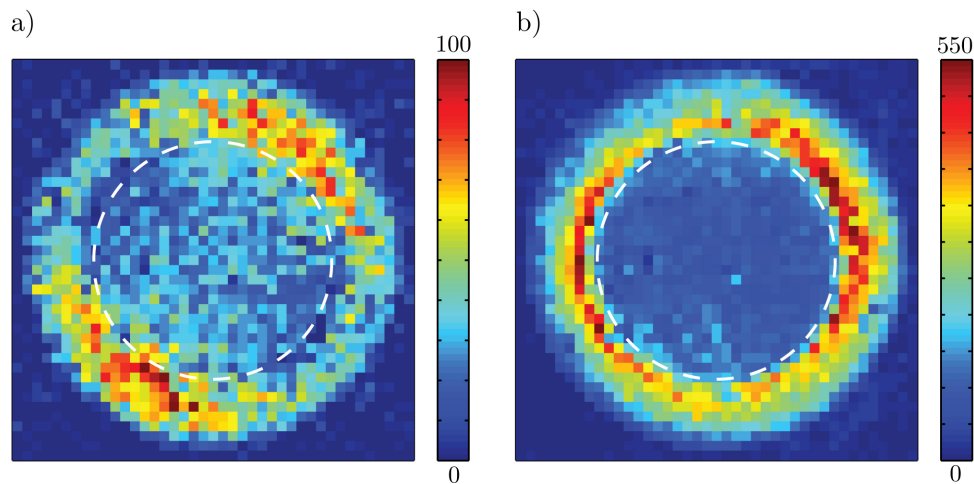


Figure 4.3: Angular radiation pattern of a photoluminescent SWCNT a) without and b) with the influence of an antenna. The dashed line in the patterns marks the circle where $NA=1$ [93].

In figure 4.3 the corresponding radiation patterns are displayed, where 4.3 a) is the pattern without and 4.3 b) the one with antenna. The dashed line in the patterns marks the circle where the numerical aperture is unity. The undisturbed photoluminescence pattern of the SWCNTs shows two lobes parallel to the nanotube

orientation. The highest signal intensity is situated in the outer ring near the critical angle. This shape can be modeled by an in-plane dipole in good agreement with the data. The optical antenna induces two major changes as seen in image 4.3 b). First, by comparing the intensity scale, a five times increase due to the signal enhancement is visible. Secondly, the angular intensity distribution has changed. The initially visible double lobe pattern is almost completely superimposed by a sharp ring which can be described by a vertically oriented dipole [94]. It is important to notice, that the main part of the intensity is emitted near the critical angle, above a numerical aperture of one and, therefore, a high numerical aperture is needed to collect the enhanced signal [95, 96].

Immersion lenses have been invented to increase the collection efficiency and accordingly improve the resolution of microscopes. There are two kinds of immersion lenses, namely the liquid and the solid immersion lens (SIL). Both types use index matching to increase the magnitude of the detectable in-plane component of the wave vector and to reduce refraction of light, that is associated with loss of information. For ambient conditions oil or water objectives are used, but these are not suitable at low temperatures and under vacuum. A convenient alternative is the solid immersion lens, that also works in non-ambient environments. It is a half ball shaped lens consisting of a high refractive index material.

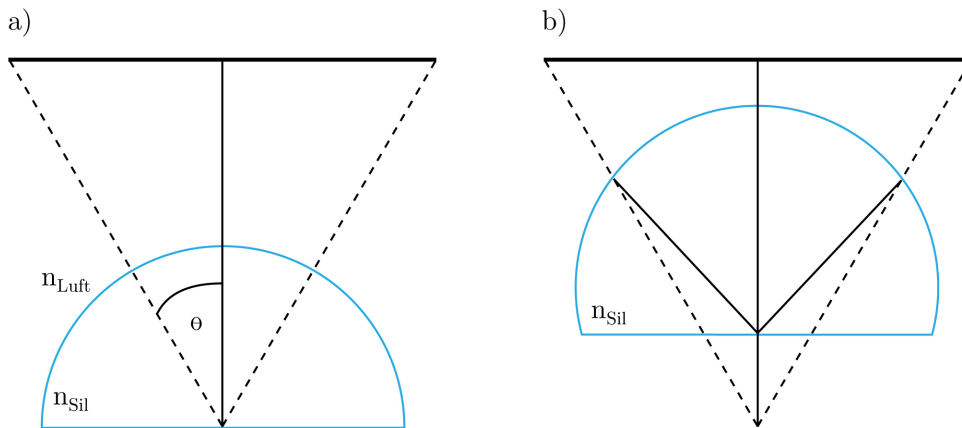


Figure 4.4: Types of solid immersion lenses. a) Plano convex lens, where the beam is directly focused on the flat surface. b) Super-SIL, where the light is focused at R/n below the center of the sphere [97].

The first SIL microscope was documented by Mansfield and Kino in 1990 [98]. The initial application was for optical storage, but soon it also was used in physics and nanoimaging [99–101]. The idea is to focus a beam through the lens to form a spot at its flat side. The resulting spot size is decreased by $1/n$ where n is the refractive index of the solid immersion lens. Later, a second type of SIL was proposed, the so-

called super-sphere or super-SIL. It has its focus below the center of the sphere, based on the idea that one can focus a beam inside a sphere at a distance of R/n . Both types of lenses are shown in figure 4.4. The super-SIL has a higher magnification, namely n^2 versus n , but it is less tolerant regarding spatial deviations and shows strong chromatic aberrations [97, 102].

In the following, only the standard hemisphere solid immersion lens will be discussed, since it is used in the present low temperature setup. As mentioned the SIL improves the numerical aperture and, therefore, the resolution by a factor of n_{SIL} . This means the SIL is also able to collect a broader spectrum of the in-plane wave vectors and higher radiation angles. Since the beam always enters the SIL normal to the surface, according to Snell's law no additional refraction at the air - SIL interface takes place. If the incoming beam impinges on the flat surface of the SIL with an angle above the critical angle θ_{crit} , the rays undergo total internal reflection (TIR), under the condition that the surrounding medium has a smaller refractive index than the SIL. Due to total internal reflection local evanescent waves are produced at the focus point and this is the reason SIL microscopy is also referred to as near-field microscopy [103, 104].

The field distribution inside the solid immersion lens is object of several publications, which show theoretical as well as experimental data [105–108]. In reference [109] Vamivakas et al. developed a theoretical description to compare the fields in the focal plane of an objective in presence and absence of a SIL.

Figure 4.5 shows the intensity distribution of a Gaussian beam, based on the calculation of Vamivaks et al. [109] modified for our setup values. The setup properties used are: a wavelength of 633 nm, a working distance of 1.61 mm, a numerical aperture of 0.68 and the refractive index of the SIL of $n_{SIL}=2$. As result the fields in the focal plane of the same objective focusing into air (fig 4.5a) or on the flat surface of the SIL (fig 4.5b) are calculated. As discussed above the gain with respect to lateral spatial resolution depends on the refractive index of the SIL. In our case the SIL is expected to improve the focus by a factor of $n_{SIL} = 2$. This influence is clearly visible by comparing both intensity distributions shown in the image. For better comparison the cross section of both distributions is shown in Figure 4.5c). The SIL allows to collect a wider range of in-plane wave vector components and, therefore, yields an intensity higher, than compared to the focus in air. The full width at half maximum of the curves additionally pronounces the difference in spot size, as it decreased for the focus with SIL by a factor of $n_{SIL} = 2$.

The effect of the SIL strongly depends on the distance of the sample material to the SIL surface and on the refractive index of the material in between. The fields in the

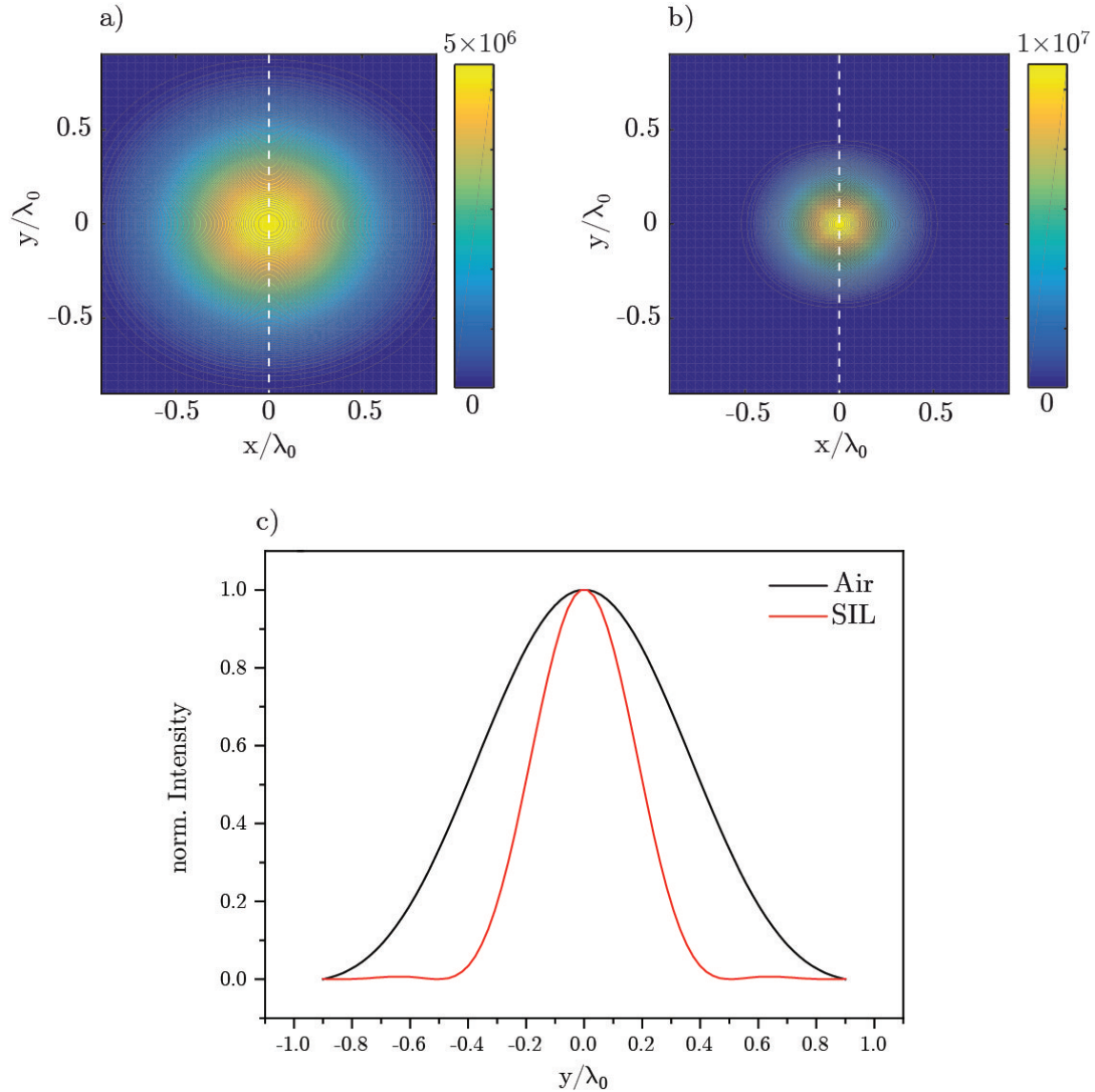


Figure 4.5: Representation of the intensity distribution of a focused Gaussian beam in the focal plane a) in air b) with SIL. The calculation is based on a MATLAB script described in reference [109]. It was modified according to the setup values with $\lambda = 633$ nm, $n_{SIL} = 2$ and the objective specifications with $NA = 0.68$ and a focal length of $f = 1.61$ mm. The cross sections along the dashed white line are plotted in c).

air gap decay rapidly, resulting in a broadening of the spot and an overall intensity loss. Calculations show that the spot size increases by about 10% for a 100 nm air gap [98]. For the same distance the intensity of evanescent waves falls off strongly to about 73%. Since propagating waves decay slower, the overall intensity loss for a 100 nm air gap is about 50% [108]. To gain the best resolution and avoid loss in intensity the sample material has to be deposited directly on the SIL surface.

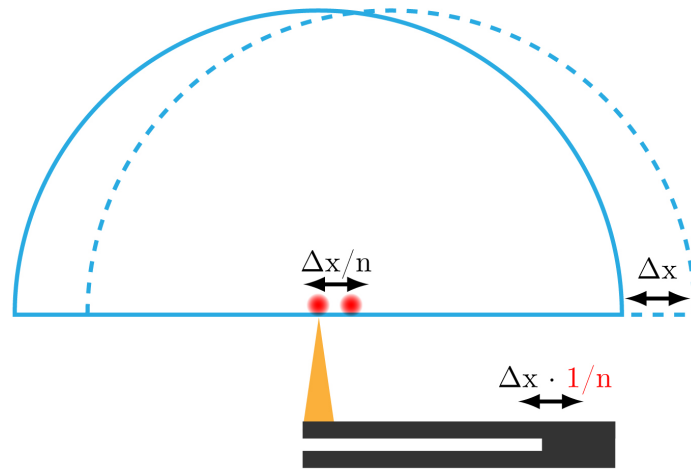


Figure 4.6: Synchronous scanning: The path difference between the movement of the tip and the focus can be overcome, by including a factor (in red $1/n_{SIL}$) to modify the tip scan movement. Using this approach, the tip can be kept in the center of the laser focus while the SIL is scanned to image the sample.

Due to its properties, in literature the solid immersion lens has been mainly used to improve the spatial resolution of conventional confocal microscopes. In our case, the increased collection angle is crucial to collect the tip enhanced signal and gain near-field information.

The use of the SIL increases the amount of collected in-plane wave vector components but it also induces a new problem, the path difference as shown in figure 4.6. During the measurement, SIL and tip are scanned synchronously for a certain distance Δx but the focus on the flat side of the SIL moves a shorter distance. This path difference is defined by the refractive index of the SIL (n_{SIL}) as $\Delta x/n_{SIL}$. To perform a near-field experiment it is crucial to keep the tip centered in the focus of the laser, but this is not possible under these circumstances. A way to change the path difference between tip and focus, is to introduce a factor that adjusts the tip movement accordingly. This is done by the software feature, synchronous scan, where the factor is defined by the reciprocal value of the refractive index of the SIL.

The synchronous scan is an essential part of the system and the reason why two independently moving scanner stacks are present. Without the synchronous scan, the path difference introduced by the SIL could not be compensated and a tip-enhanced near-field measurement wouldn't be possible in this configuration.

4.1.2 Low Temperature Atomic Force Microscope

For TONOM measurements sharp gold probes can be used, to act as optical antenna and as AFM tip. Since gold is extremely soft, the tip has to be handled with great care, without applying high forces to it. Tuning fork based AFMs have been used in order to preserve the tip from damage and being able to detect slightest changes in the interaction force. Due to its high stiffness the tuning fork has a small oscillation amplitude. A further advantage of the quartz tuning fork is that its vibration can be monitored directly without using an external laser-based detector scheme. The piezoelectric effect of the quartz transduces the mechanical vibration into an electrical signal, which can easily and precisely be detected.

The quartz tuning forks used in the microscope, are the same as those used in watches. The oscillation of the tuning fork has a very small amplitude and a resonance frequency of 32.768 Hz (2^{15} Hz). For the measurement, the tip is glued perpendicular on the front of the upper prong. Due to the change in mass, the resonance frequency of the tuning fork-tip ensemble shifts to lower resonance frequency values and reduces the quality factor (Q) of the resonance.

The low temperature AFM setup can also be operated at room temperature. On the AFM head a dither piezo is glued near the tuning fork, to excite it at its resonance frequency. The vibration induces a small current in the tuning fork, which correlates with the amplitude and phase of the oscillation. The tuning fork is soldered to a small circuit board, which is connected with a coaxial cable that guides the signal out of the microscope. Afterwards, the current is converted and amplified by a FEMTO[®] charge amplifier with a gain factor of 10 V/pC. The resulting signal is fed into the ASC 500 lock-in amplifier.

For small amplitudes the oscillation can be described by a forced, damped harmonic oscillator with a periodic excitation at ω_a and a force F . The solution of the equation of motion results in the complex amplitude as shown in equation 4.1.

$$A(t) = \frac{F/m}{\omega_0^2 - \omega_a^2 - i\omega_0\omega_a/\sqrt{3}Q} e^{-i\omega_a t} \quad (4.1)$$

The real part of the amplitude can be represented by the following equation:

$$A(t) = |A(t)|e^{-i\phi} \quad (4.2)$$

where ϕ is the phase shift between excitation and deflection.

If a force is acting on the cantilever, a change in the resonance frequency ω is induced. This leads to a decrease in amplitude and a phase shift. Based on these parameters there are two main operation modes in dynamic-mode AFM: amplitude- and frequency-modulation AFM. For the first mode, the tuning fork oscillates near its resonance frequency and the tip-sample interaction is detected by a change in amplitude [110]. A change in oscillation amplitude can be induced by a frequency shift (conservative interaction with elastic forces), as well as by damping due to dissipative forces. In the amplitude detection mode, one can not distinguish between conservative and dissipative interaction [111]. For frequency modulation the shift in resonance, induced by conservative interactions, is used as feedback. It was first introduced by Albrecht et al. in 1991 [112], for improving measurements in a vacuum environment. In this environment the oscillation has a high Q factor, that makes the time response of the oscillation extremely slow and would lead to a delay in amplitude feedback response. Both operation modes are used complementarily, depending on the experimental conditions [113].

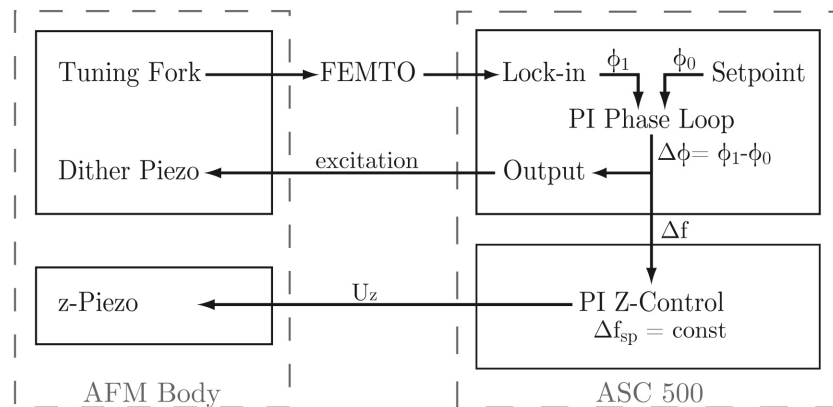


Figure 4.7: Frequency-modulation AFM. Schematic layout of the working principle of the PLL detection and the z-control loop inside the ASC500.

For low temperature conditions the frequency-modulation AFM is more suitable. A phase-locked loop (PLL) is used to detect the frequency shift Δf of the oscillation. The PLL detector compares the phases between the tuning fork output signal (ϕ_1), which is fed into a lock-in amplifier and a setpoint (ϕ_0). To keep a constant phase shift $\Delta\phi$, the excitation frequency is adjusted. In a simple theoretical model, the frequency shift Δf is proportional to the gradient of the force dF/dz . The PL loop feeds the signal into a PI controller or in this case the z-control loop. The z-control loop controls the tip-sample distance by keeping the frequency shift Δf_{sp} constant. By applying a voltage U_z to the z-piezo, the tip-sample distance is changed until the setpoint is reached. A schematic overview of the working principle is shown in

figure 4.7. It represents the layout of the low temperature setup, where PLL and z-control loop are part of the ASC 500.

Q Control

An important property of every harmonically oscillating system is the quality factor. It describes the damping of the system and scales with the spectral width of the resonance curve. It is defined as:

$$Q = \frac{\omega_o}{\Delta\omega}, \quad (4.3)$$

where ω_o is the resonance frequency and $\Delta\omega$ is the full width at half maximum (FWHM) of the resonance curve. The quality factor depends on the mechanical properties of tuning fork (e.g. mass, stiffness), its mechanical connection to the scan head, typically realized by soldering, the mass of the tip and the environment. The Q factor determines the sensitivity of the force detection and the maximum speed of a scan. Compared to ambient conditions, at which the Q factor of the bare tuning fork is on the order of 10^4 , the quality factor increases when the system is operated in vacuum or at low temperatures reaching $10^5 - 10^8$. In this environment, the influence of the quality factor leads to an extend in lifetime ($\tau = 2Q/\omega_o$) of the transient state of the motion. In other words the damping of the oscillation is so low that it leads to a delay in the feedback response. In contrast, the quality factor is decreased in a liquid environment leading to a loss in sensitivity.

In 1993 Mertz et al. [114] introduced the possibility to control the quality factor of a cantilever in a systematic manner, to improve the scan characteristics. The so called Q control allows to adapt the quality factor, depending on the environmental requirements. This is accomplished by adding a periodic driving signal to the excitation frequency, with the appropriate phase. To compose this final excitation signal, a signal adder is used. It consists of two parts: The fixed excitation at the resonance frequency and a second part, which is developed from the tuning fork output signal. After demodulating the tuning fork signal in the lock-in amplifier, the obtained phase and amplitude are used to construct this second part. Phase and amplitude are fed into a phase shifter or a gain amplifier. The phase shifter adjusts the phase according to the manual input and determines whether the damping of the system is enhanced or reduced. The feedback gain defines the amplitude of the excitation signal. Afterwards an oscillation generator creates a new oscillation signal from the now modified signal components.

In reference [115] a theoretical description of active Q control in a tuning fork based AFM is presented. To describe the tuning fork an equivalent circuit model, also called Butterworth-Van Dyke circuit is used. This consists of a parallel circuit containing an LRC unit and a capacitance C_0 . By applying a mechanical model, one can relate every parameter: the inductance L stands for the effective mass, the resistor R describes the dissipative process and the capacitance C models the spring constant [116]. The additional capacitance (C_0) is simply defined by geometry, contacts and cables. By employing these parameters into the equation of motion, the effective quality factor Q' can be approximated as

$$Q' = \frac{Q}{1 - |\bar{G}|(\bar{C}_0 \sin\theta + Q \cos\theta)}, \quad (4.4)$$

with $\bar{C}_0 = C_0/C$ and $\bar{G} = GR_0C\omega_0$. This equation can be used to derive a simple correlation between the change of Q' and the applied phase. Q factor enhancement takes place by adding a phase shift in the range of θ_1 to $\theta_1 + \pi$ and a decrease of the Q factor in a range of $\theta_1 + \pi$ to $\theta_1 + 2\pi$ with respect to the driving signal. Here, θ_1 is a characteristic constant of the tuning fork and is calculated by $\tan\theta_1 = -Q/\bar{C}_0$.

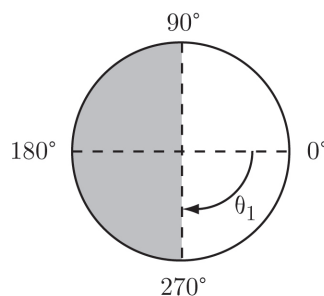


Figure 4.8: Q control phase map to represent the change in Q factor for a given phase shift, for the tuning fork system with an intrinsic phase shift of $\theta_1 = -89.7^\circ$. The gray area indicates where Q is deduced and the white are where it is increased.

For the tuning forks used during the measurement, $\bar{C}_0 = 460$ and $Q = 90000$, so θ_1 can be calculated giving a value of -89.7° . The resulting behavior of Q' , relative to the applied phase is shown qualitatively in the map in figure 4.8. This phase map represents the change of the Q factor in dependence of the applied phase lag, for the system with a calculated shift of $\theta_1 = -89.7^\circ$. The gray area indicates where the Q factor is decreased by Q control with a maximized damping at approximately 180° . In contrast, the white region represents an increase in the Q factor, which should be highest at 0° . The Q factor at 90° and 270° should show the same value.

Image 4.9 shows the behavior of the amplitude and the phase curve for active Q control with different phase shifts at low temperatures. The curves were recorded

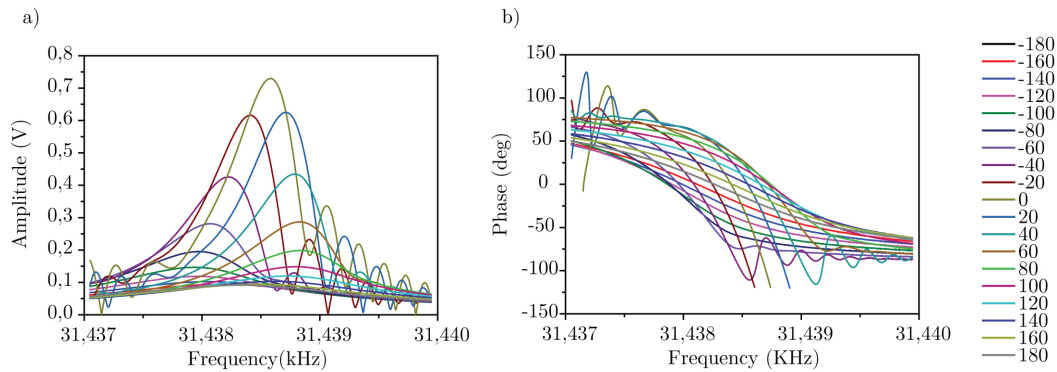


Figure 4.9: Amplitude and phase resonance curves of a tip-tuning fork system for different Q control phase shifts at a constant gain of 0.99. The curves were recorded at low temperature conditions (77 K) with an excitation amplitude of 220 mV and a resonance frequency of 31.44 kHz. The phase shift was varied from -180° to 180° in steps of 20° . a) Amplitude vs. frequency curves with Q factors between 17179 and 46233. b) Simultaneously recorded phase curves.

by changing the phase shift from -180 to 180° in steps of 20° . Within this range the quality factor was tuned from 17179 to 46233. For the smallest quality factor the highest damping takes place and the amplitude curve is broadened. In contrast, for the largest quality factor the amplitude curve has the smallest width and the highest maximum. Both extremes show approximately the same resonance frequency, which also matches the resonance frequency of the uninfluenced oscillation (not shown). The phase difference between maximum enhancement and minimum reduction of the Q factor is exactly 180° . Additionally to the change in Q, all curves in between exhibit a shift of the resonance frequency. In the complete phase range, one can see that the maximum of the amplitude curves describe a full circle. A corresponding behavior can be observed for the phase curves. The steepness of the phase varies with increasing or decreasing Q factor. The phase for the highest damping has the smallest slope and vice versa. Also a shift along the frequency axis with changing Q factor is observed.

Gold Tip Fabrication

The gold probes were etched electrochemically from a solid gold wire (Chem-pur, 99.995%, 100 μm diameter) in fuming hydrochloric acid (Fluka Analytical, 37%) [117–119]. This method can produce gold tips down to 15 nm in diameter. The characterization of the tips was performed by scanning electron microscopy (SEM). An example picture is shown in Figure 4.10 b). For the etching process, the gold wire serves as anode and an additional platinum ring acts as counter elec-

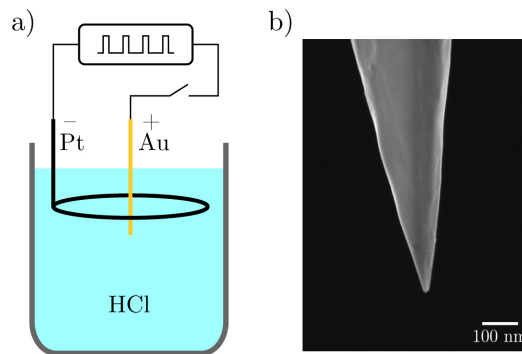


Figure 4.10: a) Scheme of the setup, used for electrochemical etching of sharp gold tips. The gold wire acts as anode and the platinum ring as cathode. Both wires are submerged in hydrochlorid acid and electrical pulses were applied. The oxidation of the gold leads to a decrease of the wire diameter and the formation of a chloroaurate complex. b) SEM image of an etched and cleaned gold tip with a diameter of about 15 nm.

trode. Both wires are dipped into a cuvette filled with hydrochloric acid as visible in figure 4.10 a). By closing the circuit electrical pulses with a duration of 50 μs , a repetition rate of 3 kHz and an amplitude of 4 V (BK Precision, 4003A) are applied, leading to an oxidation of the gold. A tetrachloroaurate complex is formed at the anode and the consumption of the gold leads to a decrease in the wire diameter. At the cathode the hydronium ions are reduced to hydrogen, which results in gas formation at the platinum wire. An optical microscope is used to observe the tip formation and to stop the process at the right time. After removing the etched wires from the acid they are rinsed in distilled water to clean it from impurities.

4.1.3 Electronics

Some electrical connections and main control electronics have already been mentioned in the previous chapters, but for a better overview and understanding the most important parts and connections are explained briefly in this section.

There are four electronic components responsible for controlling all movements inside the microscope and for signal detection. The ASC 500 is the key controller. It is responsible for the x,y,z scanning piezos of the sample stack and the z-piezo for tip height control. It also controls the tip approach, by sending the approach trigger and monitoring the PLL and z-control feedback loops. The ASC 400 is responsible for controlling the x and y scanning piezos of the tip stack. Two ANC 250 voltage

amplifier are present, each connected to either the ASC 500 or ASC 400. They multiply the incoming signal with a factor of 20 and send the amplified signal to the break-out panel. The ANC 350 is a position controller and drives all six piezo-driven stepper motors used for coarse positioning. It also reads out the position by measuring the change in resistance of the resistive sensor.

The corresponding scheme in fig. 4.11 shows how these electronic components are connected. The upper row represents the break-out-panel, which connects the microscope to all electrical components. There are six multi pin (12 pin) cables plugged in between microscope and break-out-panel and they are sorted according to the signals they send or receive. The first break-out panel is responsible for the connection of the Lakeshore 335 temperature controller with the temperature sensor and the heater, which are both situated on top of the sample stack. The second panel get the signals for the rough positioning and fine scanning of the sample stack, from the ANC 250 and the ANC 350. Panel three is entirely responsible for the sensor readout of the ANC350 for all six positioners. Panel four is similar to panel two, it is responsible for the rough positioning and fine scanning of the tip stack. Panel five directs the tuning fork excitation signal from the ASC 500 to the dither piezo on the tip stack. The tuning fork output signal is not connected via the break-out panel. It is directly fed into to the FEMTO voltage amplifier and afterwards send to the ASC 500. The complete system is grounded via panel 6.

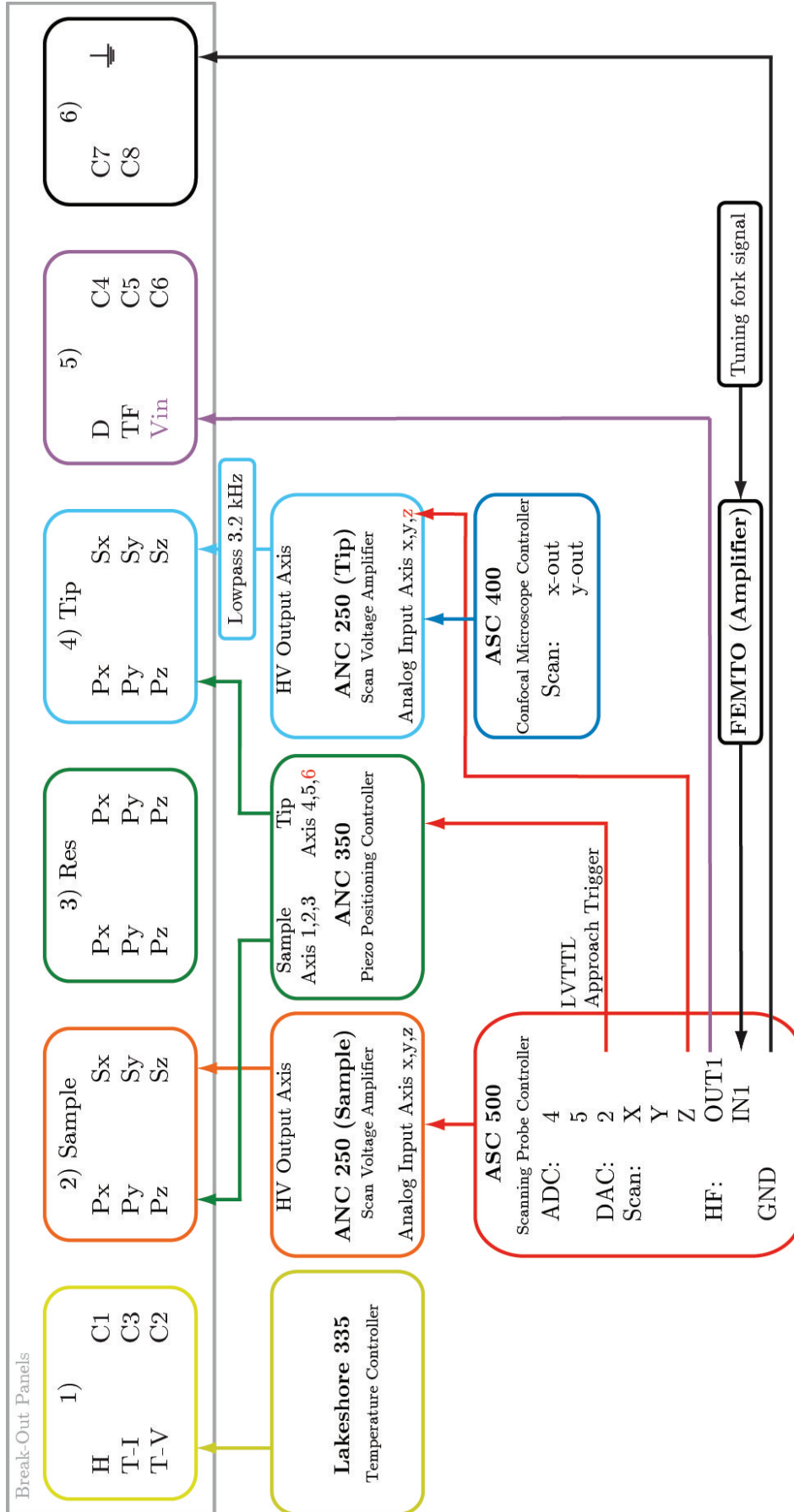


Figure 4.11: Connection scheme of the electronic components.

4.2 Sample Fabrication

For all measurements the sample material was deposited on the flat side of a solid immersion lens. The used half ball lenses have a diameter of 3 mm and are made from lanthanum dense flint glass (LaSF-35) with a refractive index of 2 (Sandoz Filz SA, Swiss). This solid immersion lens showed the best surface quality ($R_a=0.5$ nm) in combination with a desired high refractive index (see section 5.1.1).

The carbon nanotubes used, were produced by chemical vapor deposition (CVD) using cobalt and molybdenum as catalysts (CoMoCAT) and purchased as powder from Sigma-Aldrich. The material is a mixture of several chiralities, but mainly contains (6,5) SWCNTs. Due to their small size, strong van der Waals forces interact between the nanotubes, which leads to the formation of bundles. To prevent bundling and increase solubility surfactants were used. These surfactant molecules exhibit a polar and a non-polar end group. The non-polar part interacts with the nanotube forming a micelle to bring the polar part in contact with the solvent.

For the preparation of the CoMoCAT sample, Sodium deoxycholate (DOC) was used as surfactant. 0.5 mg of CoMoCAT were dispersed per 0.5 ml DOC solution (1wt% in water). To separate the nanotubes the dispersion was sonicated over 20 min with 15% power (Bandelin Sonopuls HD2200/UW2200) under ice cooling. Afterwards the samples were centrifugated for 60 min at 12000 rpm to separate from undissolved components. The obtained supernatant was transferred to a new vessel. The suspension was drop-casted or spin-coated onto the flat side of the SIL followed by rinsing with water and methanol.

5 Results and Discussion

In the following chapter the properties of the microscope are described and analyzed in detail. In the first part of this section, the focus lies on the introduction of the SIL into the system. The solid immersion lens is responsible for collecting the tip enhanced light, which is emitted at large angles. The idea to use it in a low temperature TENOM is new and its influence on the system has to be monitored. One consequence of the usage of the SIL is the path difference between the movement of the focus and the tip. To compensate for this problem, the synchronous scan is introduced and suitable scanning parameters have to be found. In the second section the low temperature tuning-fork AFM is described. As mentioned before changes in the environment strongly influence the resonance properties of the tuning fork-tip system. Therefore, the change of the Q factor and the effectiveness of Q control is studied. Additionally, the stability of the feedback and the resolution properties of the AFM at low temperatures are examined. The developments towards the first low temperature tip-enhanced near-field measurements are presented. And finally the first TENOM measurements at 77 K are shown and discussed.

5.1 Characterization of the Solid Immersion Lens

The use of the SIL increases the range of collected wave vectors which should lead to an improved resolution. Additionally, the SIL acts as sample substrate and, therefore, has to meet special requirements. The surface properties of the SIL in connection with its refractive index is characterized to select a suitable SIL for the low temperature measurements. Since the sample material is directly deposited on the SIL, one has to ensure that its surface is as flat and smooth as possible. Scratches on the SIL would lead to an accumulation of nanotubes in it. If these valleys are deep enough, the tip can be damaged while scanning over it. The usage of the SIL introduces a new problem: the path difference between the movement of the laser focus and the tip. To overcome this problem two scanner are present, which move SIL and tip independently. They are controlled by the so-called synchronous scan. In this section the synchronous scan is tested and the parameters needed to keep the

Table 5.1: Properties of the investigated solid immersion lenses.

Name	refractive index n	material	supplier
Zirconia	$n=2.177$	cubic zirconia ZrO_2	A.W.I. Industries
S-LAH71	$n=1.850$	lanthanum dense flint glass	Sandoz fls SA
LASFN-35	$n= 2.022$	lanthanum dense flint glass	Sabdoz fls SA

tip in focus are optimized. Low temperature confocal scans of the carbon nanotube photoluminescence are performed to investigate the optical resolution.

5.1.1 Surface Characterization

The solid immersion lens has to meet several quality criteria to be suited for the planned low temperature TENOM measurements. To fit in the sample holder, the diameter of the SIL has to be below 3 mm. The refractive index of the lens should be as high as possible, since the numerical aperture is improved by the factor of n_{SIL} . To ensure a stable and background free topography the surface of the SIL has to be as smooth as possible. Large scratches can lead to a damage of the tip during scanning. In addition, during sample deposition the nanotubes tend to fill the valleys, which would hinder a homogeneous distribution of single nanotubes on the substrate.

Three solid immersion lenses were investigated as possible candidates for the following near-field studies. In table 5.1 the tested solid immersion lenses and their properties are summarized.

The results of the investigation on the surface quality of the SILs are assembled in figure 5.1. First, all lenses were inspected with a camera with a magnification of 3.5 and afterwards AFM scans were performed. The optical inspection already revealed significant differences between the SILs (fig. 5.1 a-c). The Zirconia SIL shows a clear pattern of randomly distributed straight lines. The other two Lanthanum glass lenses do not exhibit any comparable pattern and look more smooth. Additionally, all SILs showed black spots, which occur from contaminations on the surface. They could be residuals of the AFM preparation process. After the optical inspection several AFM scans were performed on the lenses. For every lens one representative topography image and the corresponding cross section are shown in figure 5.1 d-i). The surface of the Zirconia SIL is completely covered with scratches of different width and depth. These straight lines are randomly distributed and probably the result of rough polishing. The cross section in figure 5.1 g) shows scratches as deep as 60 nm and with a width up to 0.5 μm . The S-LAH71 lens has a much smoother

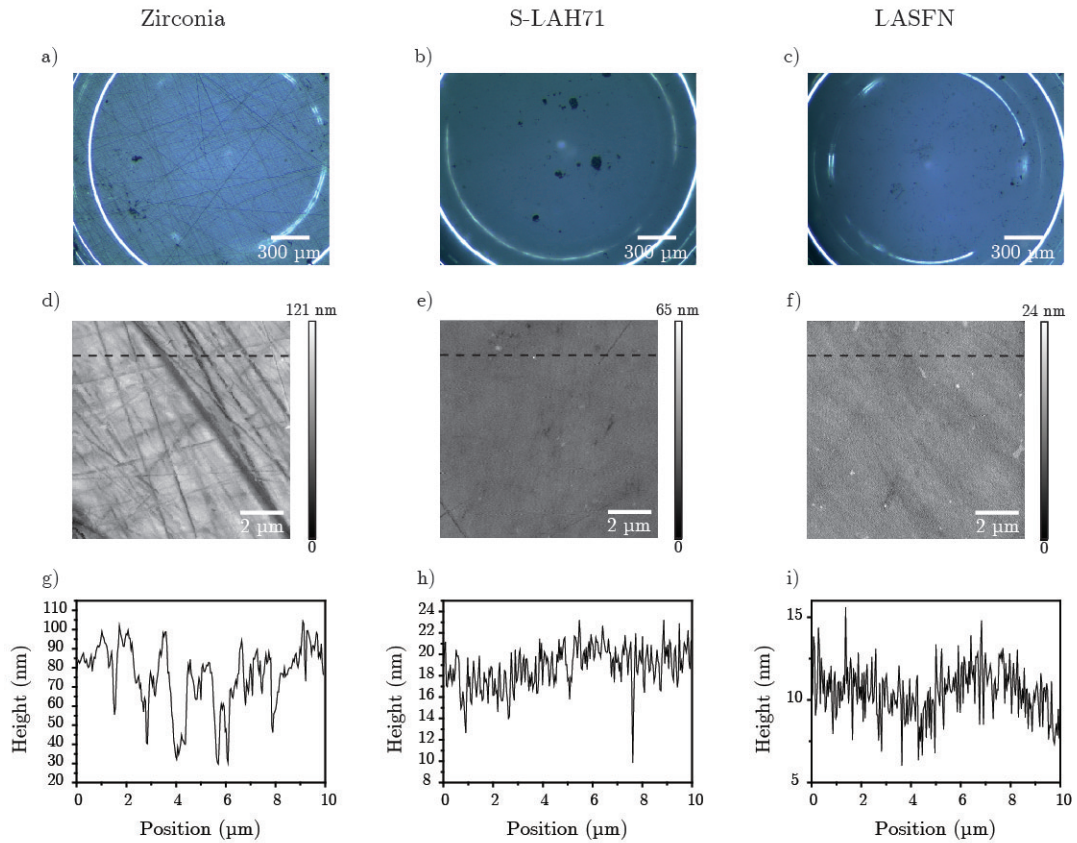


Figure 5.1: Surface characterization of the three solid immersion lenses (from left to right): Zirconia, S-LAH71 and LASFN. The upper row (a-c) shows optical images taken of the flat side of the SIL with 3.5 magnification. The Zirconia SIL exhibits a distinct line pattern. The AFM scans of a $10 \times 10 \mu\text{m}^2$ area are visible in the middle row (d-f) with the corresponding cross sections taken along the dashed line below (g-i). The LASFN SIL is showing the best surface quality and the worst surface quality is visible for the Zirconia SIL.

surface with fewer trenches. In the topography image (fig 5.1 e) the overall surface looks flat but on the top right and lower left thin scratches are present. They have a dept of 10 nm and a width of 80 nm, as can be seen in the cross section. The LASFN-35 topography image shows a flat surface with some small particles on top. The impression of a smooth surface is supported by the cross section, since it shows a nearly horizontal line.

Several of these $10 \times 10 \mu\text{m}^2$ AFM scans were performed and all of them were used to statistical analyze the surface. To determine the surface quality the root means square roughness R_{RMS} as well as the roughness average R_a was calculated. The resulting surface parameters are shown in table 5.2, together with the amount of scans used to determine the values. The calculations confirm the observations made by eye and during the AFM scans. The values of both roughness parameters decrease from

Table 5.2: Roughness parameters of the investigated solid immersion lenses.

Name	number of scans	R_a [nm]	R_{RMS} [nm]
Zirconia	16	14.08	18.34
S-LAH71	10	3.29	5.18
LASFN-35	10	1.99	2.69

Zirconia to S-LAH71 and LASFN-35 SIL. The Zirconia SIL shows surface parameters which are about a factor of 10 higher than for the S-LAH71 SIL. But the best surface quality exhibit the LASFN-35 SIL with $R_a = 1.99$ nm and $R_{RMS} = 2.69$ nm.

In the end, despite its high refractive index the Zirconia SIL was not suited for the planned measurements, due to its high surface roughness. The scratches are probably a result of the cutting and polishing procedure during manufacturing the SIL. The LASFN-35 SIL showed the best compromise with a high refractive index and the best surface properties among the tested lenses. Only a small surface roughness is present, possibly due to better polishing performance of the manufacturer.

5.1.2 Synchronous Scan

In chapter 4.1.1 the properties and advantages of the solid immersion lens were already introduced. The use of the SIL increases the amount of collected wave vectors but it also induces a new problem, the path difference as shown in figure 4.6. To perform a near-field experiment it is crucial to keep the tip centered in the focus of the laser, but this is not possible under these circumstances. A way to change the path difference between tip and focus is to introduce a factor that adjusts the tip movement accordingly. This factor is called synchronous scan gain and it is defined by the reciprocal value of the refractive index of the SIL. In case of the used LaSFN-35 SIL with $n_{SIL} = 2$ the synchronous scan gain should be 0.5.

To image the functionality of the synchronous scan a gold tip was centered in the focus and the gold luminescence of the tip was monitored during a scan. A representative image with a synchronous scan gain of 0.5 is shown in fig 5.2 a). The gold photoluminescence was recorded with a 633 nm long pass filter in the detection path and an acquisition time of 25 ms. An area of $1.5 \times 1.5 \mu\text{m}^2$ was scanned. Because the range of a typical near-field scan is equal or smaller than $1 \mu\text{m}$ the development of the intensity in this scan range should contain enough information on the effectiveness of the synchronous scan. The tip was centered in the lower left of the scan area, which is also the starting point of the scan. In 5.2 b) two cross sections are shown which were taken from the scan image. The black curve refers to the cross section

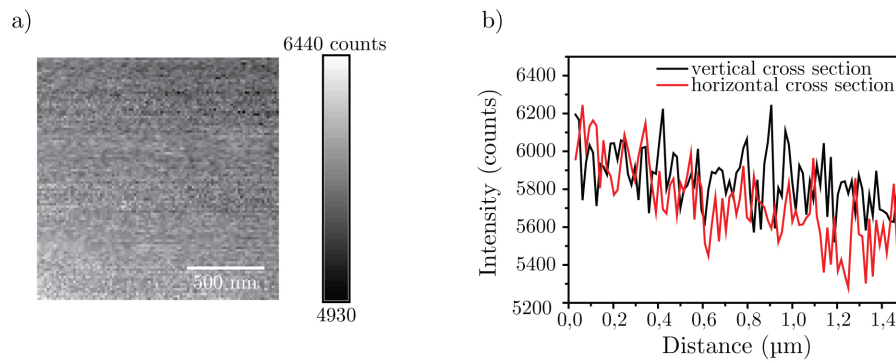


Figure 5.2: a) Synchronous scan of a gold tip centered in the laser focus. To detect the gold signal a 633 nm long pass filter and a acquisition time of 25 ms was used. The Gain setting to compensate for the path difference is 0.5. b) Cross sections along the first horizontal (red) and vertical (black) scan line to compare scanner performance in both directions.

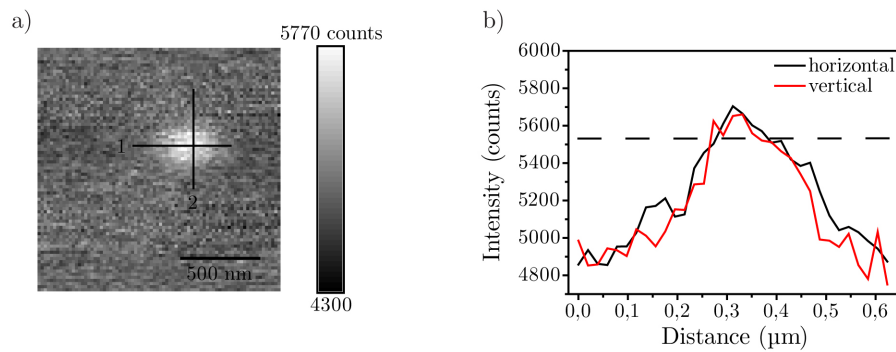


Figure 5.3: a) Photoluminescence image of a gold tip, acquired by scanning the focus over the fixed tip. To detect the gold signal only a 633 nm long pass filter and a acquisition time of 25 ms was used. b) Cross sections of the gold photoluminescence in horizontal (red) and vertical (black) direction. The dashed line in the graph represents 97% of the maximal signal intensity.

taken along the bottom horizontal line and the red curve is taken along the first column. For both directions the decrease of the signal intensity between beginning and end of the scan is about 3%. This indicates a stable synchronous scan and confirms that the gain value is suitable for tip-enhanced measurements. In addition, the similarity of both cross sections and the homogeneous intensity decrease in the scan image confirm an almost linear and uniform behavior of the sample scanners.

In image 5.3 a) the photoluminescence of a gold tip without synchronous scan is shown. The tip was centered in the middle of the scan area and kept at this position while the SIL was scanned. In this measurement the focus raster-scanned an area of $1.5 \times 1.5 \mu\text{m}^2$ using only a 633 nm long pass filter and an acquisition time of 25 ms.

The signal has a nearly circular shape and the intensity drops fast, indicating a sharp tip. The two cross sections taken horizontally and vertically across the signal are shown in 5.3 b). The graph contains a dashed horizontal line emphasizing a signal loss of 3% from the maximum intensity. This measurement indicates, that a signal decrease of the gold PL down to 97% corresponds with a spatial shift of the tip of 50 nm. This means during a $1.5 \times 1.5 \mu\text{m}^2$ scan with a synchronous scan gain of 0.5 the tip deviates approximately 50 nm from the initial centering. Since the focus has a size of 284 nm this value is acceptable and it should not severely influence the near-field enhancement.

The quality of the synchronous scan depends on several factors. At first the tip has to be centered exactly in the laser focus. Also the curvature of the SIL can effect the continuity of the synchronous scan, since it influences shape and movement of the focus. In other words, the performance of the synchronous scan is best if it is performed near the center of the SIL. If these conditions are met, the synchronous scan works well keeping the tip in the laser focus with only a small deviation.

5.1.3 Low Temperature Confocal Imaging

In this section exemplary PL measurements on CoMoCat nanotubes are presented acquired by conventional scanning confocal microscopy. One has to keep in mind that the scan movement of the sample holder does not equal the rastered area of the laser. Due to the path difference between the movement of the SIL and the focus all scans have to be recalibrated with the factor $1/n_{SIL}$. The maximal amplitude for the x,y piezo scanner at low temperatures is 20 μm , defining the maximal scan area of the sample. Taking the refractive index of the SIL of $n_{SIL} = 2$ into account, the area imaged during a scan can have a maximum size of 10 μm .

In figure 5.4 two photoluminescence scans are shown. In both images the laser raster-scanned an area of $10 \times 10 \mu\text{m}^2$. The images were recorded using a 632.8 nm HeNe laser, an acquisition time of 10 ms and a 810 nm long pass filter in front of the APD, to suppress scattered laser light. The left image demonstrates what happens if the SIL has a scratch on its surface. The nanotubes accumulate in the valleys which makes it hard to measure single tubes. The nanotubes in the scratch show photoluminescence and near the edges single spots indicate isolated nanotubes. But performing tip-enhanced measurements near the edge endangers the tip. Despite selecting the SIL with the best surface quality, irregularities during production or wrong handling can lead to scratches on the surface of the LASFN-35 SIL.

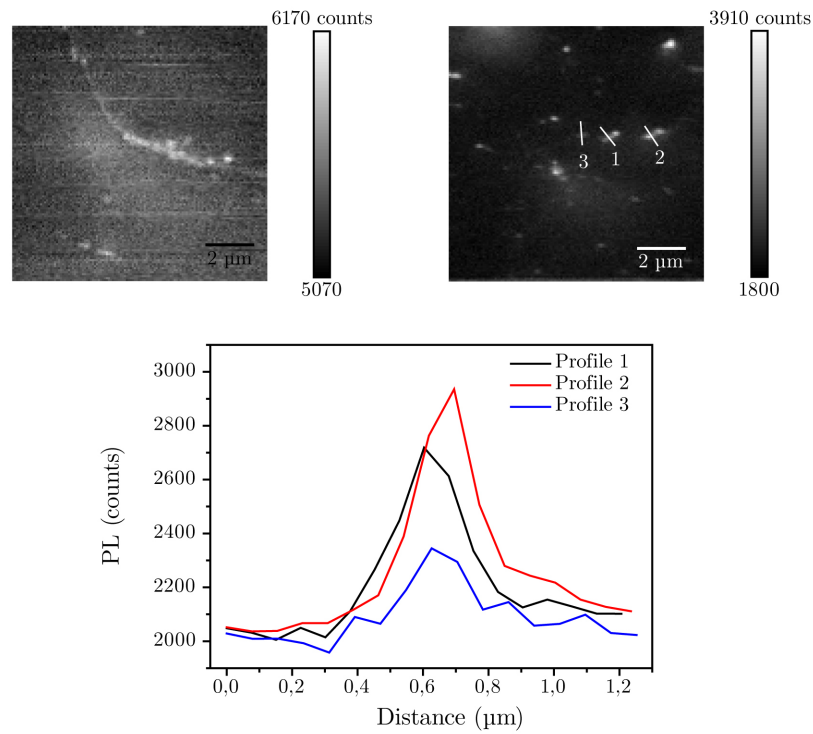


Figure 5.4: Photoluminescence scan of CoMoCat nanotubes deposited on the SIL at low temperatures. These two scans show CoMoCat on two different LASFN-35 SILs. Both images have a scan range of $10 \times 10 \mu\text{m}^2$ and were acquired by using a 810 nm long pass filter and with an acquisition time of 10 ms. The three cross sections taken on the right scan are plotted in the graph below.

The right scan in figure 5.4 shows elongated structures with varying photoluminescence intensity. Since the used 810 nm long pass filter only selects for the nanotube photoluminescence, it can be assumed that the observed signals originate from carbon nanotubes. They are evenly distributed over the substrate surface, showing different signal intensity. Spots with the lowest signal intensity are considered single tubes and it is expected that bundles appear brighter. The three cross sections marked in the PL scan are presented in the graph below. They are taken from structures with different brightness, assuming the weakest emitter is a single tube. In this case profile 3 shows the peak with the lowest intensity. It is half as bright as the peaks in profile 2 and 3. This leads to the conclusion that both profiles with higher intensity contain bundles of at least two tubes. The FWHM of several profiles, taken perpendicular to the nanotube axis were measured and a mean value of 257 nm with a standard deviation of 22 nm was calculated. Neglecting the size of the CNT perpendicular to the tube axis due to their small diameter, one can derive a spot size of 257 nm for the laser focus on the SIL surface. Taking into account the standard deviation, this value lies within the range of the theoretically calculated

spot size of the focus of 284 nm. This value was calculated for a 633 nm laser with a 0.68 NA and taking the refractive index of the SIL $n_{SIL}=2$ into account. The theoretically calculated focus size for the same microscope but without the SIL would be 567.8 nm. Therefore, the SIL further improves resolution due to its high refractive index.

Furthermore, in the middle of the scan area the background gets brighter. This can be observed when the SIL is completely centered in the laser focus. In this region probably back reflection takes place inside the SIL, leading to an enhanced radiation at this point. Whether the SIL is centered can also be observed with the webcam.

In this section, the SIL was characterized to determine whether its optical performance and surface properties are sufficient for near-field measurements. The LASFN-35 SIL turned out to be the best candidate for near-field measurements combining a high refractive index with a smooth surface. The high reflective index of the SIL leads to an improvements of the resolution by a factor $n_{SIL} = 2$. The low surface roughness of $R_a = 1.99$ nm enables scanning the gold tip without damaging it and should not influence the detection of nanosized structures on the surface. The synchronous scan was tested and a suitable synchronous scan gain value was found to compensate for the path difference between tip and focus movement. Overall the SIL proved to be suitable for future near-field measurements.

5.2 Characterization of the Low Temperature Atomic Force Microscope

The second important part of the microscope system is the low temperature tuning fork AFM. Upon excitation, the resonance frequency and the resulting amplitude and phase of the tuning fork oscillation is very sensitive to external forces acting on the prongs of the tuning fork. Tuning fork based AFM, in which the tip is attached to one of the prongs of the tuning fork is, therefore, capable of detecting very small forces down to few pN [120]. But this responsiveness to smallest changes makes it extremely receptive to variations in its environment as well as to its handling. To investigate the stability of the AFM at low temperatures, several measurements were performed and analyzed. At first the capabilities of the Q control and its influence on the resonance is reviewed. The functionality of this software feature is described in chapter 4.1.2. Q control is able to influence the Q factor by adding a second oscillation with appropriate phase shift and amplitude to the resonance frequency. Afterwards, the stability of the tip-sample distance control loop is examined by point and lateral measurements on a clean SIL. In the end, the overall performance is studied by low temperature topography scans of SWCNT.

5.2.1 Resonance Stability

Low temperatures make the tuning fork more stiff and lead to an increased Q factor of the resonance curve, of the tuning fork-tip system. Furthermore, a shift in the resonance peak can be observed. This behavior is visible in figure 5.5, where three resonance curves of the same tip-tuning fork system at room and low temperature (77 K) and for different gas pressures are shown. The black resonance curve was acquired at room temperature under atmospheric conditions. The blue resonance curve was also measured at room temperature but in the microscope stick filled with low pressured He gas. The resonance shift between both is about 19 Hz and the Q factor only slightly increases. The difference to the third curve is more obvious, here the tuning fork oscillation amplitude is higher and more narrow. This curve was recorded at 77 K under low helium gas pressure. In this case the Q factor is increased by 63%. In the course of this work an increase in Q from 20% up to 70% at 77 K could be observed. This behavior is different for every tuning fork-tip system and the weight and length of the tip as well as the soldering of the tuning fork have a noticeable influence.

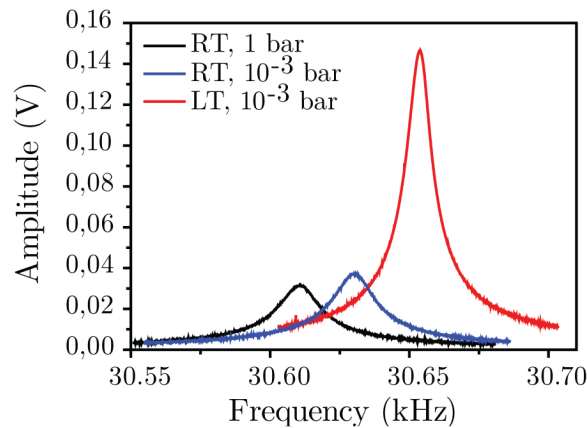


Figure 5.5: Resonance curves of the same tip-tuning fork system in different environments. The resonance curves were acquired under atmospheric conditions at room temperature (black), under low pressurized He gas at room temperature (blue) and under low pressurized He gas at 77 K (red). The cooling has the biggest effect on the resonance curve and an increase in Q from 1200 to 2000 is observed.

In figure 5.6 two graphs are presented, containing resonance curves for different Q control parameters at 77 K. The graph 5.6 a) shows three normalized resonance curves, one without Q control and two with active Q control and different phase shifts. The curve without Q control is shown in black and has a Q factor of about 18000. This value is too high to perform a stable tuning fork AFM measurement. The decay time of the oscillation is slow and leads to a delay in feedback response. To enable a more stable feedback the Q factor has to be reduced by using Q control. The red curve shows the resonance with active Q control and a phase shift of 180° . Due the influence of Q control the damping is increased, which leads to a drop in the Q factor to 13000. Compared to the case without Q control the Q factor has improved by 28%. Active reduction of the damping can also be achieved by applying Q control and it results in an even higher Q factor. By using a phase shift of 0° a Q factor of 24000 can be reached. The corresponding curve is shown in 5.6 a) in blue. This resonance curve is most narrow and additionally shows strong oscillations in the low amplitude region. These oscillations occur due to the decreased damping and the resulting increased decay time of the oscillation. In this case, the decay time reaches the timescale of frequency sweep of 10 ms used to record the amplitude spectrum shown in 5.6 a). The difference in phase shift between the two Q control influenced curves is 180° . These both phase shifts represent the highest and lowest damping, respectively and, therefore, result in highest and lowest Q factor for this system. This connection was shown in chapter 4.1.2 where the Q control for tuning fork based AFM was discussed.

For the curves in 5.6 a) a constant Q control gain of 0.995 was used, while the phase was varied. In graph 5.6 b) the gain was varied, while the phase was fixed at 180° leading to maximum damping. The resonance without active Q control and an excitation amplitude of 5 mV is shown as black curve. It exhibits a Q factor of 11530. The other three curves were recorded with the following gain values: 0.995 (red), 0.996 (blue) and 0.997 (purple), and with a constant excitation amplitude of 300 mV. With increasing gain a decrease in Q factor occurs. In this case the values drop from 7719 over 7118 to 6427. At the same time a drop in amplitude is visible. A drop in amplitude corresponds to a decrease in the signal to noise ratio, however. Therefore, a compromise between Q factor and signal to noise ratio has to be chosen. Of course an increase in excitation amplitude can improve the signal to noise ratio but it would also lower the sensitivity of the tuning fork.

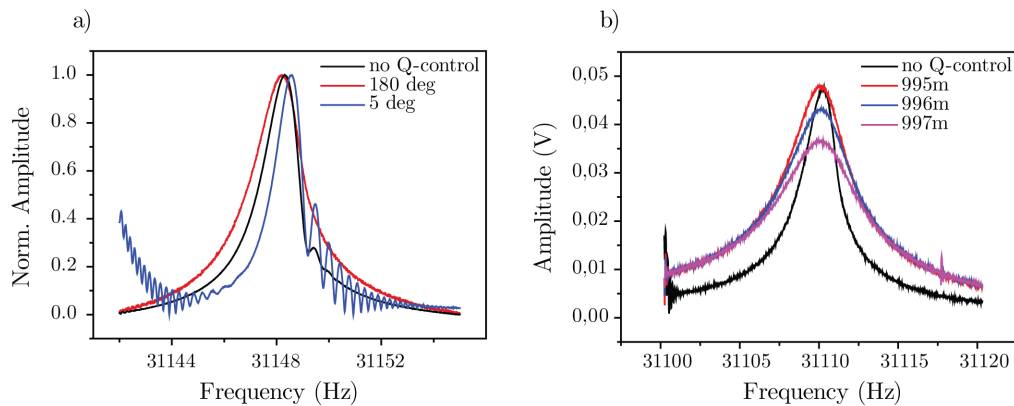


Figure 5.6: Resonance curves with different Q control damping at 77 K. a) Resonance curves with different phase shift settings used in the Q control. The Q factor without Q control is 18395 (black), the curve was recorded with an excitation amplitude of 5 mV and a resonance frequency of 31.1557 kHz. The highest damping is observed with a phase shift of 180° and a gain of 0.995 resulting in a Q factor of 13171 (red). The highest Q factor is 24390 (blue) with a phase shift of 0° and 0.995 gain. b) Resonance curves with different gain settings. The curve without active Q control (black) has a Q factor of 11530 and was recorded with an excitation amplitude of 5 mV. The other three curves were measured with active Q control, a constant phase shift of 180° and an excitation amplitude of 300 mV. The gain was varied between 0.995 (red), 0.996 (blue) and 0.997 (purple).

In conclusion, the Q factor is sensitive to many influences, for example the size of the gold wire tip, the amount of glue used and the soldering of the tuning fork. At low temperatures the Q factor typically is around 20000, too high for efficient tuning fork detection. Therefore, the software feature Q control and its influence on the tuning fork amplitude spectrum was tested. The variation of the phase and the gain settings have a significant influence on the resonance profile. By optimizing these parameters the Q factor could be lowered by about 50% at best. This allowed for

sensitive tuning fork based AFM measurements, although at limited scan speeds. Empirical it can be said, that the better the Q factor of the uninfluenced curve the higher the effect of the Q control. Also the effectiveness of the Q control depends for example on the soldering of the tuning fork and the connection quality to dither and tuning fork.

5.2.2 Feedback Stability

The stability of the AFM measurements is extremely sensitive to changes. Imperfections during soldering, like cold solder joints or loss of contact during cooling due to different thermal expansion of the components can occur. In the first hours after cooling the formation of nitrogen gas bubbles along the microscope tube, in the liquid coolant, can be observed as spikes in the tuning fork amplitude. If external influences can be excluded, also a broad tip or a contaminated sample can introduce disturbances.

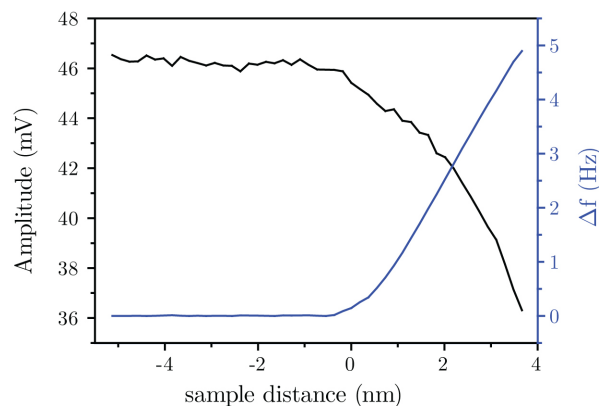


Figure 5.7: Dependence of amplitude and frequency shift as a function of tip-sample distance. The tip was landed on the bare SiL surface with a resonance frequency of 31.35 kHz, an excitation amplitude of 600 mV with active Q control and a Q factor of 7800. The tip-sample distance is calculated relative to the setpoint used for scanning.

Figure 5.7 presents the dependence of amplitude and frequency shift of the oscillation, on the distance between tip-tuning fork system and SiL surface. The distance between tip and sample is calculated relative to the setpoint. For measurements normally a setpoint between 100 and 200 mHz frequency shift was used, which is already high enough to be detected but not too high to risk damage of the gold tip. A change in frequency and amplitude is visible approximately 0.5 nm before the relative tip-sample distance is zero. At this distance the tuning fork already interacts with weak, far ranged forces. By further approaching the amplitude drops from

46 mV to 36 mV and the frequency is increasing. The relative change in amplitude of 10 mV is much larger than the relative frequency shift of 5 Hz. To compare the sensitivity of both, the signal to noise ratio has to be considered as well. The approach curve of the frequency shift appears to be much smoother than the amplitude curve. Therefore, the tip-sample distance control by detection of the frequency shift might give the better results.

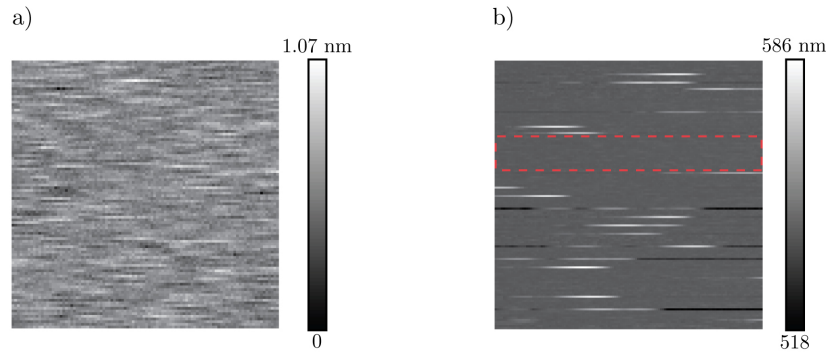


Figure 5.8: Two AFM point measurements showing two different situations. a) Optimized measurement without disturbances: The scan took 3 min and 20 s with 10 ms acquisition time per pixel. The resulting topography is uniform with $R_a = 0.14$ nm and $R_{RMS} = 0.18$ nm. b) Feedback problems with random spikes appearing: The scan took 5 min 27.7 s with 10 ms acquisition time per pixel. The resulting topography shows height differences up to 40 nm. Inside the marked area no strong deviations are visible resulting in $R_a = 0.4$ nm compared to $R_a = 2.53$ nm for the whole scan area.

To evaluate the stability of the feedback, different tip scans were performed. At first, a point measurement was carried out with closed feedback loop, to observe the tip-sample distance over time without scanning either tip or SIL. Two of these measurements are shown in figure 5.8. In fig 5.8 a) topography information over 100×100 pixels with a sample time of 10 ms per pixel were acquired. The whole measurement took 3 min and 20 s and the development of the topography over time is quite uniform. This impression is confirmed by the surface roughness values calculated for this measurement, the average roughness is 0.14 nm and the root mean square roughness is 0.18 nm. This measurement represents the optimized case with refined system and feedback parameters, which is reflected in the low roughness values. Problems in the system and the feedback loop could also often be observed, for example in the form of random deflections during a point measurement, as shown in image 5.8 b). Here, random and timely uncorrelated spikes in the topography can be detected, with heights of up to 40 nm. Nevertheless in between the system is quite stable, as can be seen in the area marked in red. For comparison the roughness values for the whole image and for the highlighted area were calculated. The complete image shows an average roughness of 2.53 nm, whereas the spike free

region exhibit a value of 0.4 nm. These spikes are random events, which cannot be attributed to a particular source. Either they vanish after a longer time period after cooling and, therefore, may be a result of thermalization effects inside the system, or in some cases only the replacement of wires, connectors or the dither piezo could resolve the problem, indicating an electrical problem.

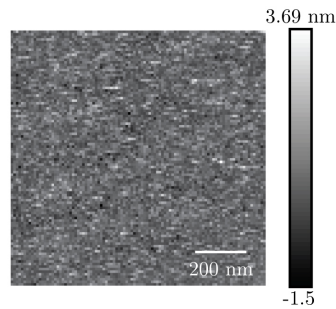


Figure 5.9: Raster-scan image of the gold tip over a flat and clean SIL surface. This scan was performed with 10 ms acquisition time per pixel and an overall scan speed of 250 nm/s in synchronous scan mode. The calculated surface roughness values are $R_a = 0.4$ nm and $R_{RMS} = 0.5$ nm.

After the point scan, the tip was raster-scanned to investigate the influence of the movement. A $1 \times 1 \mu\text{m}^2$ scan of a clean LASFN SIL is shown in figure 5.9. This scan was performed again with 10 ms acquisition time per pixel and an overall scan speed of 250 nm/s. The image was acquired using synchronous scan, which means tip and SIL are both moving. This measurement shows more distinct features compared to the point measurement in figure 5.8 a). Consequently, the surface roughness values with $R_a = 0.4$ nm and $R_{RMS} = 0.5$ nm are higher, than the values for the optimized point measurement. This indicates an influence of the lateral scanner movement on the system performance. These values are still small enough for the AFM to resolve nanometer length scales.

There is a difference between the surface roughness values determined for the LASFN SIL in chapter 5.1.1 ($R_a = 1.9$ nm, $R_{RMS} = 2.7$ nm) and the values calculated from this measurement. The measurement presented here, is taken with the tuning fork AFM at much slower scan speed and for a much smaller area. For the characterization of the SILs a different AFM was used, with a faster scan speed. Also the SILs in figure 5.1 showed a contamination of the surface, due to the AFM preparation procedure. The SIL investigated in figure 5.9 should be much cleaner.

5.2.3 Low Temperature Atomic Force Measurements

After optimizing the system parameters, in particular the Q control values, the PLL feedback gain and the setpoint, the scan and feedback stability of the low temperature AFM is excellent and the system is suitable to resolve nanometer length scales. To demonstrate the performance of the AFM, low temperature AFM measurements on carbon nanotubes were performed. In figure 5.10 two low temperature (77 K) AFM scans of CoMoCat nanotubes are shown. The measurements were performed with different gold tips and several month apart.

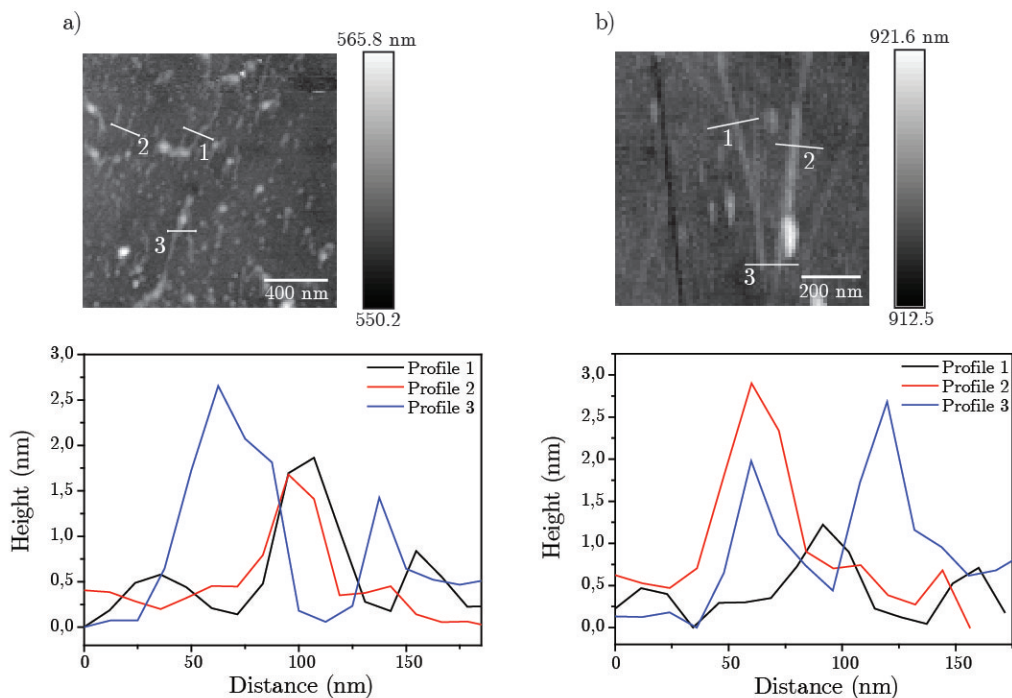


Figure 5.10: Low temperature AFM scans performed with a gold tip on CoMoCat nanotubes on a LASFN SIL. For every scan three cross sections were taken, with their profile presented below. a) Scan with an area of $1.6 * 1.6 \mu\text{m}^2$ with a high density of nanotubes and surface contaminations. The profiles show nanotubes with heights between 1 nm and 2.5 nm and a FWHM ranging from 17 nm to 46 nm. b) Scan with a size of $850 * 850 \text{ nm}^2$, showing few straight nanotubes. The profiles reveal nanotubes with heights between 1 nm and 2.5 nm and a FWHM ranging from 22 to 32 nm.

In figure 5.10 a) an overview of the sample topography is obtained with a range of $1.6 * 1.6 \mu\text{m}^2$. The scan reveals the characteristic 1D features of several nanotubes and some point-like contaminations, probably residual detergent. Three cross sections were taken at different positions across four nanotubes and the resulting profiles are presented below the scan. The most prominent feature is visible in profile three with

a height of 2.7 nm, which indicates either a bundle of nanotubes or a single nanotube covered with surfactant. In the same curve a second feature is present with about 0.7 nm, which is close to the nanotube diameter of 0.8 nm and is thus attributable to a single nanotube. The tip size can be approximated by the FWHM of this cross section due to the small CNT diameter, which can be neglected. The FWHM of the cross section taken perpendicular to the nanotube is 17 nm, which is in good agreement with the 20 nm diameter of the tip, as measured by electron microscopy. The height of the features in profile one and two is about 1.5 nm. The second scan image in figure 5.10 b) shows a smaller area of $850 * 850 \text{ nm}^2$ with fewer nanotubes. The cross sections again result in profiles with different height and width. The largest feature can be seen in profile three with an height of 2.5 nm and a FWHM of 32 nm. In profile one a single nanotube is visible characterized by a height of 0.7 nm and a FWHM of 22 nm. The other two features in profile two have a size of about 2 nm and are either bundles of two or single nanotubes wrapped in surfactant.

In summary, by optimizing the scanning parameters of the tuning fork AFM a good image quality with a high detection sensitivity and a height resolution down to 0.7 nm is achieved. The low temperature AFM is able to clearly resolve single carbon nanotubes. Therefore, if configured right the system has a good low temperature AFM performance suitable for tip-enhanced near-field measurements.

5.3 Low Temperature Tip-enhanced Near-field Measurements

In the previous sections, the performance of low temperature AFM and the characteristics of the SIL were discussed. It has been shown that by optimizing important parameters like the Q control values, the PLL feedback gains and the setpoint, the low temperature tuning fork AFM is able to resolve structures below one nanometer. Additionally, the synchronous scan was evaluated, to find the best settings to keep the tip in the laser focus. The final step is to combine AFM and confocal imaging, by centering the gold tip in the laser focus to gain near-field images.

In this section the last steps for the preparation of tip-enhanced near-field optical microscopy measurements are described. This includes the development of the tip centering procedure and the setup of a radial laser mode. And finally, the first low temperature tip-enhanced near-field measurements are presented.

5.3.1 Tip Centering

Centering the tip in the laser focus is a crucial step to gain tip-enhanced images. But this procedure turned out to be quite challenging, since the architecture of the system does not allow to look inside the microscope, when it is cooled down. Already finding and approaching the tip took quite long and often resulted in damaged tips.

To be able to observe the tip at low temperatures, an additional illumination channel was added to the setup. An uncoated fiber is guided through an empty epoxy sealed feedthrough into the microscope and fixed below tip and SIL at the sample holder. This fiber is positioned to illuminate the tip from below and to cast the shadow of the tip on the SIL surface, where it can be imaged by the integrated webcam. This addition allows to find, approach and center the tip in short time. The advantage is that the tip can already be seen when it is far away from the surface and because of that, damaging of the tip can be prevented.

For a better understanding figure 5.11 gives an overview of the two possible illumination directions and the corresponding webcam images. The scheme in fig 5.11 a) describes the standard beam path of the confocal microscope, where the laser is focused by an objective on the flat surface of the SIL. The resulting focus can be imaged by the webcam as seen in the image in the middle. This picture shows the whole field of view of the webcam. For a better view of the focus the marked area is magnified and presented next to it. This magnified image shows the focu-

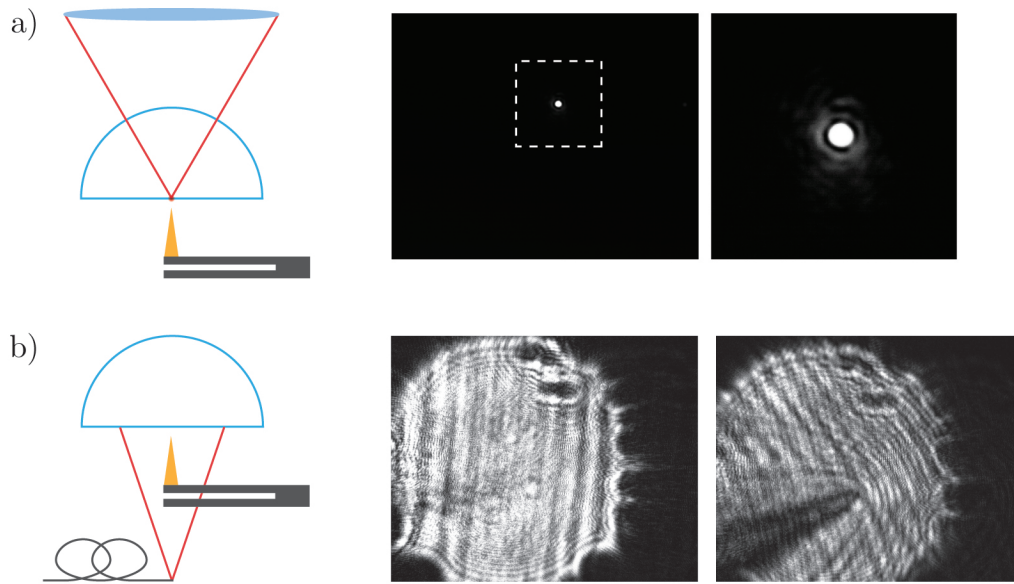


Figure 5.11: Schemes of the two possible illumination channels and their corresponding webcam images. a) Standard confocal laser illumination with the laser focused on the SIL. The field of view in the webcam is shown on the right next to it. The marked area is magnified and shows the characteristic airy pattern of a focused laser beam. b) New back illumination channel, introduced by adding a fiber. The corresponding webcam image with and without a tip in the field of view is presented to the right of the scheme.

sed laser beam and its characteristic airy pattern in more detail. The lower row in figure 5.11 presents the newly introduced illumination path via the fiber with a scheme on the left. The two webcam images next to it show the illuminated area: in the middle without a tip and on the right with a tip centered and in approximately $1\ \mu\text{m}$ distance to the SIL surface.

After roughly centering the tip in the laser focus by using the webcam, the tip is landed and the gold PL of the tip is monitored by an APD. The landed tip is centered with respect to the laser focus using the x,y piezos. The tip has reached the center of the laser focus when the photoluminescence signal is maximal. This procedure has to be done slowly and carefully to avoid damaging the tip. In figure 5.12 the development of the gold luminescence during a point measurement with simultaneous tip centering is visible. To highlight the intensity change during the tip centering, a cross section was taken along the black line. The corresponding graph is shown to the right. In the beginning the intensity is low and no signal is visible. At one point, after approximately 7 lines, the tip comes near the focus and an intensity increase can be seen. This signal is increased using the x,y piezos until the maximum is reached. In line 36 the tip is retracted and landed again. The intensity drops to the

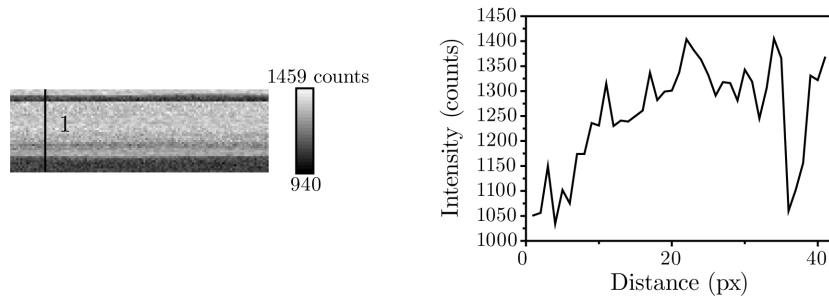


Figure 5.12: Evolution of the gold PL intensity, while centering the tip in the laser focus. Left: Photoluminescence intensity of a point measurement while adjusting the tip position to maximize the gold PL signal. The scan has a size of $42 * 128$ pixel with a line frequency of 0.391 Hz. Right: A cross section was taken along the line to illustrate the intensity development over time. The initial slow increase of the PL intensity is achieved by centering the tip with respect to the laser focus using the x, y piezos. At about pixel 37, the tip is retracted by about $1.2 \mu\text{m}$ and afterwards landed again.

same level as in the beginning of the scan suggesting a sharp tip. When a damaged tip is centered, it can still exhibit photoluminescence far away from the surface, due to its size. After landing the tip again the signal reaches the same value as before indicating a stable system. When the tip is centered, the synchronous scan can be started for tip-enhanced near-field measurements.

5.3.2 Tip-enhanced Near-field Measurements at Low Temperature

Initially, the measurements were performed using a linearly polarized laser mode, but no antenna-enhanced near-field signals could be observed. Efficient tip-enhancement requires a longitudinal field but a strongly focused linearly polarized laser mode has two weak lobes with a low longitudinal field component. Room temperature studies using a high NA immersion oil objective showed that it is possible to record near-field images with a linearly polarized laser mode, but in this type of measurements the near-field to far-field ratio is typically quite low.

Theoretical simulations have shown that radially polarized excitation is needed to gain a strong field enhancement at the end of a gold tip [121]. This higher order laser mode has a strong longitudinal component for on-axis illumination of the tip when focused. This favors the excitation of surface plasmons more compared to focused linearly polarized light. To create such radially polarized beam a mode converter,

either consisting of four $\lambda/2$ wave plates or a liquid crystal mode converter, can be used. However, both converters are too bulky to be inserted directly in the microscope or the optical head. Therefore, the generation of the radially polarized mode has to happen outside the system and the resulting beam has to be coupled into a fiber to enter the microscope. It should be noted that higher order beams are not easily coupled into the fiber and the output polarization strongly depends on the quality of the fiber and the forces applied to it [122]. Since the higher order laser beam has a larger diameter than the Gaussian beam of the same wavelength, a fiber with a larger mode field diameter has to be used [23, 122]. In this case the used fiber is a single mode fiber for 780 nm despite using an excitation wavelength of 633 nm. The output from this fiber is shown in figure 5.13. To test the polarization distribution within the mode a polarizer was placed in front of the fiber output with different orientations. The first image presents the radial mode without analyser and it shows a doughnut shaped laser mode. For the analyser orientations of 0° , 45° and 90° the resulting polarization states confirm that the mode is still radial after the fiber, despite some small asymmetries. To ensure that the polarization does not get altered by the laser line filter and the beamsplitter the laser mode was inspected after exiting the optical head. These images are presented in image 5.13, too. The output of the optical head looks still satisfying suggesting that the laser mode is stable even after it passed the optical elements.

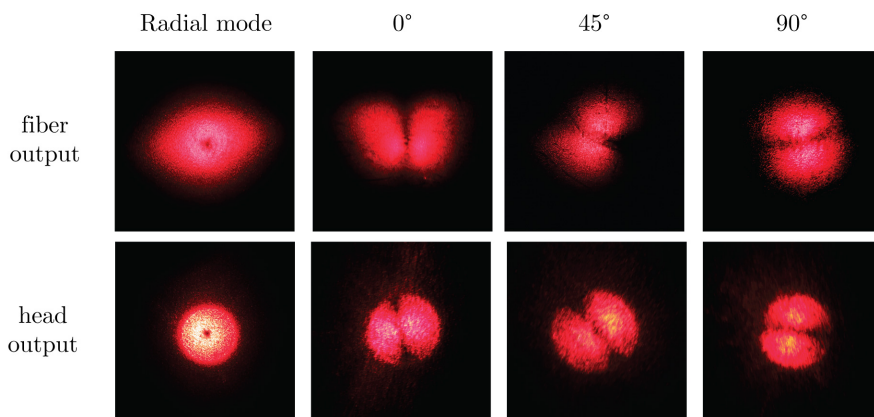


Figure 5.13: Image of the radially polarized laser mode after the fiber output (upper row) and after the head output (lower row). From left to right: Radially polarized mode. Polarization characteristics of the mode after an analyser oriented at 0° , 45° and 90° .

By using the radially polarized laser mode for excitation first tip-enhanced near-field measurements at 77 K could be performed. In the following section several near-field measurements at different positions are presented. In some cases two different photoluminescence images are shown. These were acquired at the same

time with the two detection channels containing different filters. The channel called photoluminescence 2 was equipped with a long pass filter 633 nm and was used to center the gold tip by observing the increase in intensity of the gold signal. Channel 1 was used to specifically detect the nanotube photoluminescence. Therefore, a long pass filter with 863 or 950 nm cut-off wavelength were implemented.

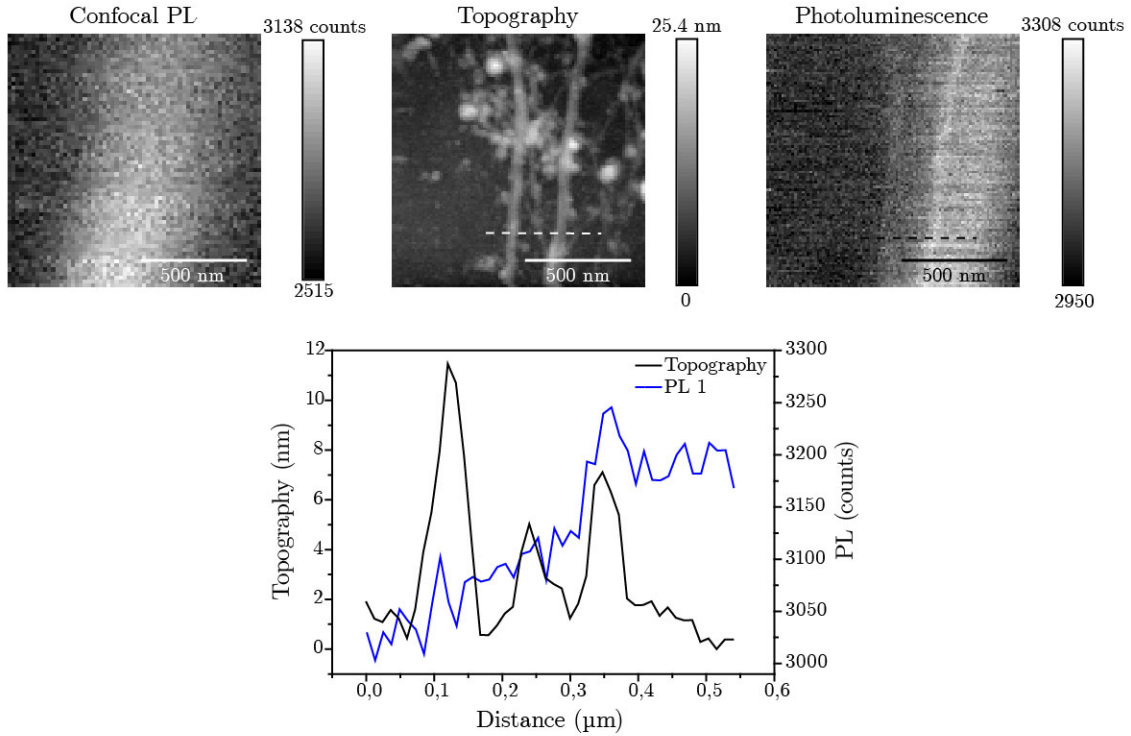


Figure 5.14: Tip-enhanced photoluminescence measurement of CoMoCat nanotubes on a LASFN SIL. An area of $1.2 \times 1.2 \mu\text{m}^2$ was raster-scanned. On the left the confocal photoluminescence is shown. Next to it the topography and the corresponding photoluminescence is visible. The cross sections of topography and photoluminescence are plotted in the graph below. Both photoluminescence measurements were performed with a 863 nm and a 633 nm long pass filter in the detection beam.

In figure 5.14 a tip-enhanced scan together with the corresponding confocal image is shown. In this case the photoluminescence was measured with a 863 nm long pass filter in front of the detector. The topography shows two 12 nm and 5 nm thick linear structures and several small, probably single nanotubes. The two bundles can also be seen in the tip-enhanced photoluminescence scan. Here, the confocal far-field background is still prominent. The confocal image and the confocal background in the tip-enhanced scan are comparable in shape and size but shifted slightly to the right. The presence of the background is also visible in the graph containing the plotted cross sections. It leads to a rise in the photoluminescence signal but on top of it two small peaks are present at the same position as the two biggest topography

features. The highest topography peak has a height of 12 nm and is certainly a thick bundle of CNTs. The other two topography features are smaller but no single nanotubes. They have a size of 5 nm and 4 nm, which is still much higher than the 0.8 nm expected for single carbon nanotubes. In conclusion, this scan shows an antenna-enhanced signal and by comparing topography and PL scan a localization of the signal is recognizable but the contrast between far-field and near-field is low.

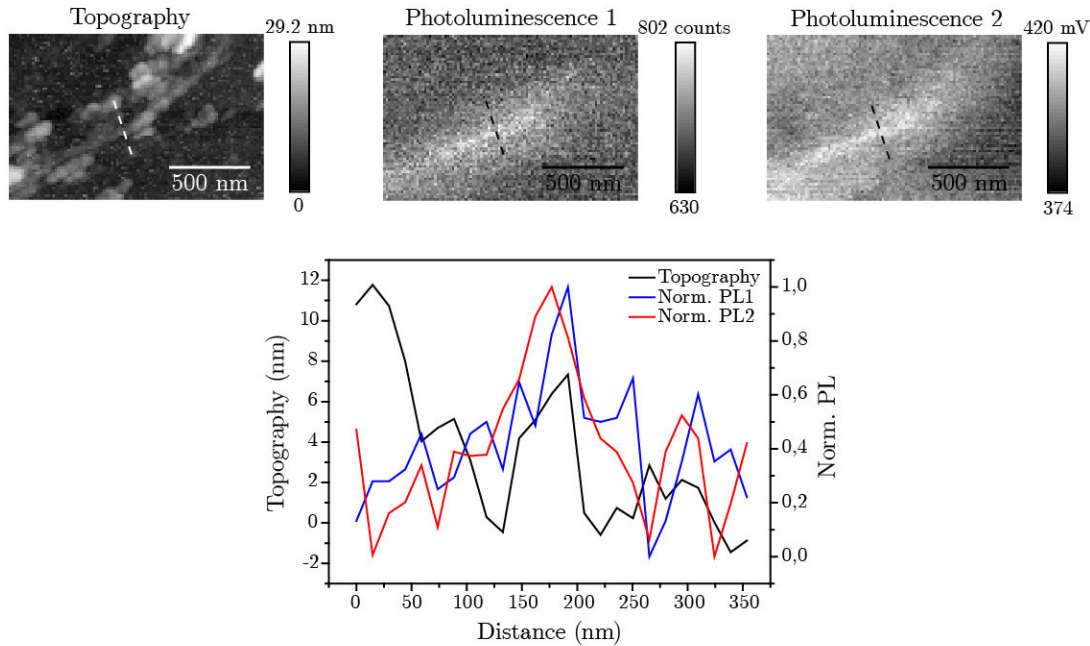


Figure 5.15: Tip-enhanced photoluminescence measurement of CoMoCat nanotubes on a LASFN SIL. An area of $1.4 \times 0.9 \mu\text{m}^2$ was raster-scanned. On the left, the topography image is presented. Next to it, the two different photoluminescence channels are shown. Photoluminescence 1 was acquired with a 950 nm and a 633 nm long pass filter and photoluminescence 2 with a 633 nm long pass filter in front of the detector. The overlay of all three cross sections is shown in the graph below. For a better comparison the photoluminescence intensity was normalized.

In figure 5.15 a tip-enhanced measurement on a different sample position is presented. The topography on the left shows a single nanotube surrounded by several particles. Both photoluminescence images represent the different detection channels mentioned above. For photoluminescence 2 only a 633 nm long pass filter was used, whereas for photoluminescence 1 additionally a 950 nm long pass filter was inserted into the detection beam path. Both images show comparable behavior with a visible near-field enhancement at the same position but not along the whole tube. Additionally, the far field background is present in both channels. The cross sections taken from all three scans at the same position of the nanotube are presented together in the graph below. The position of the nanotube (black line) overlaps nicely with the

intensity maximum of both photoluminescence channels. The width of the photoluminescence signal decreased down to 34 nm for photoluminescence 1 and to 64 nm for photoluminescence 2 for the best case. The width of the nanotube in the topography is 55 nm and, therefore, bigger than the photoluminescence signal in channel 1. It can be assumed that the nanotube is wrapped in surfactant which would lead to an increase in diameter. If this is the case, the near-field would be reduced due to the resulting dielectric shielding and increased tip-nanotube distance. In general, this measurement shows a field-enhancement in both photoluminescence channels with better contrast and localization than in figure 5.14.

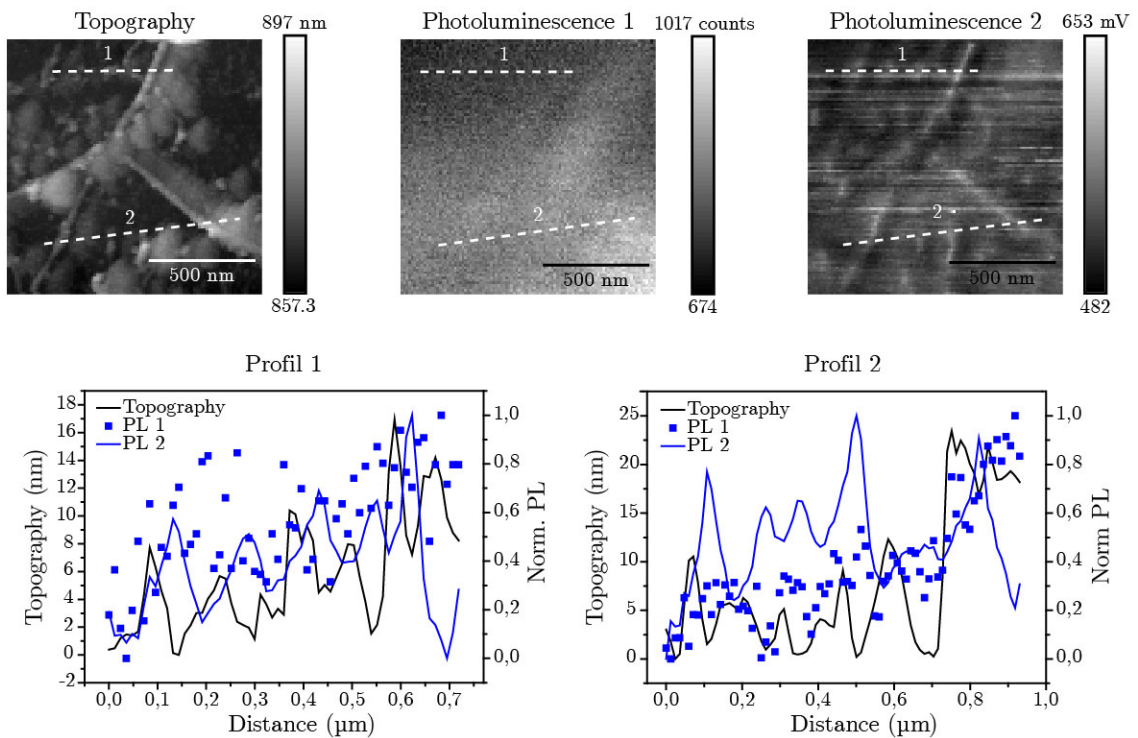


Figure 5.16: Tip-enhanced photoluminescence measurement of a CoMoCat nanotube on a LASFN SIL. A $1.2 \times 1.2 \mu\text{m}^2$ large region was raster-scanned. On the left the topography image is visible. Next to it the two different photoluminescence channels are shown. Photoluminescence 1 was acquired with a 950 nm and a 633 nm long pass filter and photoluminescence 2 with a 633 nm long pass filter in front of the detector. Two cross sections were taken at different positions and the resulting graphs are presented below.

In figure 5.16 the experimental results are different than in the scans before. The topography is much more crowded with lots of particles and different-sized nanotube bundles. The topography image shows artifacts, indicating a non-perfect tip shape. Additionally, the two photoluminescence channels differ substantially. Photoluminescence 1 is nearly identical with the confocal image, whereas in photoluminescence 2 a strong signal localization is visible. The pattern in this scan nicely

matches the topography. One explanation of why the influence of the antenna is only visible in one channel could be, that the Raman signal and not the photoluminescence is enhanced. The photoluminescence channel 2 represents all wavelengths above 633 nm, which also includes the Raman bands at 703 nm and 760 nm, respectively, in contrast in channel 1 a 950 nm long pass filter is used, which definitely suppresses the Raman signal. Another observation is that the background of the photoluminescence channel 2 is inhomogeneous. This behavior probably originates from the gold luminescence of the tip, which is sensitive to even small changes in the tip position. If the tip surface is rough, a fluctuation in the gold signal can occur, too. To gain a better insight the cross sections, which were taken at two different positions in the scan region, were evaluated. Both graphs contain the topography in comparison with both PL channels. For the intensity of photoluminescence 1 a scattered representations is used since it does not show any distinct features. As already indicated by the scan image, the topography profile reveals structures up to 25 nm in height. The comparison between topography and the PL 2 cross section indicates a shift, which is not recognizable in the scan image. All features of the photoluminescence are shifted by approximately 40 nm compared to the topography. This indicates an irregular, non-conical tip shape. As a result, different features of the tip probe the sample topography and the optical response. Moreover, irregular tip shapes can even lead to spectrally dependent enhancement and image contrast [123]. The signal in the detection channel 2 is enhanced by 18% and the smallest FWHM obtained from the profile is 36 nm.

All three measurements presented in this chapter confirm that the tip interacts with the optical signal resulting in localization and enhancement of the fields. The tip-enhanced signal always could be correlated with the corresponding topography. Even in image 5.16 a correspondence is obvious despite the shift between both channels. All images still exhibit a substantial confocal far-field background due to a weak enhancement and, therefore, low contrast. Up to now, the image quality and especially the contrast is not comparable to room temperature measurements. A possible explanation for the weak enhancement is the deposition of a thin layer on the tip upon cooling. Despite evacuating the chamber and using exchange gas with a purity grade of 5, it is very well possible to have contaminants in the atmosphere of the measurement chamber. These tend to absorb on cold surfaces, especially metals since they have a high heat conductivity and cool down fast. This could lead to the generation of a thin layer on both the gold tip and the sample surface. Since the field enhancement strongly depends on the exponentially decreasing near-field, an increase in tip-sample distance due to this layer would strongly reduce the enhancement. Also this layer would lead to dielectric screening resulting in a further decrease in

the enhancement [124]. This model would explain why the enhancement is low and why very often no field-enhancement is observed even though the tip is centered. It would also explain the rather low spatial resolution obtained in the near-field images around 50 nm. To avoid this problem, a new approach during cooling is tested. The heater included in the sample stack is used to heat the sample including the tip. The heater is switched on while the microscope is inserted in the bath cryostat to keep sample and tip at a higher temperature. After some time everything except this small heated area has cooled down and existing contaminants should already be absorbed by the cold regions. This approach was tested few times and appears to increase the probability for successful low temperature TEMOM experiments. But to fully evaluate the efficiency of this procedure, more measurements are needed.

6 Summary and Outlook

The aim of this work was to implement and characterize a new microscope design for cryogenic tip-enhanced near-field optical microscopy. The system presented, is able to acquire tip-enhanced photoluminescence images of individual single-walled carbon nanotubes, at 77 K and with a resolution down to 35 nm.

In the last 25 years, different designs of low temperature near-field microscopes were presented. They can be divided in three working principles: aperture-SNOM, scattering-SNOM and STM-based TERS. The first low temperature measurements were performed with an aperture-SNOM, but they suffered from low signal intensity and limited lateral resolutions above 50 nm. Scattering-SNOM is suitable for experiments in the IR regime and has been used on various sample materials. The latest development is the UHV STM-based TERS microscope. It enables sub-nanometer resolution and strong Raman enhancement up to 10^8 . This behavior originates from the gap plasmons, which are confined between the metallic tip and substrate. With this approach, single molecule experiments could be performed. However, this approach is limited to metallic substrates and samples with a small thickness. Importantly, it is not suitable for the observation of fluorescence, since the metal substrate would quench the signal.

The microscope implemented in this work is designed to detect the photoluminescence of samples and shows some unique features, compared to the systems presented before. It contains a solid immersion lens (SIL), as dielectric substrate to achieve collection angles larger than the critical angle θ_{crit} of the objective. This is of prime importance for the observation of the tip-enhanced signal, which is emitted primarily above θ_{crit} , corresponding to a numerical aperture $NA > 1 = n \sin(\theta_{crit})$. The introduction of the SIL, however, led to the problem of the path difference, which prevents the tip from staying in the laser focus during the scan. To compensate for this path difference, two independent scanner stacks were realized, controlled by the so called synchronous scan implemented in the software. The microscope uses a gold tip, acting as optical antenna, to enhance the signal in the near-field region. For controlling the tip-sample distance a tuning-fork based AFM was employed.

Before performing the tip-enhanced measurements, all parts of the microscope had to be thoroughly characterized and the scan parameters had to be optimized. Firstly, a suitable SIL had to be selected, combining a high refractive index and low surface roughness. Three SILs were examined by AFM, to determine their surface roughness. The Zirconia SIL had the highest refractive index ($n=2.177$), but also the highest surface roughness, with a roughness average of $R_a=14$ nm. The S-LAH71 SIL exhibited the lowest refractive index ($n=1.85$) but an improved surface roughness ($R_a=3.29$ nm), compared to the Zirconia SIL. The LASFN-35 SIL had the best surface roughness properties ($R_a=1.99$ nm) and a high refractive index ($n=2.02$), and, therefore, was chosen for near-field measurements.

The second step was to test the synchronous scan and to optimize the parameters to keep the tip in focus during scanning. Due to the refractive index of the LASFN-35 SIL, the path difference of the focus movement is approximately half the range of the tip scan. A synchronous scan gain of 0.5 was found to be suitable for tip-enhanced measurements. With this value a shift in focus position of about 50 nm, for a scan range of 1.5 μm is observed. This shift is acceptable regarding a focus size of 284 nm.

The optimization of the tuning-fork AFM performance at low temperatures formed the next part of this thesis. At a temperature of 77 K the Q factor can grow by 20 to 70% as compared to room temperature, which leads to a delay in feedback response. The damping of the tuning fork oscillation can be influenced by using Q control, a feature implemented in the software of the SPM controller, which is based on the asynchronous excitation of the tuning fork. The aim is to reduce the Q factor, to improve the response time of the tuning fork detection. Two parameters have to be controlled in order to gain the best Q factor: the phase shift and the gain. The highest damping is observed, with a phase shift of 180° and the gain needs to be at least 0.99, to see a sufficient change in Q factor. If the gain is set too high, it will result in a decrease of the signal to noise ratio. For every new tip and new tuning fork a new gain has to be chosen in the range between 0.990 and 0.998, to obtain a small enough Q factor with a reasonable signal to noise ratio. After choosing the right Q control values, the phase-locked loop feedback parameters of the the force feedback have to be optimized in order to perform stable AFM measurements. To evaluate the stability of the AFM different measurements were performed, first on a clean substrate, and later on single walled carbon nanotubes. The reference measurement on the clean LASFN SIL revealed a stable and smooth topography, with a surface roughness value of 0.4 nm. This value is smaller than the surface roughness obtained for the LASFN SIL during characterization. This can be explained with the smaller scan area and the different AFM technique used to scan the image. With all scan

parameters optimized, single walled carbon nanotubes down to a diameter of 0.7 nm could be imaged.

After optimizing the system parameters of the synchronous scan, Q control and the feedback, the system proved to be suitable for measuring at low temperatures. To gain tip-enhanced near-field images, confocal imaging and AFM have to be combined. First, the tip has to be centered in the laser focus. This step is crucial, since only perfect centering results in a high field-enhancement. In the present setup the tip is not visible from the outside of the cryostat, however, centering without damaging the tip, thus, is quite challenging. In the course of this work, a new illumination channel was implemented to visualize the tip shadow on the SIL surface. This improved and sped up the tip centering process and the handling of the tip at low temperatures.

In the beginning, tip-enhanced near-field measurements were performed using a linearly polarized laser mode, but no antenna-enhanced signals could be observed. A mode converter was added to create a radially polarized laser mode. This mode has the advantage of having a strong longitudinal component for on-axis illumination of the tip, when focused. This results in a stronger excitation of surface plasmons and leads to a higher field enhancement at the tip. The radially polarized laser mode was coupled into the microscope by using a polarization maintaining fiber.

These improvements in the setup and the optimization of the system parameters lead to the first tip-enhanced near-field PL measurements performed at 77 K. Experiments at various sample positions are presented, showing a difference in image quality. The localization of the signal, due to the interaction with the tip, led to a resolution down to 35 nm. A field enhancement up to 18% could be observed. All images still exhibit a far-field background and weak contrast. A possible explanation for the weak enhancement is the deposition of a thin layer of contaminant on the tip and/or the sample, during cooling. An additional layer with a thickness of a few nanometers, would increase the tip sample distance, leading to substantially weaker near-field interactions. To avoid this deposition a new approach during cooling is tested. The heater, which is included in the sample stack, was used to heat the sample, including the surrounding tip until the other parts of the microscope inside the cryostat are cooled. This could result in the contaminations adsorbing onto the walls of the chamber and not the tip. This procedure appears to increase the probability of successful low temperature TEMOM experiments, but more measurements have to be performed to fully evaluate the efficiency of this approach.

In summary, this work presented and characterized a new low temperature tip-enhanced near-field microscope. The optimization of the measurement parameters

and the improvements in the setup resulted in the first low temperature tip-enhanced near-field measurements. The successful implementation of the microscope opens up the way for further investigations at low temperatures. The issue of the weak field enhancement and the heating approach have to be investigated further. In the future different sample materials can be measured using this microscope, to gain new insights into nanomaterial properties at low temperatures. By using liquid Helium as coolant the operation temperature of this microscope can be decreased even further down to 4 K. AFM measurement at 4 K have already been performed with this system, confirming the usability of the microscope at these temperatures.

7 Appendix A: Manual for Handling the Low Temperature Setup

This chapter acts as manual and describes all crucial steps needed to perform tip-enhance near-field measurements at low temperatures, including one section, which focuses on the important software properties and gives an overview on the user interface. Additionally, important error sources and measurement artifacts are discussed.

A.1 Structure and Parts of the Setup

In this section the main parts and the whole setup are shown and named. All electrical and optical connections, which are important for performing a measurement are described.

Figure A.1 shows the external beam path that is fixed on the optical table and is responsible for coupling the laser into the fiber. The laser can be switched by a flipable mirror between two fiber couplers. If the mirror is flipped into the beam path, the laser is deflected to the fiber coupler responsible for back illumination. This configuration is needed to find and center the tip via the internal webcam. If the mirror is removed, the laser passes a beam expansion and a liquid crystal mode converter and is coupled into the other available fiber coupler. This is the standard configuration for confocal or tip-enhanced imaging. The liquid crystal mode converter converts the laser polarization into a radial mode by applying a voltage. The two wires coming from the mode converter are labeled *Phase Comp.* and *Rad./Azim.* and have to be connected to *Output 1* and *Output 2* of the LC Driver. The LC Driver is controlled by a laptop via USB connection. To enter the voltage applied to the mode converter the *ARCOptix LC Driver* software is used and the following values have to be entered: *Rad./Azim.* = 8.8 V and *Phase Comp.* = 1.91 V. This results in a radially polarized laser mode, but only for a wavelength of 633 nm. If other wavelengths are used, the *Phase Comp.* value has to be adjusted. To do so, consult the manual of the *ARCOptix Polarization Converter*.

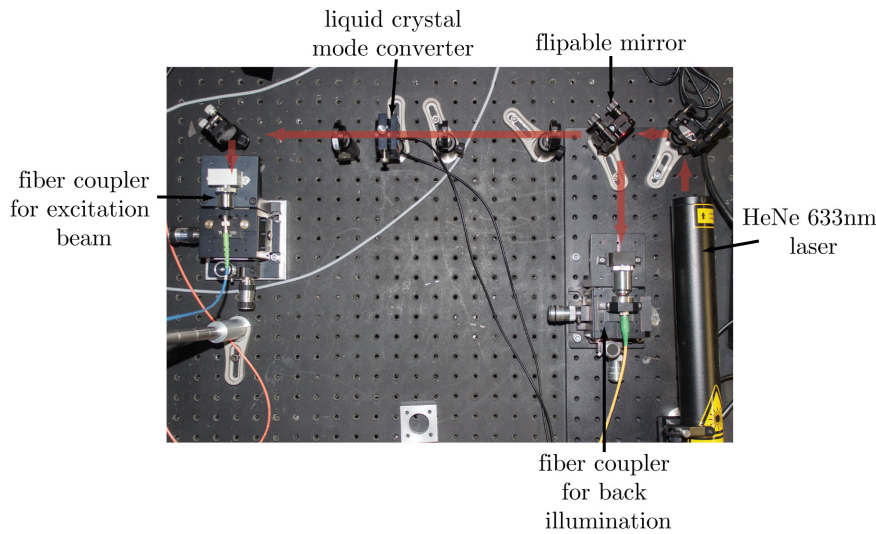


Figure A.1: The beam path on the optical table. It is responsible for fiber coupling the laser into the system. One can switch between standard laser excitation or back illumination of the sample by flipping the mirror. The mode converter converts the excitation beam into a radial laser mode.

The experimental section of this thesis contains a schematic overview (see 4.11) about all important connections of the system. For operation, the electronics looks like shown in the left image of figure A.2. All wire connections visible in this image are set and should not be changed. The breakout panel merges all signal cables coming from the controllers to six main cable bundles. These six cables have to be connected to the microscope stick as visible on the right in figure A.2 using the 12pin Fischer connectors. This figure shows the upper part of the microscope with the optical head and all important optical and electrical connections. All connections visible in this image need to be removed when the microscope is moved to the VÜK or inserted into the cryostat. Before starting the measurement it is important to reconnect everything as shown.

In the optical head different types of fiber couplers are present. Each is labeled by a sticker next to the port. The orange fibers are multimode fibers and responsible for sending the signal to the APDs. *Detection 1* is directly connected to the fiber coupled APD, which is fixed on the optical table. The second APD has no fiber port and the fiber coming from *Detection 2* is connected to a fiber coupler where the signal is coupled out and focused on the APD by a free horizontal beam path. The polarization maintaining fiber (blue) is connected to the *Excitation* port of the head. On the front of the head a switch is present that slides the pellicle beamsplitter in and out of the beam path. While the beamsplitter is in the beampath 3% of the signal is sent to the webcam for imaging. The webcam has to be connected to the

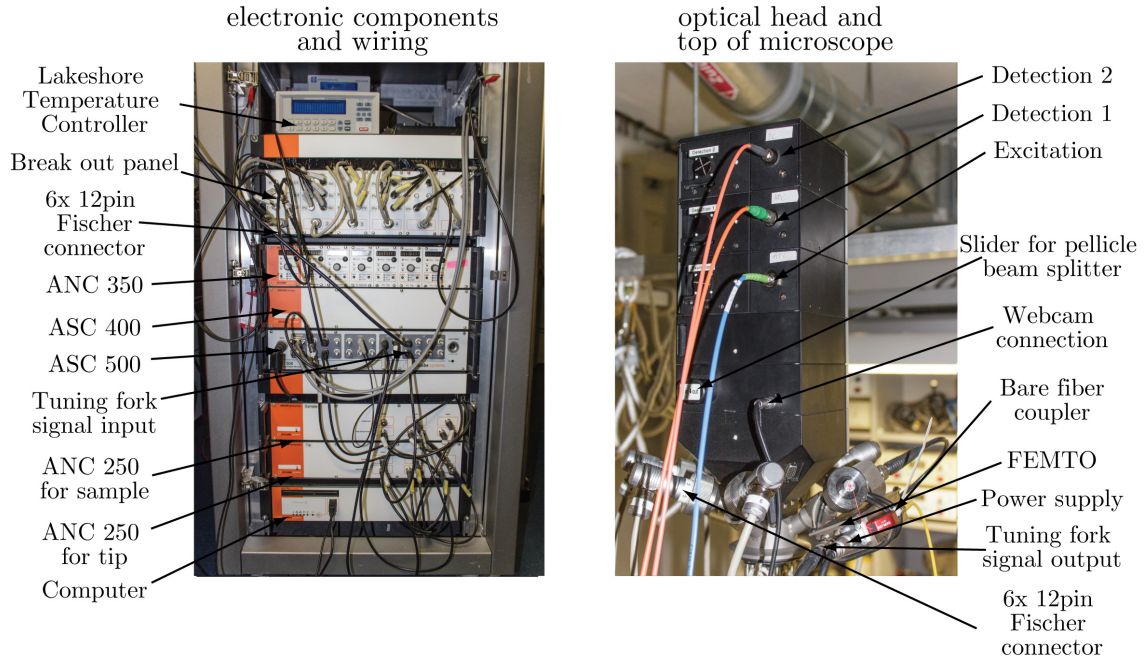


Figure A.2: Left: Electronics rack containing all controller and electronic connections. The wiring should not be changed. Right: Upper part of the microscope with the optical head. All electrical and optical connections are crucial for performing a measurement and should only be disconnected while the microscope is moved.

USB port of the computer. The microscope stick contains 6 ports for the 12pin Fischer connectors. They have to be attached following the numbers labeling jack and plug. In addition, the FEMTO is fixed on top of the microscope stick and he must not be removed and needs to be connected to the power supply. The tuning fork signal coming from the microscope is sent into the FEMTO by a short BNC cable, before the amplified signal is transmitted from the FEMTO to the *HF IN 1* connection of the ASC 500 by a BNC cable. On the side of the FEMTO a bare fiber coupler is fixed and connected with the fiber used for back illumination. Before moving, the FC/PC fiber patch cable has to be disconnected.

In figure A.3 the stacks for sample and tip movement are shown from behind. The stacks are plugged to the microscope and the electrical signal is distributed from the four 18pin connectors to the single components. The pin assignment is defined in A.3. Cables with a positive voltage are labeled red and ground wires are labeled black.

In figure A.3, on the left, the sample stack is shown. The left 18pin row of the sample stack contains the heater and temperature sensor connections. Below a single pin connects the head plate of the sample stack to the ground. The last three vertical pins are responsible for reading the position of the z positioner (Res Pz). For the

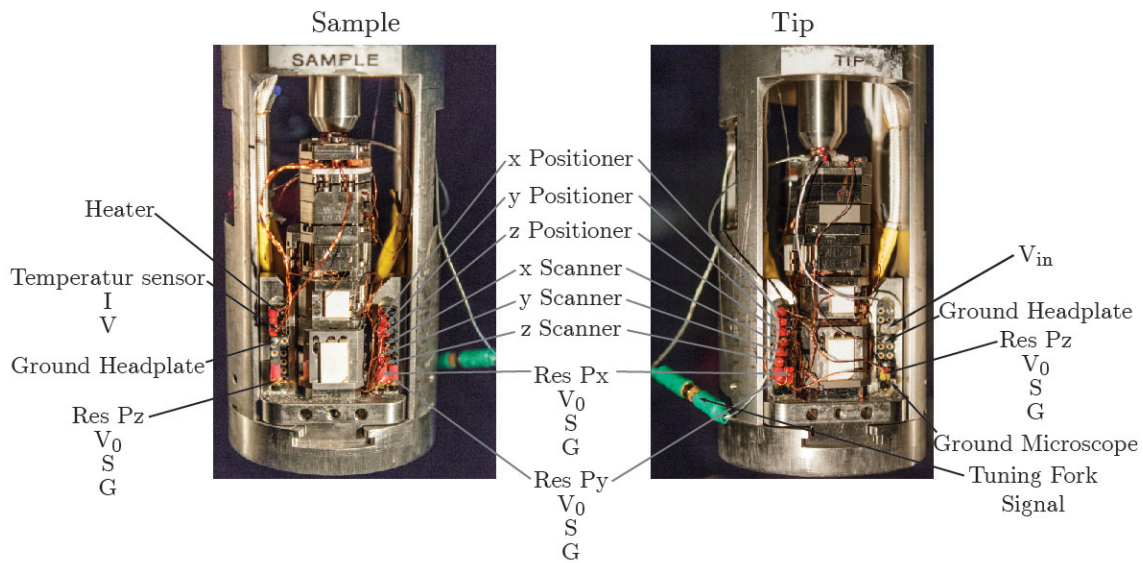


Figure A.3: Both measurement sliders, present at the bottom of the microscope stick, are shown from behind. Left: Sample stack Right: Tip stack. The pin assignment of the four 18 pin connectors is shown.

resistive position readout, a constant input voltage (V_0), the resulting sensor readout (S) and a ground connection (G) are present. In this pin row some free pins are available for additional connections. The right 18pin connector row of the sample stack is responsible for connecting all three piezo scanner and positioner and the position readout for x and y positioner.

On the right side of figure A.3 the tip stack is visible. The left pin row of the tip stack is identical to the right pin row of the sample stack. It connects to the scanners, positioners and the positioner readout. On the right side of the tip stack several empty pins are present. Further more, the excitation signal of the dither piezo is connected (V_{in}). The single wire below connects the head plate to the ground. The connection for the positioner readout of the z positioner can be found in the lower left.

A.2 General Points

- Always switch off all outputs in the software before removing cables or the stacks
- Keep the VÜK closed with a lid when not in use
- Vent the pump after it is disconnected from the system and has stopped moving
- Don't forget to change between room temperature and low temperature settings
- Flip the pellicle beamsplitter inside the optical head out of the beam path when imaging
- The connection of dither and tuning fork cables are fragile: avoid straining or twisting
- Switch off the halogen lamps next to the system, they interfere with the tuning fork oscillation
- Switch off all positioner outputs during scanning they interfere with the amplitude
- The objective is sensitive to dust flying into it if it is kept outside the VÜK
- While scanning the SIL without the tip, the tip should be retracted at least 20 steps to keep it safe

A.3 Software

In this section the main measurement software *Daisy* is described. If more detailed Information are needed the Main User Manual can be consulted.

The software controls the scanning controller ASC 400 and ASC 500 and the positioner controller ANC 350. To avoid interactions it is advised to switch on the hardware in the following sequence: ASC 500, ASC 400 and ANC 350 afterwards the two ANC250. At first the software for the ANC 350 is started, which can be found on the desktop (C:/Program Files/atto software/ANC 350_v1442/daisy). Afterwards the program for the ASC 500 is selected (C:/Program Files/atto software/Sync test 2/ASC 500 hs/Daisy). The program takes some time to synchronize and a green light in the lower right of the window indicates a successful connection. The profile *AFM2.ngp* contains the main control panels for performing a measurement. It

Table A.1: Settings for the output limit of different temperatures.

parameters	297 K	77 K	4 K
x/y max. voltage	3 V	6.39 V	7.5 V
x/y max. range	35 μm	20 μm	20 μm
z max. voltage	3 V	6.39 V	7.5 V
z max. range	3.5 μm	2 μm	2 μm

is opened by clicking on the open icon () after loading two green signal lights should be visible in the lower right. At last the program for the ASC 400 is selected (C:/Program Files/atto software/Sync test 2/ASC 400 hs2/Daisy) and the same profile is loaded.

In the end three windows should be open: One to control the positioner via the ACS 350 and two windows to control the scanning. The window named *Daisy Double Device Mod@ ASC400 SPM Controller* is only for monitoring and checking the tip movement. Here no parameter should or can be changed since it has no influence on the scan. All scan parameters are controlled by the ASC 500 and, therefore, the *Daisy Double Device Mod@ ASC 50mm SPM Controller* window is the main working interface. Both controller work in a master/slave configuration and the program window for the ASC 400 is only required if the scanning signal is not transferred correctly and needs to be adjusted by hand.

Before proceeding with the measurements and activating the *Output*, some parameters have to be changed in the program:

- Insert the correct *Output Limits* (see table A.1) and set the lever to the right temperature range
- In the *Output Limits* also the Scanner Adjustment Speed should be lowered to 1 $\mu\text{m/s}$ or 500 nm/s
- In the *Line View* tab a sample time of 10 ms should be entered
- Got to Settings→Experiment Preferences→Counter→Exposure Time: 10 ms

Depending on the environment different output limits have to be used. They can be changed by clicking on the corresponding button on the upper left. Table A.1 summarizes the required settings for different temperatures.

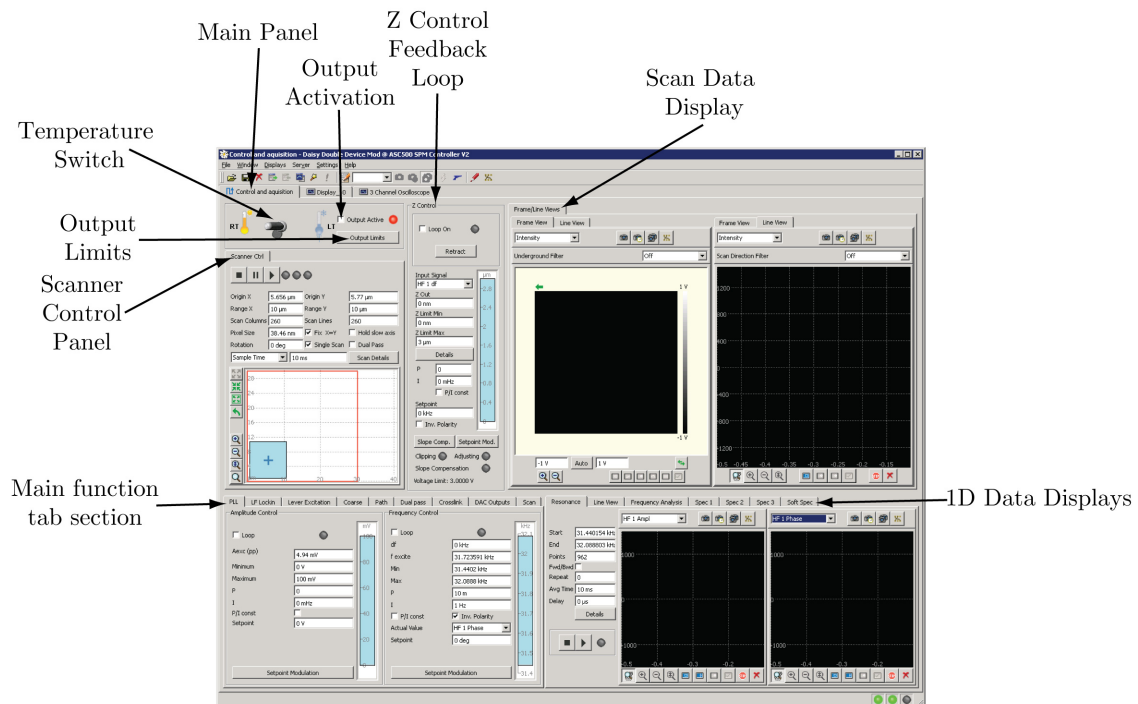


Figure A.4: Main Panel of the Daisy program containing 6 main sections. In the upper part of the panel the Output section, Scan Control, Z Control and the Scan Data Display are organized. The lower half contains two tab sections, on the left the Main function tab section and right the 1D Data Display tab section.

A.3.1 Software User Interface

In the following several screen shots of the user interface of the program are shown. The important tabs and buttons are labeled and their task is explained. Figure A.4 shows the main window and labels the six main sections.

Output Section

The upper left of the Main Panel hosts the Output section, for the activation of the controller outputs and changing the corresponding limits. The temperature switch can be used to change between low and room temperature settings. By clicking the *Output Limits* button a window opens where the actual output limits can be changed (see table A.1). By checking the *Output Active* box all electrical outputs can be activated. This only should be done when all important values were added and rechecked.

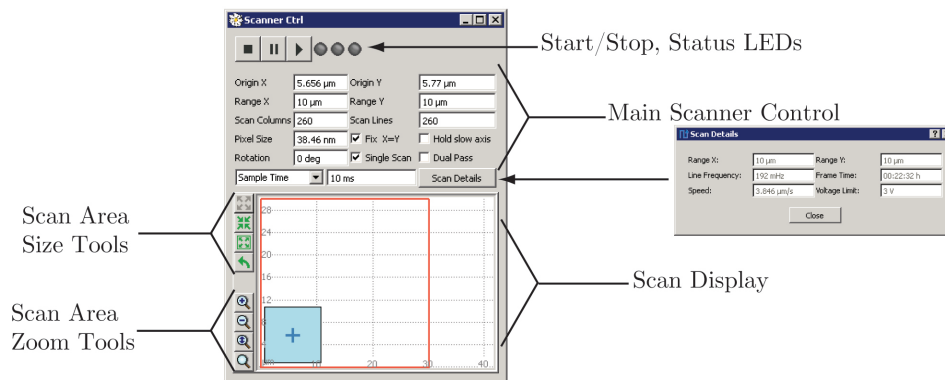


Figure A.5: The Scanner Control Panel is used to set the scan parameters and change the scan area.

Scanner Control Panel

In the *Scanner Control* panel all important scan parameters can be entered. It is shown in image A.5 in detail and labeled. The buttons to start (▶), stop (■) or pause (⏸) a scan can be found at the top. By pressing the pause button the scan movement will be held at the current scan position until the scan is resumed (▶) or aborted (■). In the Main Scanner Control part all scan parameters such as number of *Scan Lines* and *Scan Columns*, *Pixel Size* and *Sample Time* can be entered. Instead of the *Sample Time* related values like *Line Frequency*, *Scan Speed* or *Time per Frame* can be entered in the drop down menu as well. The parameters are all interconnected and calculated by the software. By clicking the *Scan Details* button all important scan parameters are presented.

The Scan Display gives an overview of the overall scan range (red square) and the Active Scan Area (blue square). To move, resize and rotate the Active Scan Area one can either use the mouse or enter the desired values in *Origin*, *Range* and *Rotation* of the Main Scanner Control. On the left of the Scan Display the Scan Area Size Tools are present, which can also be used to change the Active Scan Area. The Scan Area Zoom Tools do not change the Active Scan Area but are used to zoom in and out of the Scan Display.

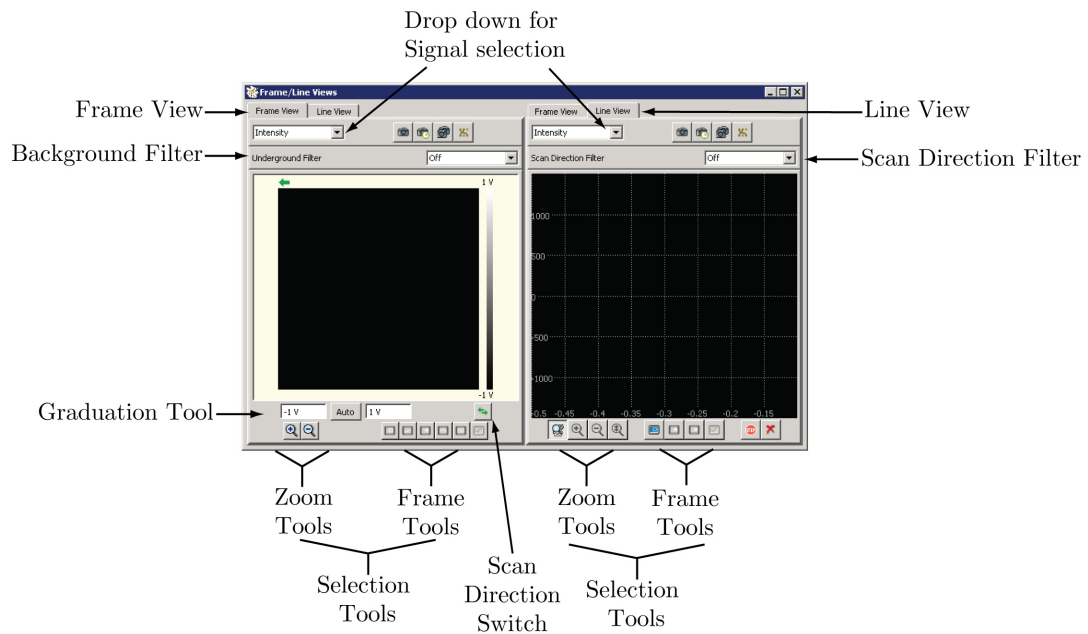


Figure A.6: The Scan Data Display panel is used to image the scan data. Two tabs allow to select either Frame or Line View.

Scan Data Display

The Scan Data Display consists of two windows showing the scan data (figure A.6). One can switch between the Frame View and Line View tab depending on the needed information. In the drop down menu the displayed signal can be selected.

In the Frame View tab the data is displayed as xy plot with a color-coded scale. By right-clicking on the window the context menu opens. Here the color coding can be changed and the Selection Tools can be activated. The *Underground Filter* allows a simple background correction while scanning. It can be used to subtract a constant or a linear function from each line. The *Graduation Tool* can be used to change contrast, by pressing the *Auto* button it calculates automatically the range of the displayed values. The Selection Tools can be divided into Zoom Tools and Frame Tools. The Frame Tools can be used to change the Active Scan Area or start the path mode. The Active Scan Area is altered based on the information selected in the Scan Display. From left to right the following functions are available:

- select a new rectangle for scanning
- rotate the scan direction
- select a new center of the scan area
- start the Pathmode

The last button on the right is only active if selections were made and is used to accept the changes.

The Pathmode allows to select a path by clicking on one or more points in the Data Display. The Pathmode can be controlled in the Main Function Tab named Path.

In the Line View tab the scan lines can be imaged while scanning. The updated value is continuously displayed in a graph as signal versus position. The *Scan Direction Filter* allows to choose between forward or backward scan and if switched off it shows both lines. By right-clicking on the window the context menu opens. Here the *Ranges* function can be used to adjust the scale in x and y and to change the amount of traces shown in the graph. The display range can also be adjusted with the Zoom Tools. The stop button (⊞) stops the display until it is cleared (⊗) or restarted by pressing stop again.

Z Control Feedback Loop

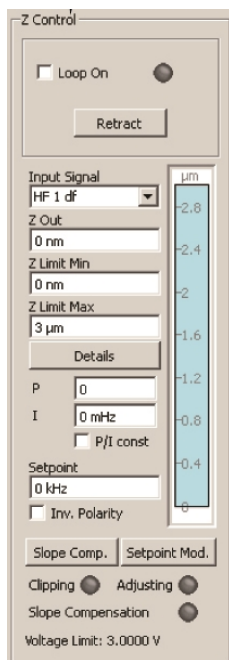


Figure A.7: Z Control Feedback Loop panel.

The Z Control Feedback Loop (fig A.7) is essential for controlling the position of the z-piezo. One can select between different *Input Signals*, for low temperature measurements it is advisable to use the HF 1 df signal together with the PLL - Frequency Control. Checking the *Loop On* box immediately activates the feedback loop which should only be done after all parameters were entered and all settings reviewed. If the *Loop On* box is unchecked while the z-piezo is extended, the feedback loop will be switched off and the position will be held. The *Retract* button also deactivates the feedback loop while retracting the piezo to *Z limit Min*. The important parameters for the feedback loop are the P and I gain values and the *Setpoint*, which depend on the measurement conditions.

Main Function Tab Section

This section contains all main functions and can be adjusted by reordering or hiding tabs. The most important tabs for low temperature applications are PLL, Lever Excitation, Coarse and Scan.

PLL: In this tab the integrated Phase Locked Loop can be controlled (fig A.8). The function of the *Frequency Control* loop is described in other parts of this thesis (see Chapter 4.1.2). Prior to a measurement the proportional and the integral gain have to be entered and the *Inv. Polarity* box must be checked. The *Actual Value* is commonly set to HF 1 Phase. If the phase is shifted to the resonance frequency at a phase of 0° , the setpoint should be set at 0° . In the lower part of the panel the *Setpoint Modulation* button is shown. This button opens a window that can be used to improve the feedback settings of the PLL. This is explained in detail in Chapter A.5.4.

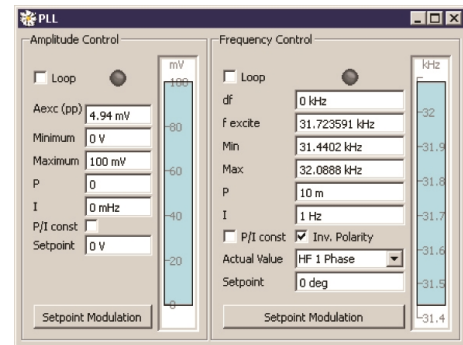


Figure A.8: PLL tab.

Lever Excitation: In this tab the tuning fork excitation can be controlled and it contains the *Q Control* settings. The resonance curve can be imaged in the Resonance tab in the 1D Data Display tab section A.3.1. The oscillation excitation (*Aexc*) influences the final amplitude of the oscillation. It should be adjusted to get an amplitude of about 50 mV. If the *Q control* is active, the excitation must not exceed 600 mV. The *Auto Phase* button is important to shift the phase to get a value of 0° at the resonance frequency. Fine tuning of the frequency can be done by turning the mouse wheel and observing the amplitude in the Line View. The settings for the mouse wheel can be changed by performing a right click on the text field.

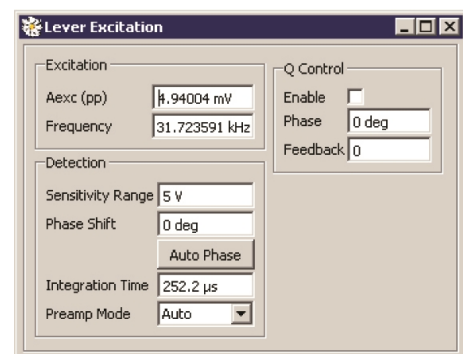


Figure A.9: Lever Excitation tab.

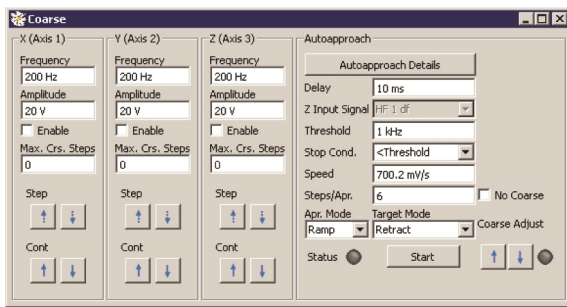


Figure A.10: Coarse tab.

defines whether the feedback loop gets activated or the tip is retracted. The approach mode (*Apr. Mode*) defines the ramp used for the z-piezo expansion. In the *Ramp* mode a constant speed is applied, which can be entered into the *Speed* cell. The *Loop* mode uses the feedback values entered in the Z Control panel. The *Z Input Signal* is defined by the selection done in the Z Control panel. The *Delay* value defines the waiting time after each coarse step and should be increased at low temperatures (to 50-100 ms). The approach speed should be around 500 mV/s and needs to be lowered for big Q factors. The amount of steps per approach (*Steps/Apr.*) is 5 for low temperatures and 3 for room temperature. If *HF 1 Ampl* is selected as input signal, the stop condition (*Stop Cond.*) has to be set to *<Threshold* and the *Threshold* to 95% of the signal amplitude. If *HF 1 df* is selected as input signal, the stop condition (*Stop Cond.*) has to be set to *>Threshold* and the *Threshold* has to be +100 mHz.

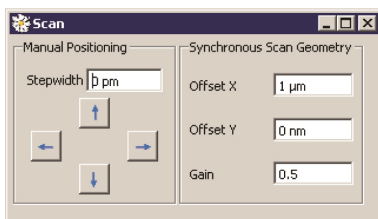


Figure A.11: Scan tab.

Scan: In the Scan Tab the *Synchronous Scan Geometry* panel is important. In the *Gain* field the gain value for the synchronous scanning has to be entered, in case of the LASFN-35 SIL it should be 0.5. Both *Offset* fields are required to fine center the tip, which will be described in more detail in section A.5.3.

Coarse: The coarse tab is used to control the positioner movement and the autoapproach of the tip (fig A.10). The autoapproach alternately controls the expansion of the z-piezo and the z-positioner movement to bring the tip near the sample. If the *Stop Condition* is met, the system will enter the *Target Mode*. It

1D Data Display Tab Section

Line View: The Line View Tab simply displays data versus time. The sampling time on the upper right corresponds to one pixel in the Line View. In the drop down menu the input signal can be chosen.

Resonance: This tab is important to find and characterize the oscillation of the tuning fork. The selected frequency window will be scanned by pressing the start button (▶). The range of this scan is defined by the inputs in the *Start* and *End* field. It is advisable to select amplitude (HF 1 Ampl) and phase (HF 1 Phase) to be displayed in the windows.

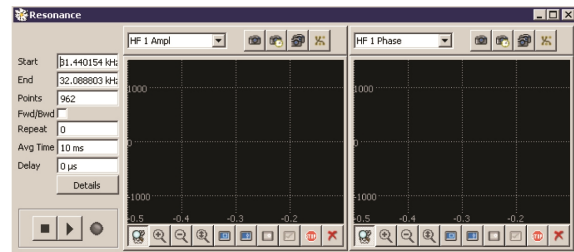


Figure A.12: Resonance tab.

In the tools below the scan window two useful Frame Tools are situated. The left one allows to select a new frequency range at which the *Start* and *End* values will be changed automatically. The right one allows to select a point in the window which will be entered as new frequency in the Lever Excitation tab. The selections made with one of the tools are applied by clicking the accept button.

A.3.2 Data Saving

This section will give an overview on how to save the measured data. The four icons shown in figure A.13 are important for triggering the data storage and defining the saving settings. They all can be found at various positions of the user



Figure A.13: Buttons for data storage.

interface. The three buttons containing a camera trigger different data storage processes. The icon at the right accesses the *Data Channel Configuration* dialog (DCC). Here the signals and the format they are saved in are defined. The DCC has separate tabs for different data channels. Most important are the Line tab on the lower half and the Scan tab in the upper half of the window. The Scan group is responsible for all data acquired during a raster-scan. For saving all data during a tip-enhanced experiment at least the following channels should be selected: *Z out in* (Topography), *HF 1 df* (error signal), *Counter* (APD1), *ADC 2* (APD2). To add more signal channels the *Add* button can be clicked and unnecessary channels can be removed by clicking the delete button at the end of the row. In the text field in the front of the row a recognizable filename should be chosen.

The checkboxes define the format in which the data is saved, to be sure all boxes should be checked.

To trigger the data storage one of the three camera buttons has to be clicked. By triggering the data storage all data of the corresponding display will be saved. For example if the Save button is clicked in the Scan Data Display, all 2D and 1D information will be saved. The button on the left is the Save Immediate button. It saves the current state of the data, independent if the scan is finished or not. In the middle the Save Delayed button is shown. It will store the data when the scan is completed and can only be activated as soon as the data acquisition started. Upon clicking the button an icon appears in the corresponding display to visualize that the data will be stored when finished. The third button is the Save Repeat button. Once it is pressed the completed data will be saved continuously. The process can be stopped by clicking the button again.

A.4 Preparations for Low Temperature Measurements

In the following the most important steps for preparing the low temperature measurements are listed. The details are described in this sections. During the experiments two webcams, which use two different programs to display the stream, are used. For the internal webcam in the head the *uEye Cockpit* software has to be used. The external camera used for tip inspection at room temperature is controlled by the *Yacam* software. The preparation is separated into five steps, which will be explained in more detail in the following.

1. Tuning fork soldering
2. Tip gluing
3. Centering SIL and tip
4. Transfer to vacuum chamber, pumping and exchange gas
5. Transfer to cryostat and cooling

A.4.1 Tuning Fork Soldering

This step is optional: If the tuning fork is handled with care and shows good low temperature behavior, it is not necessary to change it. If the scan shows strange artifacts that cannot be explained or if the Q factor is too high at low temperatures, it is advisable to change the tuning fork. Soldering should only be done when the head plate is removed from the stack.

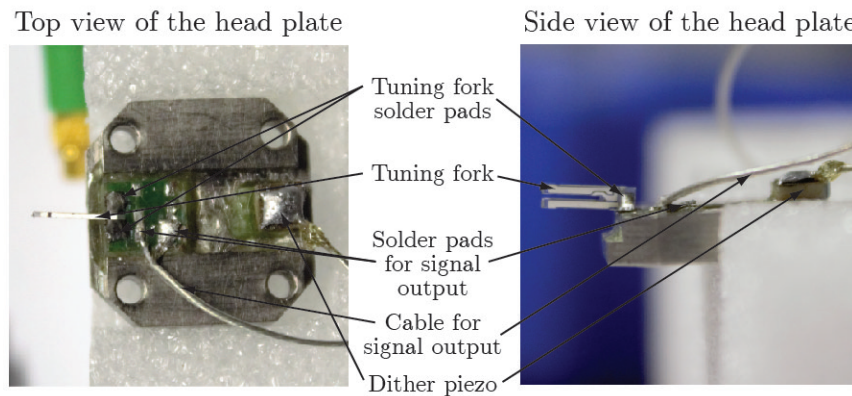


Figure A.14: Side and top view of the AFM Head plate. The main connections and solder points are named and marked.

After carefully removing the tuning fork from its capsule, the two wires at the end of the tuning fork are removed. To do so, use the soldering iron to heat the solder point of the wire until it gets loose and remove it with a pair of tweezers. Now the tuning fork has to be prepared by adding a tiny amount of solder to the solder pads, where the wires were removed from. Also, the circuit board should contain a small amount of solder, on the two patches where the tuning fork needs to be fixed. The tuning fork has to be placed at the solder position without tilting or twisting and it should be kept there in a stable position. The final soldering should be done fast, avoiding a short circuit. Both sides of the tuning fork have to be connected properly, but without using too much solder tin. At best, both contacts of the tuning fork contain the same amount of solder. The optimal orientation and position of the tuning fork is shown in figure A.14 from the side and from the top. The amount of solder visible in this image is adequate.

A.4.2 Tip Gluing

The old tip has to be removed, before gluing the new one. To do so the tip stack must be disconnected and removed from the microscope stick. Afterwards, the head plate of the tip stack has to be unscrewed and the cable to the dither piezo has to be unplugged. The four screws of the head plate should be unscrewed using the least force possible and the stack should be placed on a soft surface. Once the head plate is removed, the tip can be detached by using acetone and a sharp razor blade. One has to take care, not to add too much pressure on the tuning fork. When the tuning fork is clear of all glue residuals the head plate can be screwed back on the stack. Make sure to fix the screws only hand tight without using too much force.

Now, the tip can be prepared and cut for gluing, this is done by the standard procedure using gold wires not longer than 1.5 mm. The setup for tip gluing is shown in figure A.15. The tip stack is laid down on a foam material with a height of approximately 3 cm. The prepared tip is hold by tweezers, which are fixed with magnets to the lower position of the micrometer stage, as visible in A.15 b). After checking height and position of the tip, it is glued on the upper prong of the tuning fork using one small drop of epoxy glue. Figure A.15 a) shows the view through the microscope on a correctly positioned and oriented tip. When the glue is cured, the tweezers and the tape can be removed and the stack can be plugged back in the microscope. It is advisable to measure the resonance curve after gluing a new tip, to see if the tuning fork got loose or damaged during the process.

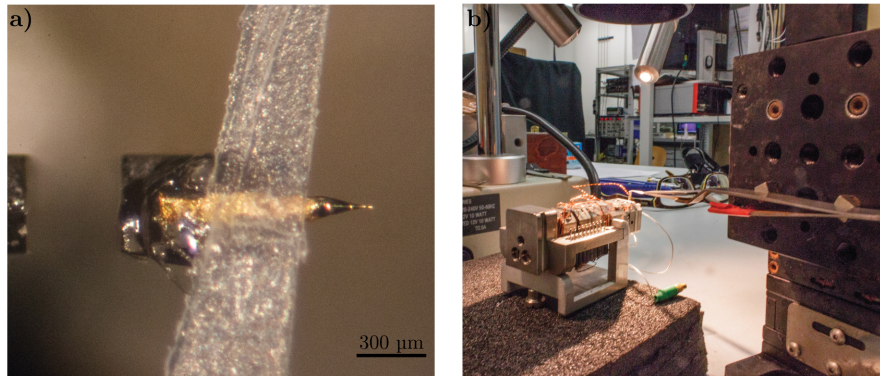


Figure A.15: Gluing a tip: a) View through the microscope on the glued tip. The tip is positioned on the upper prong of the tuning fork and fixed with a drop of epoxy glue. b) Setup for gluing a tip. The AFM stack is laid down with the tuning fork pointing up. The cut tip is hold by a pair of tweezers, fixed on the lower part of the micrometer stage.

A.4.3 Centering SIL and Tip

The new tip and the SIL should be centered at room temperature, prior to cooling. The internal webcam, integrated in the optical head, is responsible for imaging the SIL from the top, to inspect the laser focus. At first, the height of the SIL has to be adjusted by using the z positioner, until the focus looks like in figure A.16 a). For centering the SIL in x and y direction, the SIL has to be moved until the back reflection of the laser is visible. To see this back reflection the exposure time of the webcam has to be increased. Figure A.16 b) shows the resulting webcam image containing the back reflection.

The tip can be additionally visualized by an external camera. This camera uses a 6.5 zoom objective (Navitar) and images the tip and the tuning fork from the side. It is used to roughly approach and center the tip. In figure A.16 c) an image, taken with this camera at maximum zoom is shown. The tip and its reflection on the surface of the SIL is visible. On the right of the tip, the focus can be seen as a small red spot. For rough centering, the tip has to be positioned as shown. It has to be on the right side of the focus and with a small safety distance from the SIL surface. Afterwards, the integrated webcam is used to fine center the tip. For this, the illumination path has to be changed to back illumination, by flipping the mirror after the laser into the beam path. Now the SIL is illuminated from below and the webcam should show a image, like in figure A.16 d). By moving the tip with the x positioner in both directions ($\pm 100\text{-}200\ \mu\text{m}$) the shadow of the tip should become visible in the webcam. If the apex of the tip is already centered the image

should look like in A.16 e), otherwise the shadow is much bigger and sometimes covers the whole visible area. If no shadow appears, one has to move the tip with the y positioner approximately $50\ \mu\text{m}$ in positive direction. Afterwards again the x positioner has to be moved in both directions ($\pm 100\text{-}200\ \mu\text{m}$). These steps have to be repeated until the shadow of the tip is found. In picture A.16 e), the tip is still in a safe distance from the SIL surface. If no AFM measurements are needed at room temperature, it is advisable to not approach the tip further to avoid damaging it. In figure A.16 e) the tip is approximately $20\ \mu\text{m}$ away from the surface. For comparison in figure A.16 f) the tip is only $1\ \mu\text{m}$ away from the surface. To keep the tip safe during the microscope transfer and cooling, it has to be retracted 400 steps in z direction with the positioner.

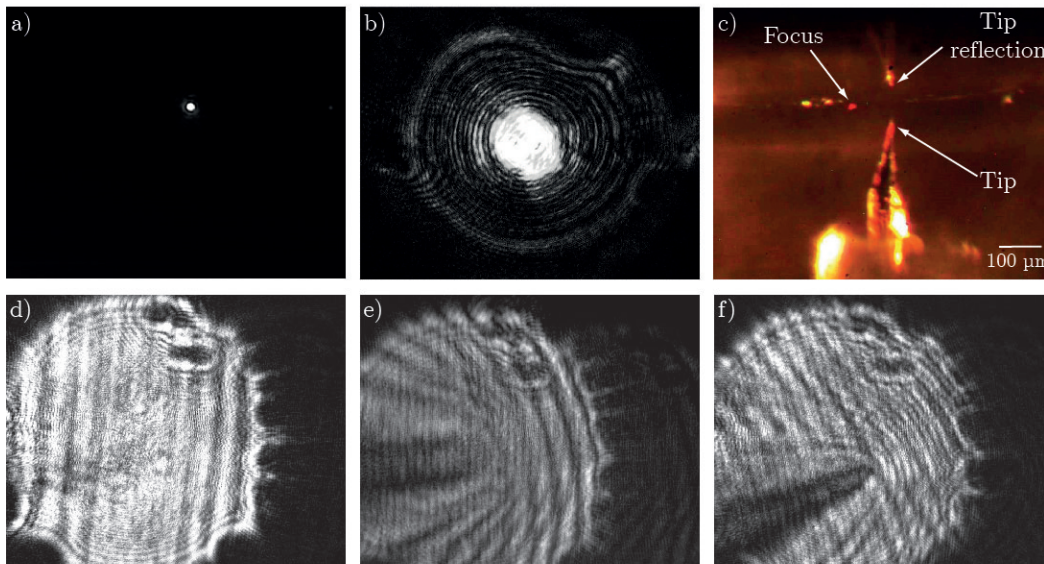


Figure A.16: Centering of tip and SIL. a) Image of the laser focus on the SIL surface, taken by the internal camera, with an exposure time of approximately $0.1\ \text{ms}$. b) Image of the laser focus and its back reflection on the SIL surface, taken by the internal camera, with an exposure time of approximately $60\ \text{ms}$. c) Side view on the tip and tuning fork, taken with the external camera with maximum zoom. d) - f) Back illumination of the SIL to visualize the shadow of the tip. All images were acquired with the internal web cam with a maximum exposure time of $62.4\ \text{ms}$. Different stages of finding and approaching the tip are shown.

A.4.4 Transfer Microscope Stick to Vacuum Chamber and Pumping Down

Before proceeding make sure the tip is retracted far enough to be safe of damage. The next step is to secure the cables at the low temperature section with aluminum tape, to prevent them to get stuck or cause a short circuit. The micro coaxial connector should be fixed in the window on the front side of the low temperature section as shown in image A.17 a). Additionally, the dither cable at the AFM stacks to be fixed by a thin strip of tape. Image A.17 b) shows how the cables have to be secured at the low temperature chamber.

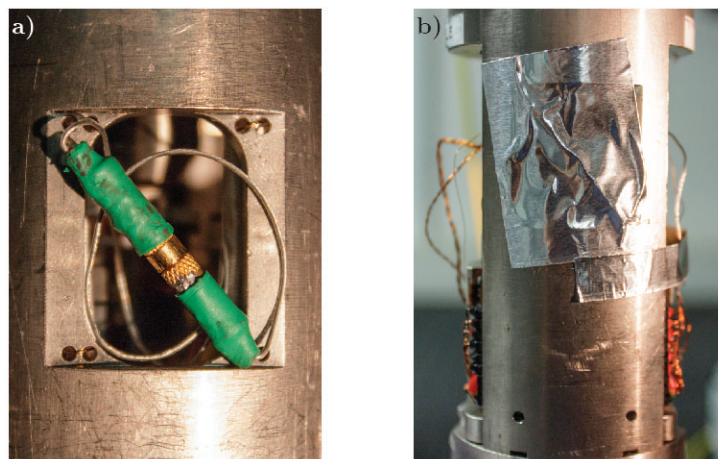


Figure A.17: The cables in the low measurement chamber have to be secured by aluminum tape. a) Position of the micro coaxial connector before covering it. b) Secured cables on the low temperature chamber, ready for transfer.

Before transferring the microscope, make sure the VÜK and the sealing ring are clean and in place. The VÜK should be positioned in its mount and fixed with its bracket. It is more secure, if the transfer is performed by two people. Remove the optical head and disconnect all cables from the microscope. Afterwards, the microscope has to be unscrewed from the holder at four positions with equal speed. Now, the microscope has to be moved to and inserted into the VÜK. During the transfer, vibrations have to be avoided and the microscope should not be touched at the measurement chamber.

The setup of the vacuum chamber and its connection to the pump is shown in figure A.18, where all important components are labeled. After the microscope is inserted in the vacuum chamber, it should be sealed by closing the clamp hand tight. To evacuate the vacuum chamber the pump has to be connected with the vacuum valve. It is advisable to connect the six multi pin Fischer connectors to the microscope during pump down. The chamber should be evacuated down to a

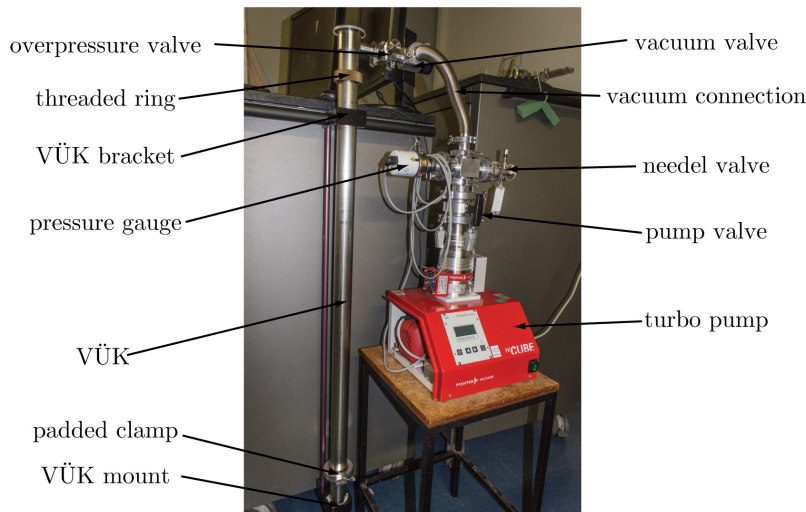


Figure A.18: Setup of the vacuum chamber and its connection to the pump. All important components of the pump and the vacuum chamber are labeled.

pressure of 10^{-5} mbar. Careful heating of the vacuum chamber with a heat gun improves cleanliness of the chamber. After the chamber is evacuated, pure helium gas is inserted to improve heat exchange during cooling. A helium pressure of about 10 mbar is suitable. The helium gas cylinder is connected to the needle valve via a pressure regulator.

A.4.5 Transfer to Cryostat and Cooling

Before transferring the microscope, make sure that all valves are closed hand-tight and that the pump and the cables are disconnected. Check if the threaded ring and the two sealing rings are wrapped around the vacuum chamber and fix the padded clamp below them, but not higher than 10 cm above the lower end of the VÜK. The position of the clamp is shown in figure A.18. Remove the bracket, that keeps the VÜK in place and lift it out of the mount. Carefully lift up the vacuum chamber and insert it into the cryostat, until it gets stopped by the padded clamp. Make sure the clamp fixes the chamber in place and quickly connect the six multi pin Fischer connectors to the microscope. This step is important because the piezos have to be connected to ground while cooling. By slightly loosening the clamp one can lower the VÜK into the cryostat in a controlled manner. After approximately two-thirds the VÜK reaches the notch inside the cryostat. Here one has to carefully recenter the VÜK to fit it into the notch. After the VÜK reaches the bottom of the cryostat the threaded ring has to be screwed down to seal the cryostat and fix the microscope in place. Now all cables and the optical head can be reconnected.

For liquid nitrogen a stable temperature is reached after 1.5 h, but complete thermalization takes longer and should be observed by monitoring the tuning fork amplitude. As long as spikes appear in the amplitude of the tuning fork, the system is not stable to measure.

A.5 Tip-enhanced Measurements

After the microscope is cooled down, the final steps towards low temperature TE-NOM have to be performed. The procedure can be separated in four steps, which will be explained in more detail in the following.

1. Center SIL and confocal inspection
2. Approach and find tip
3. Center tip for Sync scan
4. Scan parameters

A.5.1 Center SIL and Confocal Imaging

After cooling the SIL has to be recentered by using the web cam and all three sample positioner. The steps are the same as for the room temperature procedure, explained in A.4.3. Afterwards, a confocal scan should be performed, to check on the alignment of the detector and the laser.

A.5.2 Approach and Find Tip

To safely approach the tip, the stack should be moved 100 μm in positive y direction. Afterwards the tip should be approached stepwise in z direction. After every 20-30 up steps one has to look for the shadow of the tip by moving it +/- 100 μm in x direction. The change between z approach and x "scanning" have to be repeated until the shadow of the tip becomes visible. The approach is comparable to the centering at room temperature explained in A.4.3. The difference is that, at low temperatures, the tip is much further away from the SIL surface and it can not be monitored by the external webcam. If the shadow of the tip is found, it has to be approached further as long as it is safe. If the webcam image looks like A.16 e), it is advisable to start the automatic approach by the software to cover the final distance.

A.5.3 Center Tip for Sync Scan

After the scan range for the final scan is selected, the tip has to be centered. The rough centering is done as described in A.5.2, always take care of keeping a safe distance between tip and SIL, when using the positioner for rough centering. After the tip is approached and the the z-piezo is retracted the tip should be approximately 1 μm away from the SIL.

The fine centering is done by changing the offset values in the *Sync Scan* Tab of the program. The area for the sync scan and the final scanning parameters should be selected before beginning. The scan program only applies the changes in offset when the scan is already running. A simple point scan at the starting point of the scan area, to center the tip is not successful. Once the scan range is changed back, a shift of the tip position due to the programming of the sync scan occurs. Therefore, the best way to center the tip, is to start the scan (▶) and quickly press the pause button (■). In this way the scan program is active and immediately applies the changes made in the *Offset* values, to the tip position. As soon as the scanning movement is paused, the first step is to keep the tip retracted and center it while observing its shadow in the webcam. Next, the tip is landed while observing the shadow and its position is readjusted. Now, when the tip seems to be directly in the focus, the illumination should be changed to normal laser illumination from the top. By retracting and landing the tip, a change in the photoluminescence signal in channel 2 should be observed. This channel only contains the 633 nm long pass filter and is able to detect the gold signal. If the signal intensity increases while the tip is landing, the tip is already pretty close to the center of the focus. Now, the z piezo should be retracted and the pellicle beamsplitter in the optical head should be carefully flipped out of the beam path. Afterwards the tip can be landed again. Finally, by observing the gold signal, the offset values are slowly changed. The tip should be centered perfectly when the signal is maximal. Now, the scan can be stopped by pushing the stop button (■) and one can restart the scan to gain a tip-enhanced image.

A.5.4 Scan Parameters for Low Temperature Scanning

Lever excitation: Press the Auto Phase Button to center the resonance frequency at a phase of 0°

Q control: Enable , Phase = 180° , Feedback = 0.990 - 0.998

Scanner Ctrl: Scan Speed ≈ 250 nm/s and sample time = $n \times 10$ ms (with $n = 1-6$), Single Scan

Frequency Control: Loop , $P > 10$ m (often 35 m), $I < 1$ Hz (often 800 mHz), Inv. Polarity , Setpoint: 0 deg

Z Control: Input Signal: HF 1 df, $P \approx 40$ m, $I \approx 1$ Hz, Setpoint = 200 mHz

Most of these values are for orientation since every measurement is different, but in general it is safe to use them as starting point.

To find the right feedback parameters for Frequency Control it is helpful to use the *Setpoint Modulation* below the Frequency Control settings. This opens a small window where the following settings are entered: Setpoint Mod. = Periodic Rectangle, Period = 1 s, Value = 5 deg. In the *Line View* HF 1 df and HF 1 Phase should be visible. The setpoint modulation periodically changes the phase and the reaction of the feedback can be monitored. In the *Line View* of the HF 1 Phase channel a rectangular shape should be visible. If the feedback is too fast, an overshoot at the edges is visible. If the feedback is too slow, the edges become round. In the *Line View* of the HF 1 df channel, a small overshoot is always present.

When all values are set the tip can be landed by checking *Loop On* in the *Z Control* tab.

A.6 Troubleshooting

In general if there are problems, check for cold solder points or loose connections. Sometimes the software and the Scan Controller need to be restarted if the system does not respond properly. Since all optical signals are transported via fibers the imaging is sensitive to changes of the beam path.

Table A.2: Troubleshooting.

Error	Solution
No counts	Check the Exposure time: Settings →Experiment Preferences →Counter →Exposure Time: 10 ms
	Check the BNC and power connections
	Readjust the downwards mirror in the head. It shifts slightly if the head is moved to fast
Low PL resolution or contrast	Check if the mode converter is switched on and if the mode of the laser is correct
	Check if the laser is completely coupled into the fiber
	Clean the objective from accumulated dust
	Readjust the downwards mirror in the head. It shifts slightly if the head is moved to fast
Resonance curve low or unsymmetrical	Check Tuning fork soldering and connection between the micro coax plugs
	Check dither soldering and dither plug
Noise in amplitude or topography	Check Tuning fork soldering and connection between the micro coax plugs
	Check dither soldering and dither plug
	Check if the positioner outputs are all enabled
	Check if the halogen lamps at the ceiling are switched off
	Thermalization after cooling down can take up to several hours until then spikes are often visible
Positioner does not move	Increase the the voltage for a short time up to 50V and try to move it

Bibliography

- [1] Bundesministerium für Bildung und Forschung (BMBF). *Nano.de-Report – Status Quo der Nanotechnologie in Deutschland*. Referat Neue Werkstoffe; Nanotechnologie; KIT, 2013.
- [2] C. Kisielowski et al. “Detection of Single Atoms and Buried Defects in Three Dimensions by Aberration-Corrected Electron Microscope with 0.5-Å Information Limit”. *Microsc. Microanal.* **14** (2008), p. 469.
- [3] Nobel Media AB 2014. *The Nobel Prize in Chemistry 2014*. Ed. by Nobelprize.org. 24/2016. URL: http://www.nobelprize.org/nobel_prizes/chemistry/laureates/2014/.
- [4] S. W. Hell. “Far-Field optical Nanoscopy”. *Science* **316** (2007), p. 1153.
- [5] S. W. Hell, S. J. Sahl, M. Bates, X. Zhuang, R. Heintzmann, M. J. Booth, J. Bewersdorf, G. Shtengel, H. Hess, and P. Tinnefeld. “The 2015 super-resolution microscopy roadmap”. *J. Phys. D: Appl. Phys.* **48** (2015), p. 443001.
- [6] N. Paradiso, F. Yaghobian, C. Lange, T. Korn, C. Schüller, R. Huber, and C. Strunk. “Tailored nanoantennas for directional Raman studies of individual carbon nanotubes”. *Phys. Rev. B* **91** (2015), p. 235449.
- [7] M. Liao, S. Jiang, C. Hu, R. Zhang, Y. Kuang, J. Zhu, Y. Zhang, and Z. Dong. “Tip-Enhanced Raman Spectroscopic Imaging of Individual Carbon Nanotubes with Subnanometer Resolution”. *Nano Lett.* **16** (2016), p. 4040.
- [8] P. Patoka et al. “Nanoscale plasmonic phenomena in CVD-grown MoS₂ monolayer revealed by ultra-broadband synchrotron radiation based nano-FTIR spectroscopy and near-field microscopy”. *Opt. Express* **24** (2016), p. 1154.
- [9] J. Stadler, T. Schmid, and R. Zenobi. “Nanoscale Chemical Imaging of Single-Layer Graphene”. *ACS Nano* **5** (2011), p. 8442.

- [10] E. Lipiec, R. Sekine, J. Bielecki, W. M. Kwiatek, and B. R. Wood. “Molecular Characterization of DNA Double Strand Breaks with Tip-Enhanced Raman Scattering”. *Angew. Chem. Int. Ed.* **53** (2014), p. 169.
- [11] G. Rusciano, G. Zito, R. Isticato, T. Sirec, E. Ricca, E. Bailo, and A. Sasso. “Nanoscale Chemical Imaging of Bacillus subtilis Spores by Combining Tip-Enhanced Raman Scattering and Advanced Statistical Tools”. *ACS Nano* **8** (2014), p. 12300.
- [12] H. F. Hess, E. Betzig, T. D. Harris, L. N. Pfeiffer, and K. W. West. “Near-Field Spectroscopy of the Quantum Constituents of a Luminescent System”. *Science* **264** (1994), p. 1740.
- [13] Y. Toda, S. Shinomori, K. Suzuki, and Y. Arakawa. “Near-field magneto-optical spectroscopy of single self-assembled InAs quantum dots”. *Appl. Phys. Lett.* **73** (1998), p. 517.
- [14] J. L. Merz, A. M. Mintairov, T. Kosel, and K. Sun. “Exciton localisation in InGaAsN and GaAsSbN observed by near-field magnetoluminescence and scanning optical microscopy (NSOM)”. *IEE Proceedings - Optoelectronics* **151** (2004), p. 346.
- [15] A. Kiriwara, S. Kono, A. Tomita, and K. Nakamura. “Development of Scanning Near-Field Optical Microscope Working under Cryogenic Temperature and Strong Magnetic Field”. *Opt. Rev.* **13** (2006), p. 279.
- [16] R. D. Grober, T. D. Harris, J. K. Trautman, and E. Betzig. “Design and implementation of a low temperature near-field scanning optical microscope”. *Rev. Sci. Instrum.* **65** (1994), p. 626.
- [17] H. U. Yang, E. Hebestreit, E. E. Josberger, and M. B. Raschke. “A cryogenic scattering-type scanning near-field optical microscope”. *Rev. Sci. Instrum.* **84** (2013).
- [18] T. Saiki, K. Nishi, and M. Ohtsu. “Low Temperature Near-Field Photoluminescence Spectroscopy of InGaAs Single Quantum Dots”. *Jpn. J. Appl. Phys.* **37** (1998), p. 1638.
- [19] G. Behme, A. Richter, M. Süptitz, and C. Lienau. “Vacuum near-field scanning optical microscope for variable cryogenic temperatures”. *Rev. Sci. Instrum.* **68** (1997), p. 3458.

-
- [20] S. Paddock. “Principles and practices of laser scanning confocal microscopy”. *Mol. Biotechnol.* **16** (2000), p. 127.
- [21] E. Betzig and R. Chichester. “Single molecules observed by near-field scanning optical microscopy.” *Science* **262** (1993), p. 1422.
- [22] B. Hecht, B. Sick, U. Wild, V. Deckert, and R. Zenobi. “Scanning near-field optical microscopy with aperture probes: Fundamentals and applications”. *J. Chem. Phys.* **112** (2000), p. 7761.
- [23] L. Novotny and B. Hecht, eds. *Principles of Nano-optics*. Cambridge University Press, 2006.
- [24] M. Born and E. Wolf. *Principles of Optics*. 7th. Cambridge University Press, 1999.
- [25] L. Novotny. “The history of near-field optics”. *Progress in Optics*. Ed. by E. Wolf. Vol. 50. Progress in Optics. Elsevier, 2007, p. 137.
- [26] B.-S. Yeo, J. Stadler, T. Schmid, R. Zenobi, and W. Zhang. “Tip-enhanced Raman Spectroscopy - Its status, challenges and future directions”. *Chem. Phys. Lett.* **472** (2009), p. 1.
- [27] T. Ming, H. Chen, R. Jiang, Q. Li, and J. Wang. “Plasmon-Controlled Fluorescence: Beyond the Intensity Enhancement”. *J. Phys. Chem. Lett.* **3** (2012), p. 191.
- [28] B. Pettinger, P. Schambach, C. J. Villagómez, and N. Scott. “Tip-Enhanced Raman Spectroscopy: Near-Fields Acting on a Few Molecules”. *Annu. Rev. Phys. Chem.* **63** (2012), p. 379.
- [29] J. M. Atkin, S. Berweger, A. C. Jones, and M. B. Raschke. “Nano-optical imaging and spectroscopy of order, phases, and domains in complex solids”. *Adv. Phys.* **61** (2012), p. 745.
- [30] C. Georgi, M. Böhmler, H. Qian, L. Novotny, and A. Hartschuh. “Tip-Enhanced Near-Field Optical Microscopy of Carbon Nanotubes”. *Raman Imaging: Techniques and Applications*. Ed. by A. Zoubir. Berlin, Heidelberg: Springer Berlin Heidelberg, 2012, p. 301.
- [31] M. Böhmler and A. Hartschuh. “Tip-Enhanced Near-Field Optical Microscopy of Quasi-1D Nanostructures”. *ChemPhysChem* **13** (2012), p. 927.

- [32] J. S. Reparaz et al. “Probing local strain and composition in Ge nanowires by means of tip-enhanced Raman scattering”. *Nanotechnology* **24** (2013), p. 185704.
- [33] M. Lucas and E. Riedo. “Invited Review Article: Combining scanning probe microscopy with optical spectroscopy for applications in biology and materials science”. *Rev. Sci. Instrum.* **83** (2012), p. 061101.
- [34] B. R. Wood, M. Asghari-Khiavi, E. Bailo, D. McNaughton, and V. Deckert. “Detection of Nano-Oxidation Sites on the Surface of Hemoglobin Crystals Using Tip-Enhanced Raman Scattering”. *Nano Lett.* **12** (2012), p. 1555.
- [35] P. Bhatadwaj, B. Deutsch, and L. Novotny. “Optical Antennas”. *Adv. Opt. Photonics* **1** (2009), p. 438.
- [36] M. Agio and A. Alú, eds. *Optical Antennas*. Cambridge: Cambridge University Press, 2013.
- [37] L. Novotny and N. van Hulst. “Antennas for light”. *Nat. Photon.* **5** (2011), p. 83.
- [38] R. L. Olmon and M. B. Raschke. “Antenna-load interactions at optical frequencies: impedance matching to quantum systems”. *Nanotechnology* **23** (2012), p. 444001.
- [39] N. Mauser and A. Hartschuh. “Tip-enhanced near-field optical microscopy”. *Chem. Soc. Rev.* **43** (2014), p. 1248.
- [40] X. Shi, N. Coca-López, J. Janik, and A. Hartschuh. “Advances in Tip-Enhanced Near-Field Raman Microscopy Using Nanoantennas”. *Chem. Rev.* (2017), DOI: 10.1021/acs.chemrev.6b00640.
- [41] A. L. Demming, F. Festy, and D. Richards. “Plasmon resonances on metal tips: Understanding tip-enhanced Raman scattering”. *J. Phys. Chem. Lett.* **122** (2005), p. 184716.
- [42] N. Kazemi-Zanjani, S. Vedraïne, and F. Lagugné-Labarthe. “Localized enhancement of electric field in tip-enhanced Raman spectroscopy using radially and linearly polarized light”. *Opt. Express* **21** (2013), p. 25271.
- [43] Z. Yang, J. Aizpurua, and H. Xu. “Electromagnetic field enhancement in TERS configurations”. *J. Raman Spectrosc.* **40** (2009), p. 1343.

-
- [44] I. Notingher and A. Elfick. “Effect of Sample and Substrate Electric Properties on the Electric Field Enhancement at the Apex of SPM Nanotips”. *J. Phys. Chem. B* **109** (2005), p. 15699.
- [45] V. V. Gozhenko, L. G. Grechko, and K. W. Whites. “Electrodynamics of spatial clusters of spheres: Substrate effects”. *Phys. Rev. B* **68** (2003), p. 125422.
- [46] S. F. Becker, M. Esmann, K. Yoo, P. Gross, R. Vogelgesang, N. Park, and C. Lienau. “Gap-Plasmon-Enhanced Nanofocusing Near-Field Microscopy”. *ACS Photonics* **3** (2016), p. 223.
- [47] W. Zhu, R. Esteban, A. G. Borisov, J. J. Baumberg, P. Nordlander, H. J. Lezec, J. Aizpurua, and K. B. Crozier. “Quantum mechanical effects in plasmonic structures with subnanometre gaps”. *Nat. Commun.* **7** (2016), p. 11495.
- [48] A. Hartschuh. “Tip-Enhanced Near-Field Optical Microscopy”. *Angew. Chem. Int. Ed.* **47** (2008), p. 8178.
- [49] M. Sakai, Y. Inose, T. Ohtsuki, K. Ema, K. Kishino, and T. Saiki. “Near-field optical imaging of light localization in GaN nanocolumn system”. *Jpn. J. Appl. Phys.* **53** (2014), p. 030301.
- [50] A. V. Ankudinov, A. M. Mintairov, S. Slipchenko, A. Shelaev, M. Yanul, P. S. Dorozhkin, and N. Vishnyakov. “Scanning Near-Field Optical Microscopy of Light Emitting Semiconductor Nanostructures”. *Ferroelectrics* **477** (2015), p. 65.
- [51] G. Kolhatkar, A. Boucherif, C. Dab, S. Fafard, V. Aimez, R. Ares, and A. Ruediger. “Composition variation in Al-based dilute nitride alloys using apertureless scanning near-field optical microscopy”. *Phys. Chem. Chem. Phys.* **18** (2016), p. 30546.
- [52] R. Zhang, Y. Zhang, Z. Dong, S. Jiang, and C. Zhang. “Chemical mapping of a single molecule by plasmon-enhanced Raman scattering.” *Nature* **498** (2013), p. 82.
- [53] M. K. Schmidt and J. Aizpurua. “Nanocavities: Optomechanics goes molecular”. *Nat. Nanotechnol.* **11** (2016), p. 114.
- [54] M. K. Schmidt, R. Esteban, A. González-Tudela, G. Giedke, and J. Aizpurua. “Quantum Mechanical Description of Raman Scattering from Molecules in Plasmonic Cavities”. *ACS Nano* **10** (2016), p. 6291.

- [55] L. Meng, Z. Yang, J. Chen, and M. Sun. “Effect of Electric Field Gradient on Sub-nanometer Spatial Resolution of Tip-enhanced Raman Spectroscopy”. *Sci. Rep.* **5** (2015), p. 9240.
- [56] W. E. Moerner and L. Kador. “Optical detection and spectroscopy of single molecules in a solid”. *Phys. Rev. Lett.* **62** (1989), p. 2535.
- [57] W. Göhde, J. Tittel, T. Basché, C. Bräuchle, U. C. Fischer, and H. Fuchs. “A low-temperature scanning confocal and near-field optical microscope”. *Rev. Sci. Instrum.* **68** (1997), p. 2466.
- [58] I. Manke, D. Pahlke, J. Lorbacher, W. Busse, T. Kalka, W. Richter, and M. Dähne-Prietsch. “A low-temperature scanning near-field optical microscope for photoluminescence at semiconductor structures”. *Appl. Phys. A* **66** (1998), S381.
- [59] A. Kramer, J.-M. Segura, A. Hunkeler, A. Renn, and B. Hecht. “A cryogenic scanning near-field optical microscope with shear-force gapwidth control”. *Rev. Sci. Instrum.* **73** (2002), p. 2937.
- [60] J. Michaelis, C. Hettich, J. Mlynek, and V. Sandoghdar. “Optical microscopy using a single-molecule light source”. *Nature* **405** (2000), p. 325.
- [61] R. Hillenbrand, T. Taubner, and F. Keilmann. “Phonon-enhanced light-matter interaction at the nanometre scale”. *Nature* **418** (2002), p. 159.
- [62] J. Döring, H.-G. von Ribbeck, M. Fehrenbacher, S. C. Kehr, and L. M. Eng. “Near-field resonance shifts of ferroelectric barium titanate domains upon low-temperature phase transition”. *Appl. Phys. Lett.* **105** (2014).
- [63] Y. T. Chen, K. F. Karlsson, J. Birch, and P. O. Holtz. “Determination of critical diameters for intrinsic carrier diffusion-length of GaN nanorods with cryo-scanning near-field optical microscopy”. *Sci. Rep.* **6** (2016), p. 21482.
- [64] J. Steidtner and B. Pettinger. “High-resolution microscope for tip-enhanced optical processes in ultrahigh vacuum”. *Rev. Sci. Instrum.* **78** (2007), p. 103104.
- [65] C. J. Chen. *Introduction to Scanning Tunneling Microscopy*. Oxford University Press, 1993.

-
- [66] R. Wiesendanger. *Scanning Probe Microscopy and Spectroscopy: Methods and Applications*. Cambridge University Press, 1994.
- [67] J. Steidtner and B. Pettinger. “Tip-Enhanced Raman Spectroscopy and Microscopy on Single Dye Molecules with 15 nm Resolution”. *Phys. Rev. Lett.* **100** (2008), p. 236101.
- [68] S. Jiang, Y. Zhang, R. Zhang, C. Hu, M. Liao, Y. Luo, J. Yang, Z. Dong, and G. Hou. “Distinguishing adjacent molecules on a surface using plasmon-enhanced Raman scattering”. *Nat. Nanotechnol.* **10** (2015), p. 865.
- [69] J. M. Klingsporn, N. Jiang, E. A. Pozzi, M. D. Sonntag, D. Chulhai, T. Seideman, L. Jensen, M. C. Hersam, and R. P. V. Duyne. “Intramolecular Insight into Adsorbate-Substrate Interactions via Low-Temperature, Ultrahigh-Vacuum Tip-Enhanced Raman Spectroscopy”. *J. Am. Chem. Soc.* **136** (2014), p. 3881.
- [70] A. Jorio, M. Dresselhaus, and G. Dresselhaus, eds. *Carbon Nanotubes*. Vol. 111. Topics in Applied Physics. Springer Berlin Heidelberg, 2008.
- [71] S. Reich, C. Thomsen, and J. Maultsch. *Carbon Nanotubes: Basic Concepts and Physical Properties*. Wiley-VCH Verlag GmbH & Co. KGaA, Weinheim, 2004.
- [72] C. Georgi. “Exciton Mobility and Localized Defects in single Carbon Nanotubes studied with Tip-Enhanced Near-Field Optical Microscopy”. PhD thesis. Ludwig-Maximilians-Universität München, 2011.
- [73] Y. Miyauchi. “Photoluminescence studies on exciton photophysics in carbon nanotubes”. *J. Mater. Chem. C* **1** (2013), p. 6499.
- [74] K. Matsuda, T. Inoue, Y. Murakami, S. Maruyama, and Y. Kanemitsu. “Exciton dephasing and multiexciton recombinations in a single carbon nanotube”. *Phys. Rev. B* **77** (2008), p. 033406.
- [75] D. Karaiskaj, C. Engtrakul, T. McDonald, M. J. Heben, and A. Mascarenhas. “Intrinsic and Extrinsic Effects in the Temperature-Dependent Photoluminescence of Semiconducting Carbon Nanotubes”. *Phys. Rev. Lett.* **96** (2006), p. 106805.

- [76] I. B. Mortimer and R. J. Nicholas. “Role of Bright and Dark Excitons in the Temperature-Dependent Photoluminescence of Carbon Nanotubes”. *Phys. Rev. Lett.* **98** (2007), p. 027404.
- [77] K. Yoshikawa, R. Matsunaga, K. Matsuda, and Y. Kanemitsu. “Mechanism of exciton dephasing in a single carbon nanotube studied by photoluminescence spectroscopy”. *Appl. Phys. Lett.* **94** (2009), p. 093109.
- [78] Y.-Z. Ma, M. W. Graham, G. R. Fleming, A. A. Green, and M. C. Hersam. “Ultrafast Exciton Dephasing in Semiconducting Single-Walled Carbon Nanotubes”. *Phys. Rev. Lett.* **101** (2008), p. 217402.
- [79] P. B. Allen and M. Cardona. “Theory of the temperature dependence of the direct gap of germanium”. *Phys. Rev. B* **23** (1981), p. 1495.
- [80] P. B. Allen and M. Cardona. “Temperature dependence of the direct gap of Si and Ge”. *Phys. Rev. B* **27** (1983), p. 4760.
- [81] L. Viña, S. Logothetidis, and M. Cardona. “Temperature dependence of the dielectric function of germanium”. *Phys. Rev. B* **30** (1984), p. 1979.
- [82] S. B. Cronin et al. “Temperature Dependence of the Optical Transition Energies of Carbon Nanotubes: The Role of Electron-Phonon Coupling and Thermal Expansion”. *Phys. Rev. Lett.* **96** (2006), p. 127403.
- [83] R. B. Capaz, C. D. Spataru, P. Tangney, M. L. Cohen, and S. G. Louie. “Temperature Dependence of the Band Gap of Semiconducting Carbon Nanotubes”. *Phys. Rev. Lett.* **94** (2005), p. 036801.
- [84] F. Vialla, Y. Chassagneux, R. Ferreira, C. Roquelet, C. Diederichs, G. Cas-sabois, P. Roussignol, J. S. Lauret, and C. Voisin. “Unifying the Low-Temperature Photoluminescence Spectra of Carbon Nanotubes: The Role of Acoustic Phonon Confinement”. *Phys. Rev. Lett.* **113** (2014), p. 057402.
- [85] A. Högele, C. Galland, M. Winger, and A. Imamoglu. “Photon Antibunching in the Photoluminescence Spectra of a Single Carbon Nanotube”. *Phys. Rev. Lett.* **100** (2008), p. 217401.
- [86] J. Lefebvre, P. Finnie, and Y. Homma. “Temperature-dependent photoluminescence from single-walled carbon nanotubes”. *Phys. Rev. B* **70** (2004), p. 045419.

-
- [87] R. Matsunaga, Y. Miyauchi, K. Matsuda, and Y. Kanemitsu. “Symmetry-induced nonequilibrium distributions of bright and dark exciton states in single carbon nanotubes”. *Phys. Rev. B* **80** (2009), p. 115436.
- [88] Y. Miyauchi, M. Iwamura, S. Mouri, T. Kawazoe, M. Ohtsu, and K. Matsuda. “Brightening of excitons in carbon nanotubes on dimensionality modification”. *Nat. Photon.* **7** (2013), p. 715.
- [89] S. Mouri, Y. Miyauchi, M. Iwamura, and K. Matsuda. “Temperature dependence of photoluminescence spectra in hole-doped single-walled carbon nanotubes: Implications of trion localization”. *Phys. Rev. B* **87** (2013), p. 045408.
- [90] V. Perebeinos, J. Tersoff, and P. Avouris. “Radiative Lifetime of Excitons in Carbon Nanotubes”. *Nano Lett.* **5** (2005), p. 2495.
- [91] C. D. Spataru, S. Ismail-Beigi, R. B. Capaz, and S. G. Louie. “Theory and *Ab Initio* Calculation of Radiative Lifetime of Excitons in Semiconducting Carbon Nanotubes”. *Phys. Rev. Lett.* **95** (2005), p. 247402.
- [92] J. Kastner, T. Pichler, H. Kuzmany, S. Curran, W. Blau, D. Weldon, M. Delamesiere, S. Draper, and H. Zandbergen. “Resonance Raman and infrared spectroscopy of carbon nanotubes”. *Chem. Phys. Lett.* **221** (1994), p. 53.
- [93] M. Böhmler, N. Hartmann, C. Georgi, F. Hennrich, A. A. Green, M. C. Hersam, and A. Hartschuh. “Enhancing and redirecting carbon nanotube photoluminescence by an optical antenna”. *Opt. Express* **18** (2010), p. 16443.
- [94] M. Böhmler. “Tip-Enhanced near-field optical microscopy on the quasi 1D semiconductors carbon nanotubes and CdSe nanowires”. PhD thesis. Ludwig-Maximilians-Universität München, 2012.
- [95] T. H. Taminiau, F. D. Stefani, and N. F. van Hulst. “Single emitters coupled to plasmonic nano-antennas: angular emission and collection efficiency”. *New J. Phys.* **10** (2008), p. 105005.
- [96] S. Kühn and V. Sandoghdar. “Modification of single molecule fluorescence by a scanning probe”. *Appl. Phys. B* **84** (2006), p. 211.
- [97] S. M. Mansfield. “Solid immersion Microscopy”. PhD thesis. Stanford University, 1992.

- [98] S. M. Mansfield and G. S. Kino. “Solid immersion microscope”. *Appl. Phys. Lett.* **57** (1990), p. 2615.
- [99] S. Moehl, H. Zhao, B. D. Don, S. Wachter, and H. Kalt. “Solid immersion lens-enhanced nano-photoluminescence: Principle and applications”. *J. Appl. Phys.* **93** (2003), p. 6265.
- [100] S.-Y. Yim, J.-H. Kim, and J.-M. Lee. “Solid Immersion Lens Microscope for Spectroscopy of Nanostructure Materials”. *J. Opt. Soc. Korea* **15** (2011), p. 78.
- [101] K. A. Serrels, E. Ramsay, P. A. Dalgarno, B. Gerardot, J. O’Connor, R. H. Hadfield, R. Warburton, and D. Reid. “Solid immersion lens applications for nanophotonic devices”. *J. Nanophotonics* **2** (2008), p. 021854.
- [102] M. Baba, T. Sasaki, M. Yoshita, and H. Akiyama. “Aberrations and allowances for errors in a hemisphere solid immersion lens for submicron-resolution photoluminescence microscopy”. *J. Appl. Phys.* **85** (1999), p. 6923.
- [103] B. Goldberg, S. Ippolito, L. Novotny, Z. Liu, and M. Ünlü. “Immersion lens microscopy of photonic nanostructures and quantum dots”. *IEEE J. Sel. Topics in Quantum Electron.* **8** (2002), p. 1051.
- [104] L. P. Ghislain and V. B. Elings. “Near-field scanning solid immersion microscope”. *Appl. Phys. Lett.* **72** (1998), p. 2779.
- [105] S. B. Ippolito, B. B. Goldberg, and M. S. Ünlü. “Theoretical analysis of numerical aperture increasing lens microscopy”. *J. Appl. Phys.* **97** (2005), p. 053105.
- [106] K. Koyama, M. Yoshita, M. Baba, T. Suemoto, and H. Akiyama. “High collection efficiency in fluorescence microscopy with a solid immersion lens”. *Appl. Phys. Lett.* **75** (1999), p. 1667.
- [107] R. Chen, K. Agarwal, C. J. R. Sheppard, J. C. H. Phang, and X. Chen. “Resolution of aplanatic solid immersion lens based microscopy”. *J. Opt. Soc. Am. A* **29** (2012), p. 1059.
- [108] T. D. Milster, J. S. Jo, and K. Hirota. “Roles of propagating and evanescent waves in solid immersion lens systems”. *Appl. Opt.* **38** (1999), p. 5046.

-
- [109] A. N. Vamivakas, R. D. Younger, B. B. Goldberg, A. K. Swan, M. S. Ünlü, E. R. Behringer, and S. B. Ippolito. “A case study for optics: The solid immersion microscope”. *Am. J. Phys* **76** (2008), p. 758.
- [110] R. García and A. San Paulo. “Attractive and repulsive tip-sample interaction regimes in tapping-mode atomic force microscopy”. *Phys. Rev. B* **60** (1999), p. 4961.
- [111] B. Voigtländer, ed. *Scanning Probe Microscopy*. Springer-Verlag Berlin Heidelberg, 2015.
- [112] T. R. Albrecht, P. Grütter, D. Horne, and D. Rugar. “Frequency modulation detection using high Q cantilevers for enhanced force microscope sensitivity”. *J. Appl. Phys.* **69** (1991), p. 668.
- [113] B. Bhushan and S. Kawata, eds. *Applied Scanning Probe Methods VI*. Springer-Verlag Berlin Heidelberg, 2007.
- [114] J. Mertz, O. Marti, and J. Mlynek. “Regulation of a microcantilever response by force feedback”. *Appl. Phys. Lett.* **62** (1993), p. 2344.
- [115] J. Jahng, M. Lee, H. Noh, Y. Seo, and W. Jhe. “Active Q control in tuning-fork-based atomic force microscopy”. *Appl. Phys. Lett.* **91** (2007), p. 023103.
- [116] J. Rychen, T. Ihn, P. Studerus, A. Herrmann, K. Ensslin, H. J. Hug, P. J. A. van Schendel, and H. J. Güntherodt. “Operation characteristics of piezoelectric quartz tuning forks in high magnetic fields at liquid helium temperatures”. *Rev. Sci. Instrum.* **71** (2000), p. 1695.
- [117] B. Ren, G. Picardi, and B. Pettinger. “Preparation of gold tips suitable for tip-enhanced Raman spectroscopy and light emission by electrochemical etching”. *Rev. Sci. Instrum.* **75** (2004), p. 837.
- [118] C. Williams and D. Roy. “Fabrication of gold tips suitable for tip-enhanced Raman spectroscopy”. *J. Vac. Sci. Technol. B* **26** (2008), p. 1761.
- [119] L. Eligal, F. Culfaz, V. McCaughan, N. I. Cade, and D. Richards. “Etching gold tips suitable for tip-enhanced near-field optical microscopy”. *Rev. Sci. Instrum.* **80** (2009), p. 033701.

- [120] W. H. J. Rensen, N. F. van Hulst, A. G. T. Ruiter, and P. E. West. “Atomic steps with tuning-fork-based noncontact atomic force microscopy”. *Appl. Phys. Lett.* **75** (1999), p. 1640.
- [121] L. Novotny, E. Sanches, and X. Xie. “Near-Field optical imaging using metal tips illuminated by higher-order Hermite-Gaussian beams”. *Ultramicroscopy* **71** (1998), p. 21.
- [122] A. Bouhelier, J. Renger, M. R. Beversluis, and L. Novotny. “Plasmon-coupled tip-enhanced near-field optical microscopy”. *J. Microsc.* **210** (2003), p. 220.
- [123] N. Mauser, D. Piatkowski, T. Mancabelli, M. Nyk, S. Mackowski, and A. Hartschuh. “Tip Enhancement of Upconversion Photoluminescence from Rare Earth Ion Doped Nanocrystals”. *ACS Nano* **9** (2015), p. 3617.
- [124] N. Anderson, P. Anger, A. Hartschuh, and L. Novotny. “Subsurface Raman Imaging with Nanoscale Resolution”. *Nano Lett.* **6** (2006), p. 744.

List of Abbreviations

AFM	atomic force microscope
APD	avalanche photo diode
DOS	density of states
FWHM	full width at half maximum
IR	infrared
LED	light-emitting diode
NA	numerical aperture
NIR	near-infrared
PALM	photo activated localization microscopy
PL	photoluminescence
PLL	phase-locked loop
SEM	scanning electron microscopy
SIL	solid immersion lens
SNOM	scanning near-field optical microscopy
STED	stimulated emission depletion
STM	scanning tunneling microscopy
STORM	stochastic optical reconstruction microscopy
SWCNT	single-walled carbon nanotube
TEM	transmission electron microscopy
TENOM	tip-enhanced near-field optical microscopy
TERS	tip-enhanced Raman scattering
TIR	total internal reflection
UHV	ultra high vacuum
vHS	van Hove singularity

List of Figures

2.1	Schematic of the optical scattering problem	6
2.2	Coupling of an optical antenna	11
3.1	Rolling up a SWCNT	22
3.2	SWCNT band structure	24
3.3	Temperature dependence of the optical properties of CNT	25
4.1	Signal channel inside the optical head	30
4.2	Scheme of the low-temperature near-field optical microscope setup	31
4.3	Radiation pattern	33
4.4	Solid immersion lens	34
4.5	Fields in the focal plane	36
4.6	Synchronous scanning	37
4.7	Scheme of the phase-locked loop detection	39
4.8	Q control phase map	41
4.9	Resonance curves with different Q factor	42
4.10	Schematic setup for electrochemical etching of sharp gold tips	43
4.11	Connection scheme of the microscope electronics	45
5.1	Characterization of the SIL	49
5.2	Synchronous scan of a gold tip	51
5.3	Photoluminescence image of a gold tip	51
5.4	Photoluminescence scan of CoMoCat at low temperatures	53
5.5	Resonance curves for different environments	56
5.6	Resonance curves with different Q factor	57
5.7	Approach curve of the tip	58
5.8	AFM point measurement at low temperatures	59
5.9	AFM scan of flat surface at low temperatures	60
5.10	AFM scan on CoMoCat at low temperatures	61
5.11	Illumination channels	64
5.12	Centering of the tip in the laser focus	65
5.13	Radially polarized laser mode	66

LIST OF FIGURES

5.14	Low temperature near field image region 3	67
5.15	Low temperature near field image region 1	68
5.16	Low temperature near field image region 2	69
A.1	System: Beam path	78
A.2	System: Optical and electrical connections	79
A.3	System: Measurement stacks	80
A.4	Software: Main Panel	83
A.5	Software: Scanner Control Panel	84
A.6	Software: Scan Data Display	85
A.7	Z Control Feedback Loop panel.	86
A.8	PLL tab.	87
A.9	Lever Excitation tab.	87
A.10	Coarse tab.	88
A.11	Scan tab.	88
A.12	Resonance tab.	89
A.13	Buttons for data storage.	89
A.14	System: AFM head plate	91
A.15	System: Tip gluing	93
A.16	System: Tip centering	94
A.17	System: Tape	95
A.18	System: Vacuum chamber and pump	96

List of Tables

5.1	Properties of the investigated solid immersion lenses.	48
5.2	Roughness parameters of the investigated solid immersion lenses.	50
A.1	Settings for the output limit of different temperatures.	82
A.2	Troubleshooting.	100

List of Publications

During the course of my PhD research, the following peer-reviewed papers have been published:

N. Mauser, N. Hartmann, M. S. Hofmann, J. Janik, A. Högele, A. Hartschuh “Antenna-Enhanced Optoelectronic Probing of Carbon Nanotubes”, *Nano Lett.* **14**, 3773 (2014).

X .Shi, N. Coca-Lopes, J. Janik, A.Hartschuh. “Advances in Tip-Enhanced Near-Field Raman Microscopy Using Nanoantennas”. *Chem. Rev*) ASAP (2017).

J. Janik, A. Hartschuh “A new low temperature near-field microscope”, to be submitted to *Rev. Sci. Instrum.*)

List of Conferences

Workshop on Nano Carbon Optics

Niederstetten (Germany), 25.09. - 28.09.2012

Oral Presentation: High-Resolution Lifetime Imaging of CdSe Nanowires

Poster: High-Resolution Lifetime Imaging of CdSe Nanowires

NIM Winter School

Kirchberg (Austria), 03.03 - 09.03.2013

Poster: A new low temperature near-field optical scanning microscope

Symposium: Nanosystems for Solar Energy Conversion

Munich (Germany), 24.07. - 26.07.2013

Poster: High-resolution optical characterization of nanomaterials

WE-Heraeus-Seminar: Light at the Nanotip

Bad Honnef (Germany), 04.08 - 08.08.2013

Poster: A new low temperature near-field optical scanning microscope

CeNS Workhop: Nanosciences: Great Adventures on Small Scales

San Servolo (Italy), 16.09. - 20.09.2013

Poster: A new low temperature near-field optical scanning microscope

DPG Frühjahrstagung 2014

Dresden (Germany), 30.03. - 04.04.2014

Oral presentation: A new low temperature near-field optical scanning microscope

Condensed Matter 2014

Paris (France), 24.08 - 29.08.2014

Oral presentation: New Directions in Tip-Enhanced Near-Field Optical Microscopy

Winterschool: Electronic Properties of Novel Materials

Kirchberg (Austria), 07.03 - 14.03.2015

Poster: New Directions in Tip-Enhanced Near-Field Optical Microscopy

LIST OF CONFERENCES

DPG Frühjahrstagung 2015

Dresden (Germany), 15.03. - 20.03.2015

Oral presentation: New Directions in Tip-Enhanced Near-Field Optical Microscopy

DPG Frühjahrstagung 2016

Dresden (Germany), 06.03. - 11.03.2016

Poster: New Directions in Tip-Enhanced Near-Field Optical Microscopy

Acknowledgments

Viele wichtige Menschen haben meinen Weg während meiner Doktorarbeit gekreuzt oder mich dabei begleitet. Alle haben auf die ein oder andere Art und Weise ihren Beitrag geleistet um diese Arbeit möglich zumachen. Bei all diesen lieben Menschen möchte ich mich hiermit bedanken.

An erster Stelle gilt mein Dank meinem Doktorvater Achim Hartschuh, für die Möglichkeit ein so spannendes Thema unter seiner Leitung zu bearbeiten. Seine wissenschaftliche Unterstützung und seine Diskussionsbereitschaft waren immer sehr hilfreich und motivierend.

Des Weiteren Danke ich Prof. Wintterlin, dass er die Aufgabe des Zweitgutachters übernommen hat.

Der Firma Attocube und den an diesem Projekt beteiligten Mitarbeitern danke ich für den Support und die Beantwortung meiner vielen Fragen.

Ich danke all meinen Kollegen und Freunden Irene, Veit, Nicolai, Xian, Kevin, Nicolas, Tobia, Harry, Richard, Alberto, Nicolai, sowie den Ehemaligen Matthias, Giovanni und Tobias für die tolle Zeit und die angenehme Arbeitsatmosphäre.

Ein herzlicher Dank geht an Nina und Miriam, für ihre Einführung in die Grundlagen der Nahfeldmikroskopie und insbesondere für ihre andauernde Freundschaft.

Ein besonderer Dank geht an die Kellercrew: Sophia, Ramona und Michi, für den Kaffee, die vielen hilfreichen Gespräche und die gelegentlichen Aufmunterungen.

Vielen Dank an die guten Seelen der Verwaltung, speziell Rita Römling und Alena Vock, für die zahlreiche Hilfe im Kampf mit der Bürokratie.

Meiner Familie bin ich über alles Dankbar für ihre andauernde Liebe und Unterstützung.

Can ich danke dir für deine Geduld und dein Verständnis und dafür, dass du mein Fels zum Anlehnen warst, wann immer ich es nötig hatte.